# *Non-linear Static and Dynamic Finite Element Analyses of Reinforced Concrete Structures*

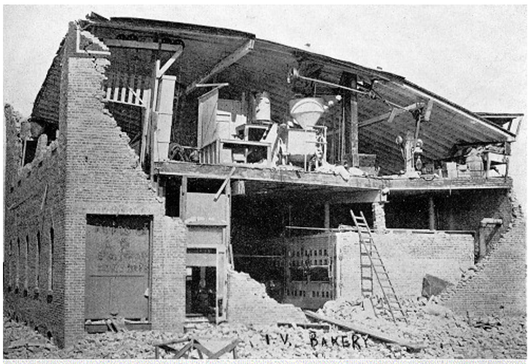


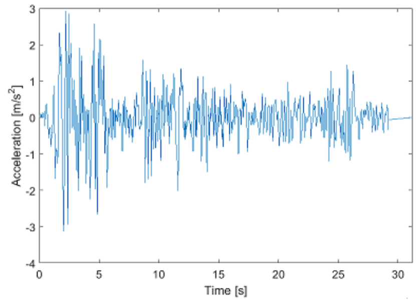


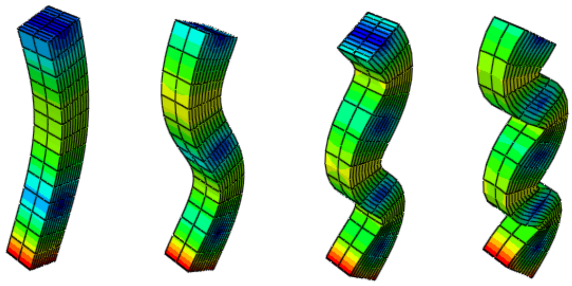

MASTER THESIS
Michele De Filippo
Aalborg University
Structural and Civil Engineering
June 8, 2016

In memory of Mimmo,
a loyal friend,
who fought with all his courage and strength
against a terrible illness,
and flew away wrongly too soon.
Its determination will always be of example for me.
I miss you everyday.

**School of Engineering and Science**
**Study Board of Civil Engineering**
Fibigerstræde 10
9220 Aalborg Ø
http://www.ses.aau.dk

**Title:** Non Linear Finite Element Analyses of Reinforced Concrete Buildings
**Theme:** Non Linear Analysis of Earthquake Induced Vibrations
**Project period:** MSc. 4th semester. Feb. 2016 - Jun. 2016

**Student:**

Michele De Filippo

**Supervisor:**
Lars Andersen

**Issues: 9**
**Pages: 84**
**Annex-CD: 1**
**Turn-in: 08-06-2016**

Synopsis:

This report documents static and dynamic analyses of reinforced concrete structures. Analytical and numerical analyses are carried out for a static case.
The beam strength and displacements is analytically evaluated in accordance to the prescriptions of the Eurocode 2.
The numerical analyses are performed by using the Finite Element Method, and creating shell and solid models through the commercial software Abaqus.
The material model used for concrete is the so called Concrete Damage-Plasticity. Steel is modeled by the commonly known elasto-plastic perfect plastic model.
Dynamic analyses are performed with reference to the El Centro earthquake. Such data are adjusted to match the structure eigenfrequency in order to provoke resonance. Simulations are then carried out leading the model to fail. The time-dependent displacement amplitudes are then reduced to investigate the plastic behavior of the model. The results are then analyzed and compared, and finally conclusions are carried out on the efficiency of the built-up models.

# Preface

This report is the representation of the project work done by on the 4th semester MSc. on Structural and Civil Engineering at Aalborg University. The project has the theme *Non linear Analysis of Earthquake Induced Vibrations* and the topic is mainly concerned on Finite Element modeling of reinforced concrete structures. This report includes a static analysis on a reinforced concrete beam, and a dynamic analysis of a reinforced concrete column. The project is done with supervision and guidance of Lars Andersen and is handed in on the June 8, 2016.

I want to express my gratitude to Lars Andersen for being a great supervisor, and for having continuously supported and motivated the work done for this Master Thesis.

## Reading guide

### Source Citation

Source references are developed by Vancouver referencing system and refer to the full source list at the back of the report with author, title, publisher and year when available. A source will be indicated by a number as follows: [Number].

### Figures, tables and formulas

Figures, tables and formulas in the report will be numbered under which chapter they belong and which number in the sequence of tables, figures and formulas they are in chapter. As an example, "Figure 5.2" can be found in Chapter 5 and be the second figure. Equations numbers appear in parentheses and shifted to the right side of the document.

### Annex

The annex is available on a CD located on the report's rear side. This CD is be referred as "Annex-CD", and contains all the calculations underlying the report's contents.

# Contents

# List of Figures

# Introduction 1

## 1.1 Reinforced Concrete

Concrete is a composite material constituted of coarse and fine aggregates bonded together with a fluid cement which hardens over time. More specifically the fluid cement consists of water and cement, and the aggregates are gravel and sand.
Fig. 1.1 gives more detailed informations on the standard quantities of the above mentioned components in the concrete composition. The ratio of water and cement is indirectly proportional to the material strength, thus by increasing the cement percentage an improvement in terms of strength can be obtained.
Concrete has a good strength in terms of compression, but its tensile strength is of about 1/10 of the compressive one. Moreover its ductility is not excellent as well.
The above mentioned weaknesses can be counteracted by the inclusion of some reinforcement having higher tensile strength and/or ductility giving then rise to Reinforced Concrete (RC).


***Figure 1.1.*** Concrete components quantities. [1]

The reinforcement is represented by steel reinforcing bars (rebars), and they are embedded in the concrete before this is poured. Fig. 1.2 gives an illustration of how reinforced concrete is usually produced.
Reinforcements are normally designed in particular regions where unacceptable cracking and/or structural failure may occur. [2]

***Figure 1.2.*** Fresh concrete being poured into a framework containing steel rebas. [3]

## 1.2 Project Outlines

The main objective of this report is the analysis of RC structures due to static and dynamic loading conditions through different methodologies.
RC theory is implemented to analytical and numerical static analyses on a sample beam, and to numerical dynamic analyses on a sample column.
The numerical analyses are carried out through the Finite Element Method (FEM).

## 1.3 Analytical and Numerical Static Analyses

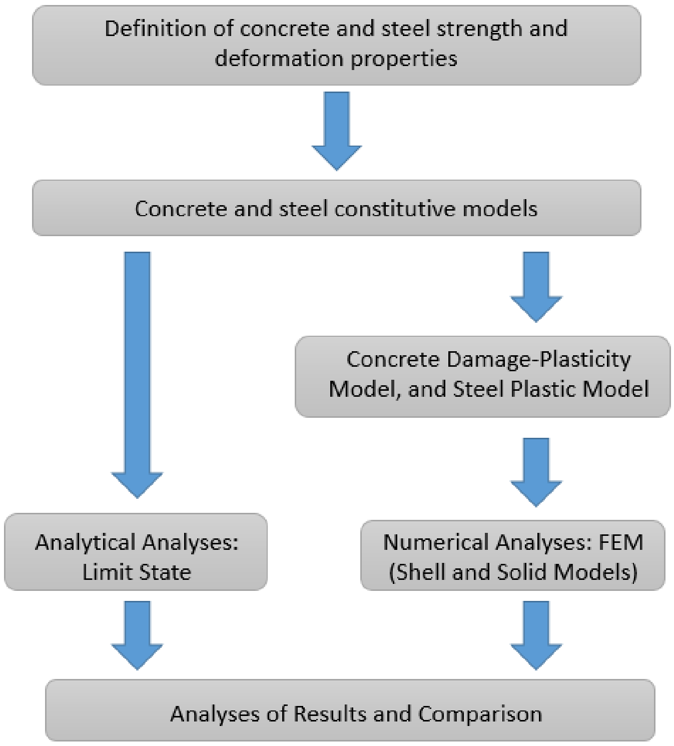


***Figure 1.3.*** General Outline of Analytical and Numerical Static Analyses.

A general step-by-step outline of this part of the report is given by Fig. 1.3. Material properties of concrete and steel are duly statistically evaluated, for different occurrence probabilities, in order to show how they affect the structural behavior of RC, and the maximum bearing load.
They are then implemented for the definition of the materials' constitutive models. Analytical static analyses are performed through limit state calculations in accordance with Eurocode 2 prescriptions. Such computation methods have been used for decades for performing structural calculations of RC buildings. Their main advantage is the calculation celerity, while their weakness is that calculations can only be performed at one cross-section per time.
The numerical analyses are carried out through the definition of a Concrete Damage-Plasticity model, and a steel plastic model then implemented into the FEM.
FE computations are, instead, slower but provide informations regarding the whole structure.
The results are then analyzed, discussed, and compared in order to evaluate the different aspects and limitations of both theories.

## 1.4 El Centro Earthquake

The earthquake data chosen to perform the simulations are derived from the El Centro earthquake of 1940 on the US west coast. Fig. 1.4 displays the geographical location of El Centro. The earthquake was the result of a rupture in the Imperial Valley, which is 8 km to the east of El Centro. It had a moment magnitude of 6.9, and was characterized as a moderate-sized destructive event. The recorded accelerations in time domain are shown in Fig. 1.5.

However the event caused significant damage since most of the buildings in that area were made up of masonry. Fig. 1.6 and 1.7 show two photos of the consequences of the earthquake. [4]

For the current analysis the application of such acceleration time series would not lead to any meaningful result to typical RC structures. Hence the data are manipulated and adjusted to make the earthquake frequency rise in order to provoke damage and a plastic response.


***Figure 1.4.*** El Centro Earthquake Location. [4]

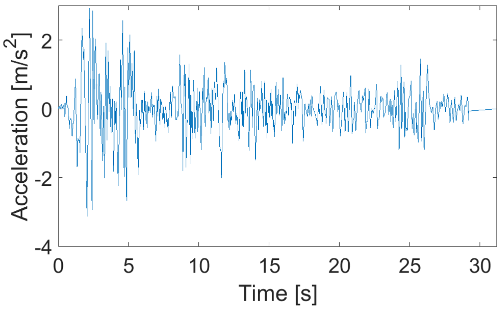


***Figure 1.5.*** El Centro Earthquake recorded accelerations in time domain.

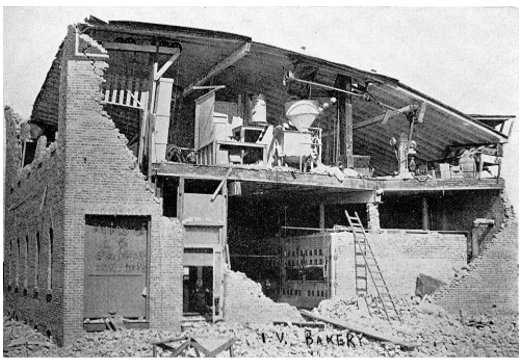

***Figure 1.6.*** El Centro Earthquake damage to a masonry construction. [4]

***Figure 1.7.*** Destroyed construction after El Centro earthquake. [4]

## 1.5 Numerical Dynamic Analyses

The second part of the project focuses on the numerical modeling of RC dynamic response. Fig. 1.8 shows the step-by-step outline for the numerical dynamic analyses.
Some of the steps previously introduced are also implemented in this analysis since the same types of concrete and steel are used to model the column as well.
By the definition of the numerical models for concrete and steel the FE models are built-up, and their eigenfrequencies are extracted through a modal analysis.
As previously mentioned the earthquake data are then adjusted in order to provoke more meaningful dynamic responses.
From the models build-ups and such data manipulation the FE analyses are carried out. Finally the obtained results are compared and analyzed.

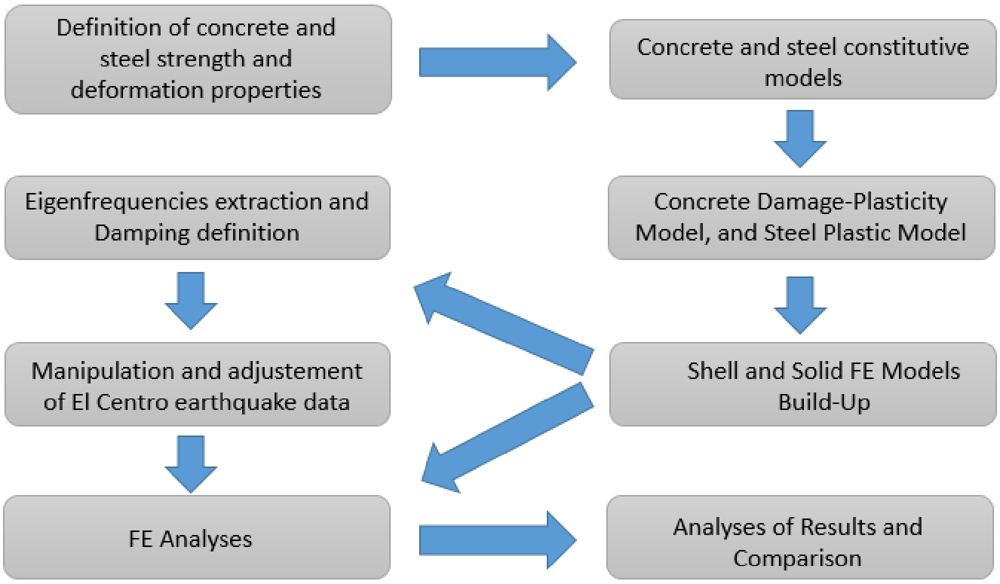


***Figure 1.8.*** General Outline of Analytical and Numerical Dynamic Analyses.

# Strength and Deformation Properties of Concrete and Steel 2

*In the present chapter a statistical approach is introduced for the evaluation of concrete compressive and steel strengths for the reinforced concrete beam. A simplified approach is instead implemented for calculating concrete tensile strength and both materials' deformation properties. Such values are required for the Limit State and Finite Element (FE) Analyses.*

Material properties are usually obtained from multiple tests performed on specimens of different sizes. The uncertainty related to the material behavior pushes companies to study statistically such properties as stochastic variables.
In the following a statical approach is implemented for evaluating concrete compressive and steel strengths.
The same procedure may be carried out also for other material properties, such as concrete tensile strength and deformation properties, but in this case a simplified approach, according to Eurocode 2, is preferred for their determination.

The types of concrete and steel for the RC design are specified in Tab. 2.1, and they are chosen in accordance to Eurocode 2 standards.

| Materials for RC Design | |
|---|---|
| Concrete | Steel |
| C20/25 | B450C |

***Table 2.1.***

## 2.1 Concrete compressive strength and steel strength

When designing any type of RC structure it is a designer's duty to specify the strength of concrete that has to be assumed for the design. Such an assumption recognizes the variability of concrete as a structural material.
The uncertainty may be higher in a non-homogeneous material, such as concrete, and lower in a more homogeneous one, like steel.
The variation of concrete compressive strength is usually assumed to follow a normal distribution. The characteristic strength is the strength below which no more than 5% of all the tested specimen from the chosen concrete mix will fall. Equally it can be expected that 95% of all the samples will have strengths in excess of the characteristic strength. The above expressed concepts are illustrated in Fig. 2.1 and 2.2. [5]

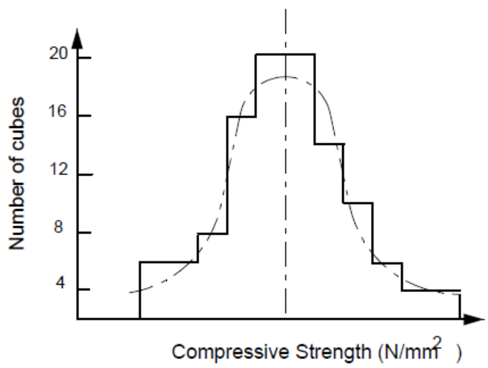


***Figure 2.1.*** Histogram of Concrete Compression Strength. [5]

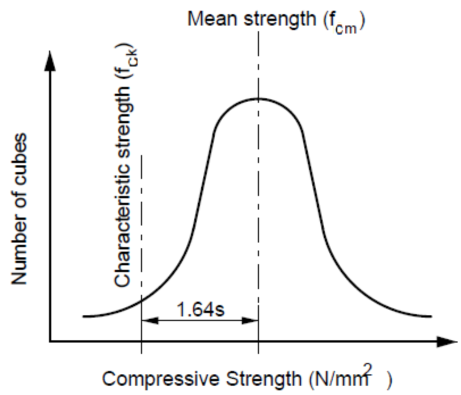


***Figure 2.2.*** Normal Distribution of Concrete Compression Strength. [5]

In Fig. 2.1 it is reported the number of specimens, cubes for example, falling into determined compressive strength intervals, and in Fig. 2.2 the histogram is approximated to a normal distribution.
The concept of characteristic strength is also displayed, and such value is usually 1.64 $\sigma$ times smaller than the mean value, where $\sigma$ is the standard deviation.
Thus :

$$f_{ck} = f_{cm} - 1.64\,\sigma \tag{2.1}$$

where

$f_{ck}$ Characteristic Compressive Strength of Concrete [MPa]
$f_{cm}$ Mean Compressive Strength of Concrete [MPa]

However the designer usually chooses a value of design strength even lower than the characteristic one in order to ensure structural safety. Such value is determined by dividing the characteristic strength by a partial safety factor $\gamma_c$, as shown in Eq.2.2.

$$f_{cd} = \alpha_i \, \frac{f_{ck}}{\gamma_c} \tag{2.2}$$

where

$f_{cd}$ Design Characteristic Compressive Strength of Concrete [MPa]
$\alpha_i$ $= 0.8 + 0.2\,\frac{f_{cm}}{88}$ [-]

The same identical approach can be applied to steel strength, with the only difference that this latter fits more likely a log-normal distribution.
The normal and log-normal distribution parameters of concrete and steel strengths are determined from their characteristic and median strengths. The statistical approach is implemented in order to define the design strength values fitting the ones given by using the partial safety factors suggested by the Eurocode 2, of 1.50 and 1.15, respectively for concrete and steel.
The concrete compressive and steel strengths are, respectively, summarized in Tab. 2.2 and 2.3. The nomenclature used for steel parameters is alike the concrete's one, where the subscript 'y' applies to steel and 'c' to concrete.

| Strength Properties Concrete C20/25 | | |
|---|---|---|
| $f_{cm}$ [MPa] | $f_{ck}$ [MPa] | $f_{cd}$ [MPa] |
| 20.0 | 28.0 | 11.5 |

***Table 2.2.***

| Strength Properties Steel B450C | | |
|---|---|---|
| $f_{ym}$ [MPa] | $f_{yk}$ [MPa] | $f_{yd}$ [MPa] |
| 479.2 | 450.0 | 391.3 |

***Table 2.3.***

The obtained results show a way lower standard deviation for steel than for concrete resulting in a more narrow probability density function (PDF). This latter statement is in accordance with what was expected since, as previously introduced, concrete production and composition lead to more uncertainties than in steel. Moreover also the design percentile is evaluated showing values of $5 \cdot 10^{-4}\%$ for concrete, and $1 \cdot 10^{-7}\%$ for steel.

## 2.2 Concrete Tensile Strength

The tensile and compressive strengths of concrete are not proportional against each other, and particularly for higher strength grades an increase in compressive strength leads only to a minor raise of the tensile strength. For this reason two different formulas, Eq. 2.3 and Eq. 2.4, are presented for calculating the median tensile strength of concrete. [6]

$$f_{ctm} = 0.3\,(f_{ck})^{\frac{2}{3}} \qquad Concrete\,Grades\ \leq\ C50/60 \tag{2.3}$$

$$f_{ctm} = 2.12\ \ln(1 + 0.1\,(f_{ck} + \Delta f) \qquad Concrete\,Grades\ \geq\ C50/60 \tag{2.4}$$

where

| | |
|---|---|
| $f_{ctm}$ | Concrete Median Tensile Strength [MPa] |
| $\Delta f$ | = 8 MPa |

In this projec, as shown in Tab. 2.2, the chosen concrete grade is C20/25, thus Eq. 2.3 is used.
An evaluation of lower and upper values of the characteristic tensile strength, $f_{ctk,min}$ and $f_{ctk,max}$, may be estimated by using Eq. 2.5 and 2.6. [6]

$$f_{ctk,min} = 0.7\,f_{ctm} \tag{2.5}$$

$$f_{ctk,max} = 1.3\,f_{ctm} \tag{2.6}$$

## 2.3 Deformation Properties

In this section the properties governing the deformation of the two materials are presented, and the implemented procedure for their evaluation is illustrated.

### 2.3.1 Concrete Deformation Properties

The modulus of Elasticity, $E$, commonly known as Young's modulus, measures, the resistance to elastic deformations. It can also be treated as a stochastic variable, as it is previously done for concrete compressive and steel strengths, but for the present analysis only the determination of a median value is performed.

For concrete two different types of Young's moduli can be defined: tangent ($E_{ci}$) and secant ($E_{c1}$). A physical representation of these two is given in the concrete non-linear constitutive model presented in Fig. 2.3.

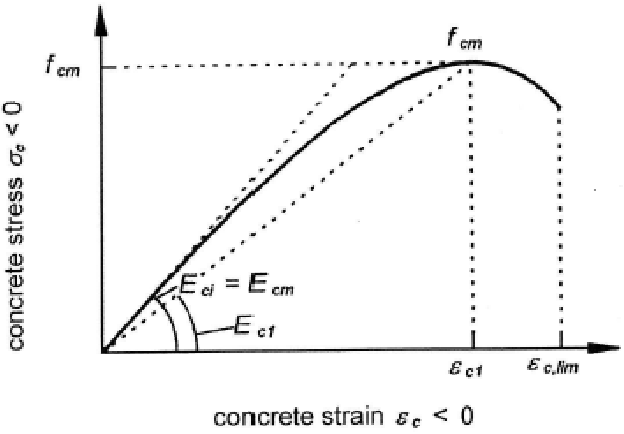


***Figure 2.3.*** Schematic representation for the compressive concrete stress-strain relation for uniaxial compression. [6]

The tangent Young's modulus, also generally called median Young's modulus ($E_{cm}$), according to Eurocode 2, can be computed from the value of concrete compressive characteristic strength as illustrated in Eq. 2.7.

$$E_{cm} = 22000 \left( \frac{f_{ck} + 8}{10} \right)^{0.3} \tag{2.7}$$

Moreover this latter is double checked from the values of deformation properties given in function of concrete grade illustrated in Fig. 2.4.
The secant Young's modulus, strain at peak value of stress ($\epsilon_{c1}$), limit strain before cracking ($\epsilon_{c,lim}$), and plasticity number $\left(k = \frac{E_{ci}}{E_{c1}}\right)$ are also evaluated according to Fig. 2.4. [6]
The ones corresponding to the chosen concrete grade are highlighted.

| Concrete grade | C12 | C16 | C20 | C25 | C30 | C35 | C40 | C45 | C50 |
|---|---|---|---|---|---|---|---|---|---|
| $E_{ci}$ [GPa] | 27.1 | 28.8 | 30.3 | 32.0 | 33.6 | 35.0 | 36.3 | 37.5 | 38.6 |
| $E_{c1}$ [GPa] | 11.1 | 12.2 | 13.3 | 14.9 | 16.5 | 18.2 | 20.0 | 21.6 | 23.2 |
| $\varepsilon_{c1}$ [‰] | -1.9 | -2.0 | -2.1 | -2.2 | -2.3 | -2.3 | -2.4 | -2.5 | -2.6 |
| $\varepsilon_{c,lim}$ [‰] | -3.5 | -3.5 | -3.5 | -3.5 | -3.5 | -3.5 | -3.5 | -3.5 | -3.4 |
| $k$ | 2.44 | 2.36 | 2.28 | 2.15 | 2.04 | 1.92 | 1.82 | 1.74 | 1.66 |

| Concrete grade | C55 | C60 | C70 | C80 | C90 | C100 | C110 | C120 | |
|---|---|---|---|---|---|---|---|---|---|
| $E_{ci}$ [GPa] | 39.7 | 40.7 | 42.6 | 44.4 | 46.0 | 47.5 | 48.9 | 50.3 | |
| $E_{c1}$ [GPa] | 24.7 | 26.2 | 28.9 | 31.4 | 33.8 | 36.0 | 39.3 | 42.7 | |
| $\varepsilon_{c1}$ [‰] | -2.6 | -2.7 | -2.7 | -2.8 | -2.9 | -3.0 | -3.0 | -3.0 | |
| $\varepsilon_{c,lim}$ [‰] | -3.4 | -3.3 | -3.2 | -3.1 | -3.0 | -3.0 | -3.0 | -3.0 | |
| $k$ | 1.61 | 1.55 | 1.47 | 1.41 | 1.36 | 1.32 | 1.24 | 1.18 | |

***Figure 2.4.*** Concrete Deformation Properties for different Concrete Grades. [6]

When a material is contracted in one direction, it then tends to expand in the other two directions perpendicular to the direction of contraction. The Poisson's ratio, $\nu$, is the negative ratio of transverse to axial strain, thus describing how much the material expands in two directions when contracting in the other one.
In the case of concrete, for a range of stresses $0.6\ f_{ck} < \sigma_c < 0.8\ f_{ck}$, the Poisson's ratio $\nu_c$ ranges between 0.14 and 0.26. Regarding the significance of $\nu_c$ for the present design, a rough estimation of $\nu_c = 0.20$ meets the required accuracy. [6]

### 2.3.2 Steel Deformation Properties

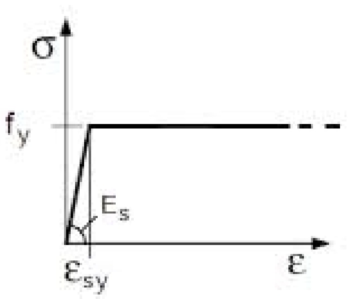


***Figure 2.5.*** Steel stress-strain relation for uni-axial compression/tension. [7]

A representation of the reinforcement steel stress-strain relation is provided in Fig. 2.5.
Given a value of yielding strain ($\epsilon_{sy}$), usually of $1.86{\cdot}10^{-3}$, the steel Young's modulus can be easily evaluated as $E_{sm} = \frac{f_{ym}}{\epsilon_{sy}}$, and it corresponds, approximately, to a value of 210000 MPa.
From Fig. 2.5 it can be noticed that no limit strain is given due to the high ductility of the material. The strain limit would be of around $1 \cdot 10^{-2}$, corresponding to a so high value that the Eurocode 2 does not specify it.
The Poisson's ratio for reinforcement steel, $\nu_s$, is estimated to be of 0.25.

# LIMIT STATE ANALYSES 3

*In the present chapter ultimate limit and serviceability state analyses are performed to determine the maximum bearing load that the beam can carry, and its vertical displacement due to such load. Different RC behavior models are implemented for both analyses.*

The Limit States of design (LSD) are conditions beyond which a structure no longer fulfills certain design criteria. The condition imposing such fulfillment is usually the degree of the load, while the criteria may refer to structural integrity, fitness for use or design requirements.
If a structure is designed according to LSD, then it is proportioned to resist all the actions that may occur during its design life with an appropriate level of reliability at each limit state.
LSD requires a structure to satisfy two principal states: Ultimate Limit State (ULS) and Serviceability Limit State (SLS).

- The ULS consists of an agreed computational condition satisfying engineering demands for strength and stability under design loads. It represents the condition at which the maximum strength of the two materials, concrete and steel, is implemented to obtain the maximum bearing load that the structure can carry.

- The SLS is a computational check proving that under the action of characteristic design loads the structural behavior complies with, and does not exceed, the SLS design criteria values. Such criteria values include stress limits, deformation limits (deflections, rotations and curvatures), flexibility (or rigidity) limits, dynamic behavior limits, cracks width control and other dispositions regarding the durability of the structure and its level of daily service and human comfort. [8]

In the following, at first, the RC behavior is introduced, then the materials' constitutive models for concrete and steel are presented. Secondly through the implementation of such material models into the RC cross-section the maximum bearing moment is evaluated in accordance to the Eurocode 2 dispositions for the ULS. The maximum bearing load is then calculated in function of the chosen static system. Finally the vertical displacement is calculated according to the Eurocode 2 dispositions for the SLS with reference to the maximum bearing load computed in the ULS.

## 3.1 Behavior of RC Beam

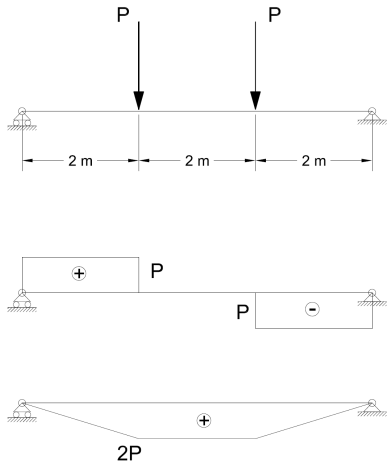


***Figure 3.1.*** Static System and force diagrams used for the analysis.

A beam is defined as an element having one dimension (length) much bigger than the other two (height and width).

Beams usually assume a bending behavior due to the loads they are designed to carry, resulting in a small curvature. For the current analysis the static system has been assumed as represented in Fig. 3.1. Hence the beam has to counteract the loading moment with an equal and opposite bending moment developed by the combined action of concrete and rebars.

The beam cross-section has then a part reacting in tension and another one in compression, respectively corresponding to positive and negative normal stresses. The neutral axis separates them, and it is defined as the axis where normal stresses are none. Its distance from the upper edge of the cross-section is named $x_n$. The compressed and tensed faces develop respectively two equal and opposite forces at a certain distance which generate the previously introduced resisting bending moment.

The beam cross-section geometrical properties are illustrated In Fig. 3.2 (a), and they are summarized in Tab. 3.1.

Moreover in Fig. 3.2 four examples of RC stress distributions are given.

The condition of linear stress distribution is represented In Fig. 3.2 (b), in which concrete does not reach its maximum strength in compression, and neither in tension.

In Fig. 3.2 (c) the condition of linear stress distribution is represented again, but in this case concrete reaches its maximum strength in compression and also in tension. As result several cracks open on the tensile face, concrete is not able to support such a high tensile stress, and the rebars thus counteract such weakness.

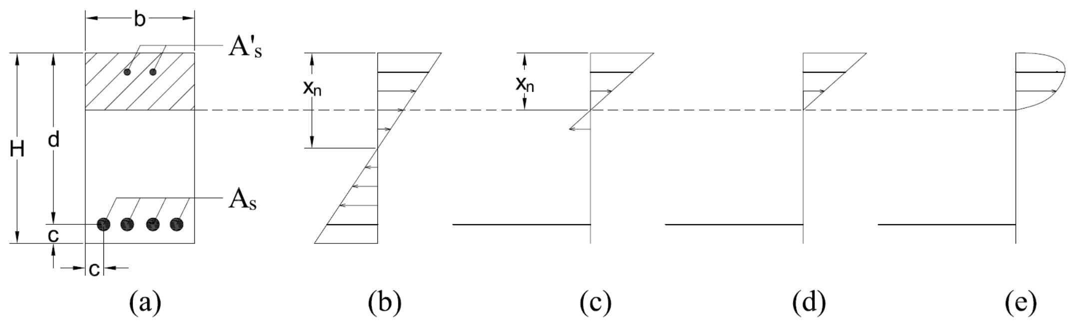


***Figure 3.2.*** (a) Beam Cross-Section (b) Linear Stress Distribution (c) Linear Stress Distribution with Tensile Failure in Concrete (d) Linear Stress Distribution with no tension in Concrete (e) Concrete experimental stress distribution on the compressed face and no tension in Concrete

| Cross-Section Properties | | | | | |
|---|---|---|---|---|---|
| $b$ [mm] | $H$ [mm] | $c$ [mm] | $d$ [mm] | $A_s$ [mm$^2$] | $A_s$ [mm$^2$] |
| 280.0 | 470.0 | 45.0 | 425.0 | $4\phi 16 = 803.8$ | $2\phi 8 = 100.5$ |

***Table 3.1.*** Beam Cross-Section Properties as indicated in Fig. 3.2

Therefore the rebar on the tensile face has the duty to provide an equal and opposite force to the one produced by the compression face. In order to do that the rebar on the tensile face yields. The rebar on the compressive face may yield too, but such condition need to be verified. The cracking of concrete on the tensile face lead to a reduction of the neutral axis depth $x_n$.
The same condition as in Fig. 3.2 (b) is represented in Fig. 3.2 (d), but the contribution of concrete in the tensile face is omitted since it only had a minor impact.
The stress distribution is finally displayed in its more realistic shape in Fig. 3.2 (e), thus in a non-linear distribution with a softening part after the peak stress. This latter corresponds to the same constitutive model as represented in Fig.2.3 rotated of 90°.

## 3.2 Concrete and Steel Constitutive Models

In this section the constitutive models used for concrete in compression and for steel in compression and tension are presented. A constitutive model for concrete in tension is not derived since concrete is assumed to not react in tension.

Ideally the concrete compressive behavior should likely match the one represented in Fig. 2.3. However an approximation of this behavior is carried out leading to a trustful and simpler solution. Such model is commonly known as Parabola - Rectangle.
The curves are represented in Fig. 3.3, and are obtained with Eq.3.1 and 3.2 by inserting into $f_c$ the values of concrete compression strength summarized in Table 2.2. [6]

$$\frac{\sigma_c}{f_c} = -\left(\frac{k\,\eta - \eta^2}{1 + (k-2)\,\eta}\right) \qquad for \;\; |\epsilon_c| < |\epsilon_{c,1}| \tag{3.1}$$

$$\frac{\sigma_c}{f_c} = 1 \qquad for \;\; |\epsilon_c| \geq |\epsilon_{c,1}| \tag{3.2}$$

where

| | |
|---|---|
| $f_c$ | Values of median, characteristic and design concrete compression strength [MPa] |
| $\eta$ | $= \frac{\epsilon_c}{\epsilon_{c1}}$ [-] |
| $\epsilon_c$ | Concrete Strain [-] |

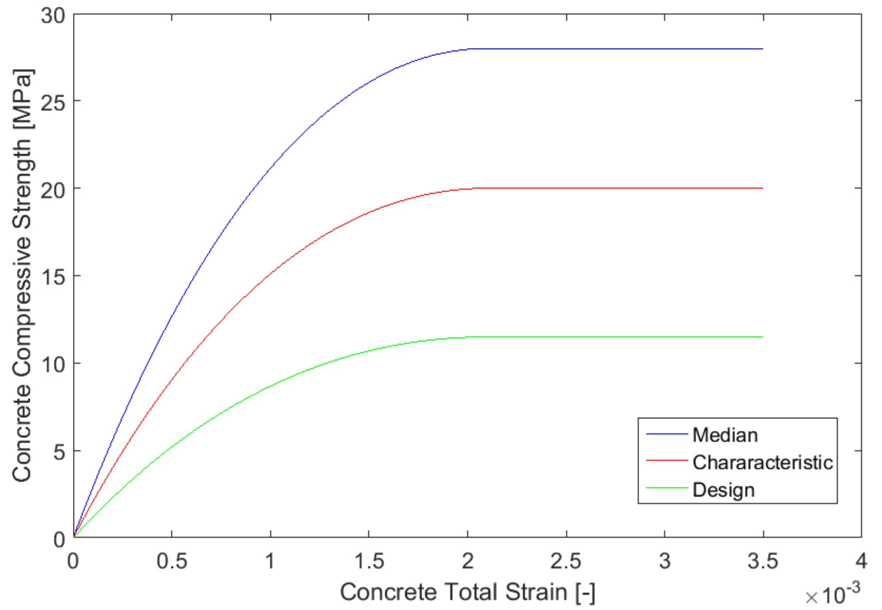


***Figure 3.3.*** Concrete Parabole-Rectangle Compression Model for Median, Characteristic and Design values of concrete compression strength.

Regarding the constitutive relationship for reinforcement steel the elastic perfect-plastic model is used with reference to steel yield strength values summarized in Table 2.3.
Fig. 3.4 represents the obtained constitutive models.

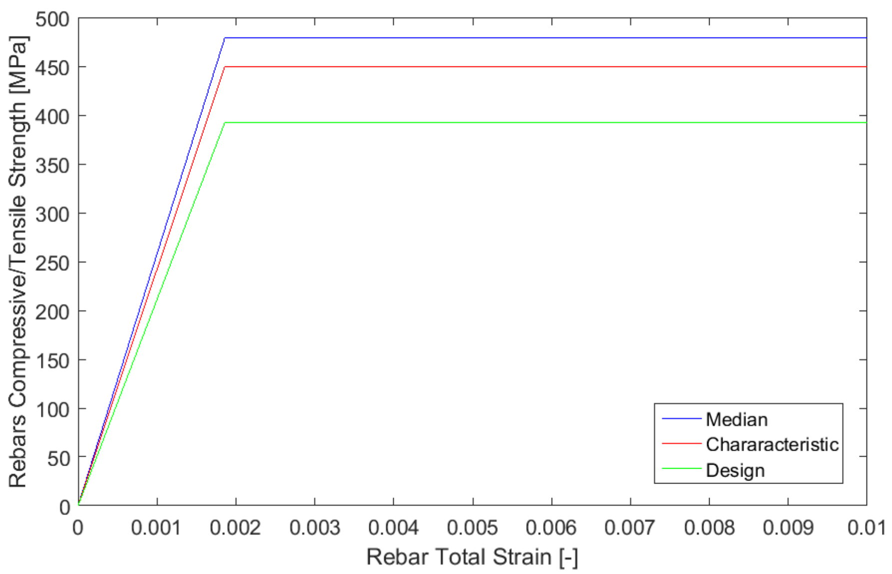


***Figure 3.4.*** Steel Elastic Perfect-Plastic Model for Median, Characteristic and Design values of steel strength.

## 3.3 Ultimate Limit State

The material models shown in the previous section are now implemented in the ULS for evaluating the maximum bearing moment that the RC cross-section can carry.
By substituting the obtained Parabola-Rectangle model into the compression face of Fig. 3.2 (d) the RC cross-section behavior turns to the one displayed in Fig. 3.5.

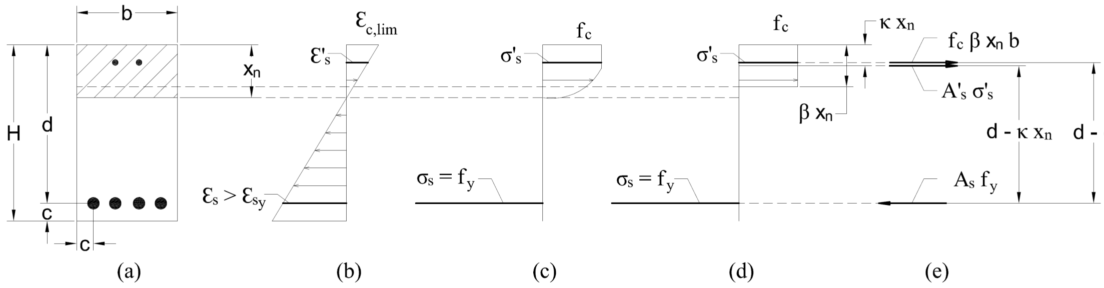


***Figure 3.5.*** (a) Beam Cross-Section (b) Linear Strain Distribution (c) Compressive parabole-rectangle stress distribution on the compressed face and no tension in Concrete (d) Compressive stress-block stress distribution on the compressed face and no tension in Concrete (e) Forces resulting in horizontal equilibrium and resisting moment

In Fig. 3.5 (b) the linear strain distribution for bending behavior of the beam is shown. It is displayed that the strain of the lower rebars ($\epsilon_s$) always exceeds the yielding strain ($\epsilon_{sy}$). As previously discussed the upper rebars strain ($\epsilon'_s$) may otherwise be smaller than the yielding one. The variable affecting the eventual yielding of the upper rebars is the distance of the neutral axis from the upper edge of the cross-section. For a fixed position of the upper rebars the minimum value of $x_n$ providing yielding in the upper rebars can be calculated from a simple linear interpolation. Such calculation leads to a minimum value of neutral axis depth of 96.1 mm.
The usage of different values of concrete strength (median, characteristic and design) implicates a change of $x_n$, thus resulting in a possible modification of the stress contribution given by the upper rebars ($\sigma'_s$) which of course affects the resisting bearing moment of the cross-section, and eventually the cracking mechanism also.
According to what is previously stated the stress in the upper rebars is evaluated as shown in Eq. 3.3 and 3.4.

$$if \qquad x_n < 96.1\, mm \qquad \sigma'_s = E_s\, \epsilon'_s \tag{3.3}$$

$$if \qquad x_n \geq 96.1\, mm \qquad \sigma'_s = f_y \tag{3.4}$$

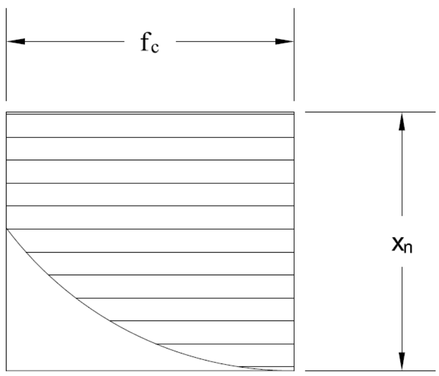


***Figure 3.6.*** Parabola-Rectangle Stress distribution over rectangle stress distribution of width equal to concrete compressive strength.

In Fig. 3.5 (c) the parabola-rectangle stress distribution is shown. Since the ratio of the parabola-rectangle area is approximately the 80 % of the rectangle of width $f_c$ area, represented in Fig. 3.6, a simplified stress model can be introduced.
Fig. 3.5 (d) represents this latter, commonly known as stress-block distribution. The principle on its basis is to approximate the non-linear parabola-rectangle shape to a simply rectangular one with the same area. In order to obtain such result the stress-block height is decreased by the factor $\beta = 0.8$.
Finally in Fig. 3.5 (e) the produced normal forces are displayed in their application points.
The compressive force developed by the concrete compression face is logically placed in the middle of the stress-block, thus at a distance from the upper edge of $\kappa\, x_n$, with $\kappa = \beta/2 = 0.4$.

The neutral axis depth, $x_n$, is calculated by satisfying the condition of horizontal equilibrium, while the maximum bearing moment can be computed through the moment equilibrium as shown in Eq. 3.5.

$$M_r = f_c\, \beta\, x_n\, b\, (d - \kappa\, x_n) + A's\, \sigma'_s\, (d - c) \tag{3.5}$$

The same approach can be implemented into another ULS model.
This latter is alike the one introduced above besides an hypothesis of linear compressive stress distribution in concrete. Such statement approximates the concrete compressive constitutive model shown in Fig. 2.3 to a linear one with Young's modulus equal to $E_{c1}$. A representation of the simplified linear model is given in Fig. 3.7.

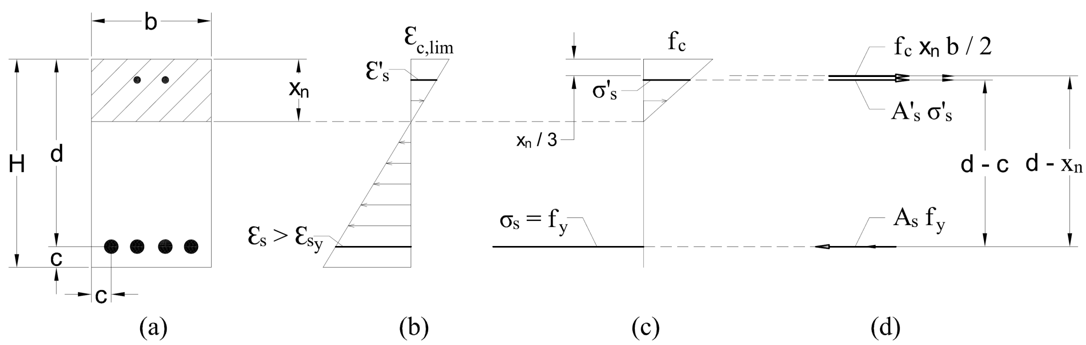


***Figure 3.7.*** (a) Beam Cross-Section (b) Linear Strain Distribution (c) Linear stress distribution on the compressed face and no tension in Concrete (d) Forces resulting in horizontal equilibrium and resisting moment

As shown in Fig. 3.7 (b) the strain distribution is still linear, thus the relations derived for determining if the upper rebars yield or not, displayed in Eq. 3.3 and 3.4, are still valid.
Fig. 3.7 (c) illustrates the above mentioned linear stress distribution on the compressive face. In this case the same approach previously introduced can be used again as well for calculating the compressive force provided by the concrete compressive face. In Fig. 3.8 the linear stress distribution is shown over the rectangle on of width equal to $f_c$. In such case it is clear that the area occupied by the linear stress distribution is 50% of the rectangle's one.
Moreover by knowing that the center of gravity of a triangle rectangle is at 1/3 of its height, and by imposing the moment equilibrium of the forces displayed in Fig. 3.7 (e) the derivation of the maximum bearing moment, shown in Eq. 3.6, can be easily carried out.

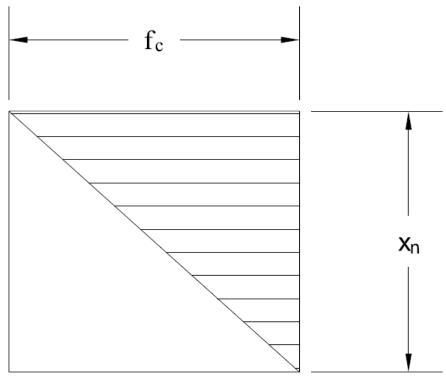


***Figure 3.8.*** Linear Stress distribution over rectangle stress distribution of width equal to concrete compressive strenght.

$$M_r = \frac{f_c \ x_n \ b}{2} \left(d - \frac{x_n}{3}\right) + A's \ \sigma'_s \ (d - c) \tag{3.6}$$

From the static system introduced in Fig. 3.1, and by assuming that the analyzed cross-section is at the beam mid-length the maximum bearing load can be calculated as illustrated in Eq. 3.7.

$$M_{max} = 2 \ P \qquad \leftrightarrow \qquad P_{max} = \frac{M_r}{2} \tag{3.7}$$

The results obtained from the median, characteristic and design strength values shown in Tables 2.2 and 2.3 using Eq. 3.5, 3.6 and 3.7 are shown in Fig. 3.9 and 3.10.

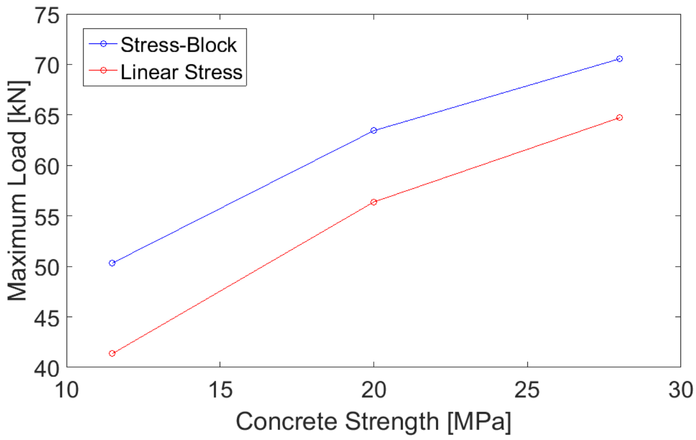


***Figure 3.9.*** Maximum Bearing Load against Concrete Compressive Strength

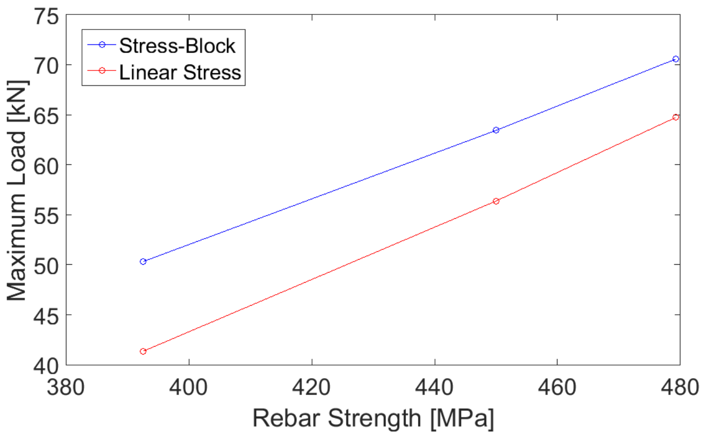


***Figure 3.10.*** Maximum Bearing Load against Rebars Strength

From the above figures a mean difference of roughly about 7.28 kN can be appreciated, corresponding to a percentage of mean difference between the two methods results of about 12.40%.
Moreover the load partial safety factor can also be evaluated from the ratio of the design load over the characteristic one, providing as results 1.26 and 1.36, respectively for the stress-block and linear stress distributions.
Surely the stress-block distribution gives a more reliable result since it is closer to the real behavior of concrete. The linear stress distribution is thought as a fair approximation of the above mentioned distribution and that is correct, but it is not simplifying the maximum bearing moment calculation that much. As result the stress-block distribution is preferred, and only this latter's results are taken into account in the following.

## 3.4 Serviceability Limit State

The SLS is used in this project in order to evaluate the magnitude of the vertical displacements due to the loads shown in Fig. 3.9 and 3.10. Such displacements are tracked at the mid-length of the beam, thus in the point circled in red in Fig. 3.11.

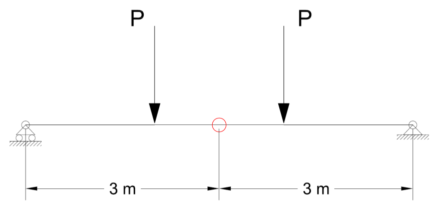


***Figure 3.11.*** Point in which the vertical displacement in tracked.

The vertical displacement is mainly function of the beam flexural rigidity. This latter is defined as the force couple required to bend the structure of one unit of curvature, or more simply as the resistance provided by a structure while undergoing bending.
The flexural rigidity is mathematically represented by the product of the Young's modulus and moment of inertia ($E\,I$). [9]
In the case of a RC beam the Young's modulus is not uniquely defined since the cross-section is composed by concrete and steel having different values of Young's moduli. Moreover the moment of inertia is not clearly well defined due to concrete's cracking when bending at ULS.
To overcome the firstly mentioned problem the homogenization factor, $n$, is introduced. Its purpose it to 'homogenize' the RC cross-section to a homogeneous one constituted only by concrete for instance. In order to do that the homogenization factor needs to be multiplied to the steel contribution therms when calculating the moment of inertia, and it is defined as $n = \frac{E_s}{E_c}$. Such operation allows to count the rebars' areas to be $n$ times the actual ones due to the difference in terms of Young's modulus between steel and concrete.
The second difficulty is vanquished by considering different behaviors of the RC cross-section as illustrated in Fig. 3.12 .

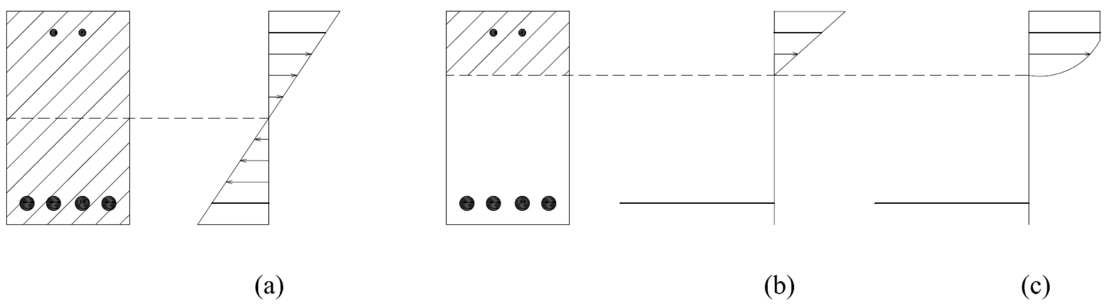


***Figure 3.12.*** Different Beam Behaviors used in SLS: (a) Linear Stress Sistribution (b) Linear Stress distribution with Tensile Failure in Concrete (c) Parabole-Rectangle Stress Distribution on the compressed face and Failure on the Tensile one

The dashed areas in the above figure represent the part of the concrete beam giving contribution to resist the bending load.
In Fig. 3.12 (a) the case in which no cracks occur in the cross-section is represented. This latter is analysed in order to evaluate how much more contribution would no cracks give to

reduce the vertical displacement. However such case is considered to be the less realistic since the ULS load is applied, thus cracks on concrete's tensile face are expected to occur. In Fig. 3.12 (b) the linear stress distribution case, previously introduced in the ULS and illustrated in Fig. 3.7, is illustrated. This latter's results in terms of maximum bearing load were shown to diverge from the most realistic one, however its results in terms of displacement are also analyzed.
In Fig. 3.12 (c) the most realistic stress relationship is shown, with a parabola-rectangle distribution on the compressed face and the concrete tensed faced cracked.
The obtained results are summarized in Fig. 3.13 where behaviors A, B and C respectively correspond to the ones in Fig. 3.12 (a), (b) and (c).

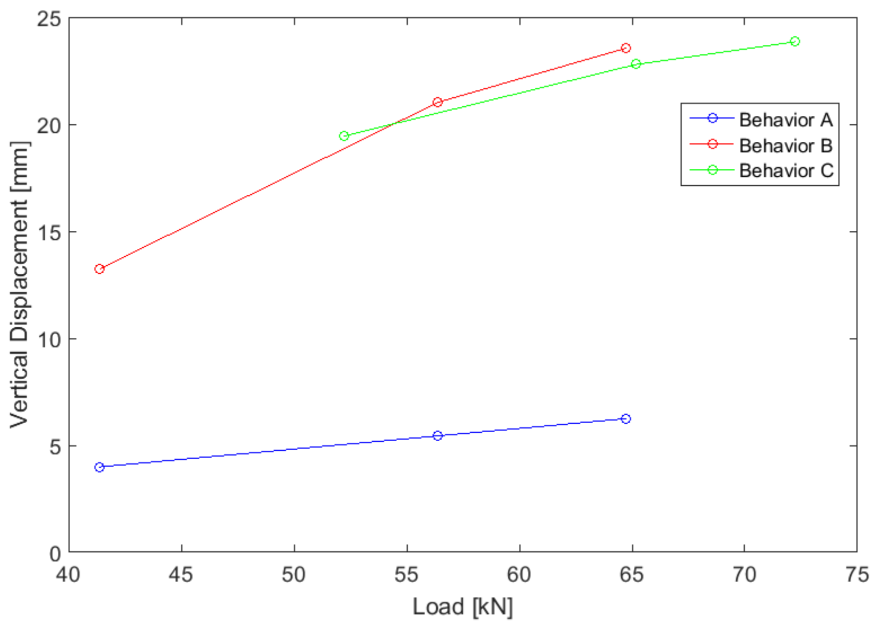


***Figure 3.13.*** Vertical Displacement against Load Magnitude.

In the above illustrated results the huge difference in terms of displacement between non-cracked (Behavior A) and cracked (Behaviors B and C) configuration can be appreciated. Such result was expected since the non-cracked cross-section has a higher moment of inertia and thus a higher flexural rigidity.
Behaviors B and C give almost the same result for similar values of load. Such statement makes sense since, with the vertical displacement calculation, the only difference between them would then be the distance of the neutral axis from the upper edge, which in the ULS calculations was almost alike. However the usage of median, characteristic and design values of concrete and steel strength gave different values of maximum bearing load, which affect also the vertical displacement magnitude.

# Material Models for FE Analyses 4

*In this chapter the concrete and steel material models used in the non-linear FE analyses are presented.*

For many years, researchers have been working toward the successful application of FE analyses to the design of RC structures. The aim was to provide a more accurate method than the simplified and approximate done shown in the previous chapter. Despite promising research in this area, only a few practical FE based design tools have been implemented in standard structural engineering technology. The goal of this study is to develop and validate such a tool regarding one particular concrete model: The Concrete Damage-Plasticity Model. [10]
Moreover RC is constituted also of rebars, thus also a plasticity model for steel needs to be introduced.
In the next chapter is then shown how to implement both together into a FE model to well represent the RC behavior.

## 4.1 Concrete Damage-Plasticity Model

The Concrete Damage-Plasticity (CDP) Model is based on the combination of damage mechanics and plasticity. Its goal is to be able to describe the important characteristics of the failure process of concrete when subjected to multi-axial loading. [11]
The model assumes the two main failure mechanisms of tensile cracking and compressive crushing. It consists of an isotropic hardening plastic model. The evolution of the yield surface is managed by the plastic strains, $\tilde{\epsilon}_t^{pl}$ and $\tilde{\epsilon}_c^{pl}$, respectively tensile and compressive.

### 4.1.1 Strength Hypothesis and CDP Parameters

Very often it is assumed the hypothesis that concrete behavior resembles the one described by the Drucker-Prager criterion. The shape of this latter is conic (as illutrated in Fig. 4.1), which implicates no complications in numerical application due to its smoothness. However the drawback is in the non-fully consistence with concrete behavior. [14]

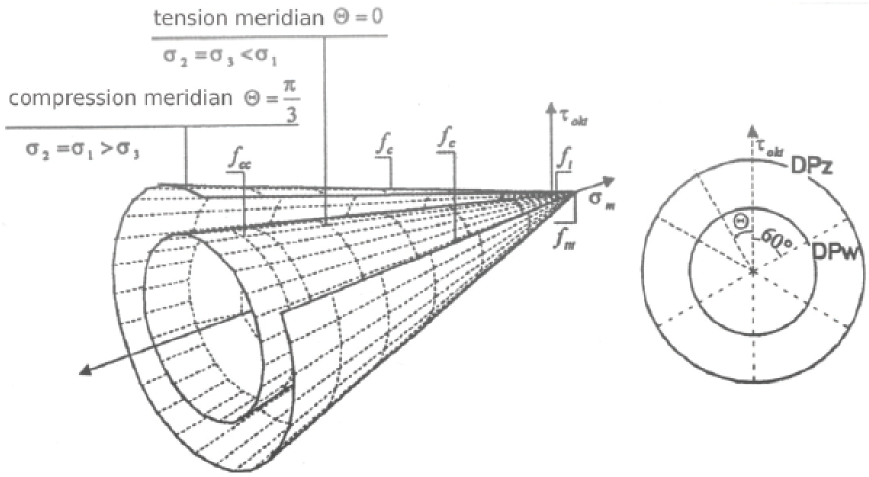


***Figure 4.1.*** Drucker-Prager Yield Surface in a 3D view and in the deviatioric plane. [14]

The CDP model is a modification of the above mentioned Drucker-Prager strength hypothesis. Such modification edits the shape of the yield surface in the deviatoric plane. The yield surface has not to be a circle since concrete strengths in compression and tension are not equal, thus the surface extension on the compressive and tensile meridian cannot be the same as it is in the case of a circle. The parameter $K_c$ governs this shape.

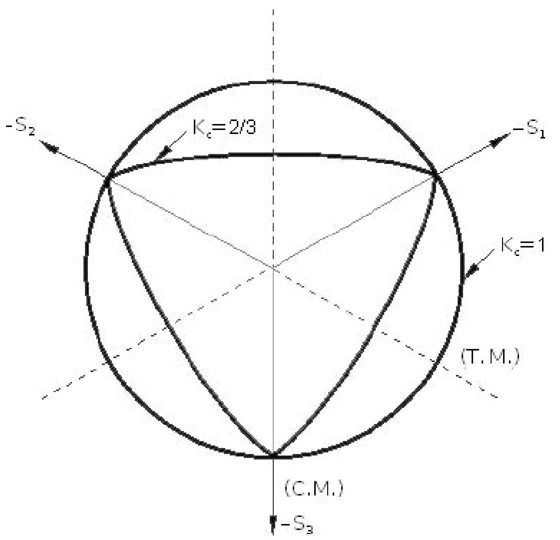


***Figure 4.2.*** CDP yield surface representation in the deviatoric plane

The physical meaning of the parameter $K_c$ is the ratio of the distances between the hydrostatic axis and respectively compression and tension meridian in the deviatoric plane. [14]. For a value of 1 the CDP yield turns to the Drucker-Prager circular shape. According to experimental results conducted on concrete samples such value can be assumed to be of 2/3, leading to a yield surface shape as given in Fig. 4.2.
The shape of the CDP yield surface in the meridional plane assumes the form of a hyperbola.
An illustration of this latter is given in Fig. 4.3. Its shape is adjusted through the plastic potential eccentricity, more commonly known as eccentricity.

It represents the distance between the vertex of the hyperbola and the intersection of the hyperbola asymptote with the hydrostatic axis.

It is usually a small number expressing the approximation of the hyperbola to its asymptote. In the case in which the eccentricity, $\epsilon$ coincides with 0 the yield surface in the meridional plane becomes a straight line as in the Drucker-Prager criterion. Usually it is recommended to assume a value of $\epsilon = 0.1$. [14]
The state of the material is described also by the ratio of the strength in biaxial state to the one in uniaxial state $\left(\frac{f_{b0}}{f_{c0}}\right)$. A physical interpretation of the meaning of such parameter is given by Fig. 4.4. Experimental results lead to a value of such parameter of approximately 1.16.

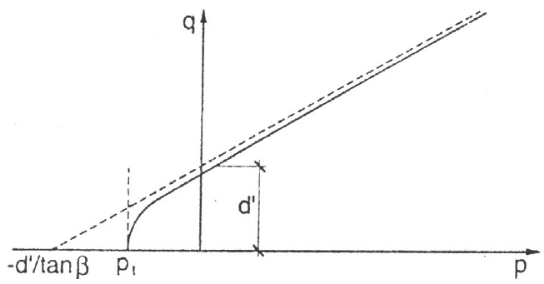


***Figure 4.3.*** CDP yield surface in the meridional plane. [14]

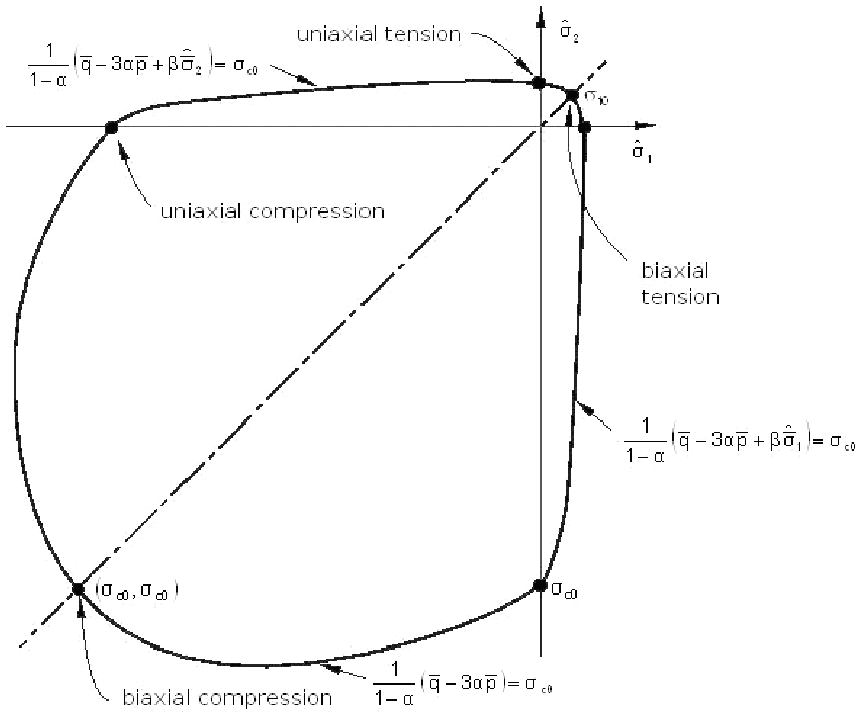


***Figure 4.4.*** Strength of concrete under biaxial stresses. [14]

Another parameter needed for defining concrete behavior is the dilation angle ($\psi$). This latter represents the inclination of the yield surface to the hydrostatic axis in the meridional plane. [14] Physically such parameter is interpreted as the concrete friction angle, and for the chosen class of concrete a value of 22° can be assumed.

Finally viscous effects can also be taken into account through the viscosity parameter. In the current analysis viscosity is ignored, thus a value of the viscosity parameter of 0 is assumed.
In Table 4.1 the above mentioned values of CDP parameters are summarized.

| CDP Parameters | | | | |
|---|---|---|---|---|
| $\psi$ [°] | $\epsilon$ [-] | $\frac{f_{b0}}{f_{c0}}$ [-] | $K_c$ [-] | Viscosity Parameter [-] |
| 22 | 0.1 | 1.16 | 0.667 | 0 |

***Table 4.1.***

### 4.1.2 General Framework

The damage-plasticity constitutive model is based on a damage, and a plasticity part. In this subsection these two aspects of the model are introduced in the mentioned order. Damage is implemented in the model in the only case in which cyclic loads are applied to the structure. The damage-plasticity model reduces to an isotropic hardening plasticity model in static conditions.

Damage is introduced into the model through the so called tensile and compressive damage variables, $d_t$ and $d_c$. They evolve within increases in plastic tensile and compressive strains ($\tilde{\epsilon}_t^{pl}$ and $\tilde{\epsilon}_c^{pl}$). Damage leads to a degradation of the 'elastic' Young's modulus, which is controlled by $d_t$ and $d_c$. Such variables are assumed to be in function of plastic strains, temperature and other field variables. In the case of analysis the influence of temperature and field variables is not taken into account, thus the damage variables are derived only in function of plastic strains as indicated in Eq. 4.1 and 4.2.

$$d_t = d_t(\tilde{\epsilon}_t^{pl}); \qquad 0 \leq d_t \leq 1 \tag{4.1}$$

$$d_c = d_c(\tilde{\epsilon}_c^{pl}); \qquad 0 \leq d_c \leq 1 \tag{4.2}$$

The damage variables can have values from 0, representing undamaged material, to 1, which represent a full loss of stiffness. [12] The constitutive model results to be degraded by the effect of damage, which lowers the Young's modulus, thus the values of the stresses are necessarily lowered. The relationships given in Eq. 4.3 and 4.4 describe the value of such stress in function of the plastic strains and damage variables.

$$\sigma_t = (1 - d_t)\, E_0\, (\epsilon_t - \tilde{\epsilon}_t^{pl}) \tag{4.3}$$

$$\sigma_c = (1 - d_c)\, E_0\, (\epsilon_t - \tilde{\epsilon}_c^{pl}) \tag{4.4}$$

Or in vectorial form as in Eq. 4.5

$$\sigma = (1 - d_t)\, \sigma_t + (1 - d_c)\, \sigma_c \tag{4.5}$$

The plasticity model is based on the effective values of stresses, which are independent of damage. The model is described by the yield function, flow rule and loading-unloading conditions. The evolution of the yield function is governed by the hardening variables, which will now be introduced. [11]

The plasticity part of the model is presented in the following. The yield function is as given in Eq. 4.6

$$f_p(\sigma, \kappa_p) = F(\sigma, q_{h1}, q_{h2}) \tag{4.6}$$

where $q_{h1}(\kappa_p)$ and $q_{h2}(\kappa_p)$ are dimensionless functions managing the size and shape of the yield function as shown in Fig. 4.5 and 4.6. The rate of hardening variable, $\kappa_p$, is connected to the rate of plastic strain by an evolution law. [11]
The flow rule is given in Eq. 4.7

$$\dot{\epsilon}_p = \dot{\lambda}\, \frac{\partial g_p}{\partial \sigma}\, (\sigma, \kappa_p) \tag{4.7}$$

where

| | |
|---|---|
| $\dot{\epsilon}_p$ | Rate of plastic strain |
| $\dot{\lambda}$ | Rate of plastic multiplier |
| $g_p$ | Plastic Potential |

The loading-unloading conditions are illustrated in Eq. 4.8.

$$f_p \leq 0, \qquad \dot{\lambda} \geq 0, \qquad \dot{\lambda} f_p = 0 \tag{4.8}$$

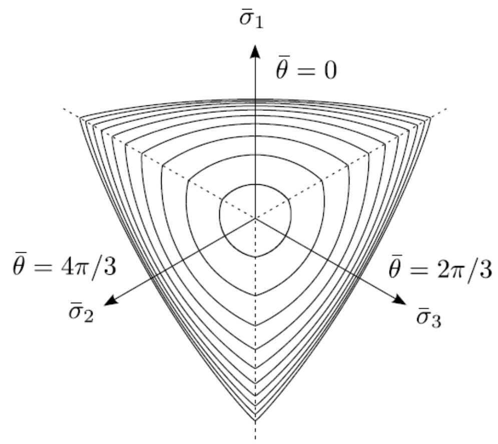


*Figure 4.5.* Evolution of yield surface in the deviatoric plane during hardening for a constant volumetric stress. [11]

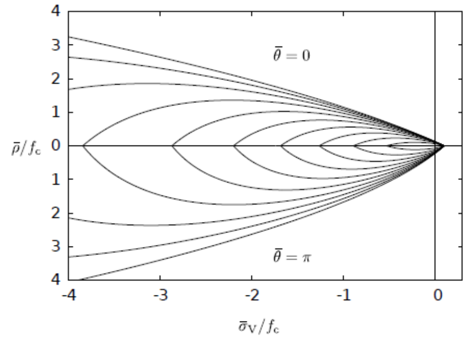


*Figure 4.6.* Evolution of yield surface in the meridional plane during hardening for a constant volumetric stress. [11]

### 4.1.3 Tensile and Compressive Stress-Strain Relationships

Concrete exhibits a complex non-linear behavior. Failure in tension is characterized by softening, which means decreasing stresses with increasing strains. This latter is also accompanied by irreversible (plastic) deformations. [11]
Under uniaxial tensile loading the stress-strain response is linear elastic until the failure tensile stress, $\sigma_{t0}$, is reached. Beyond such value some micro-cracks occur. This phenomenon is represented with a softening stress-strain response. [12]
This latter statement makes physical sense since as concrete starts cracking its capacity becomes lower and lower. The post-failure tensile relationship also defines the interaction with concrete since as the stress carried in tension by concrete decreases, the one carried by rebars should increase in order to satisfy the overall equilibrium. Such behavior is usually referred in literature as 'tension stiffening'.
Fig. 4.7 provides an illustration of the above mentioned concrete tensile stress-strain relationship.

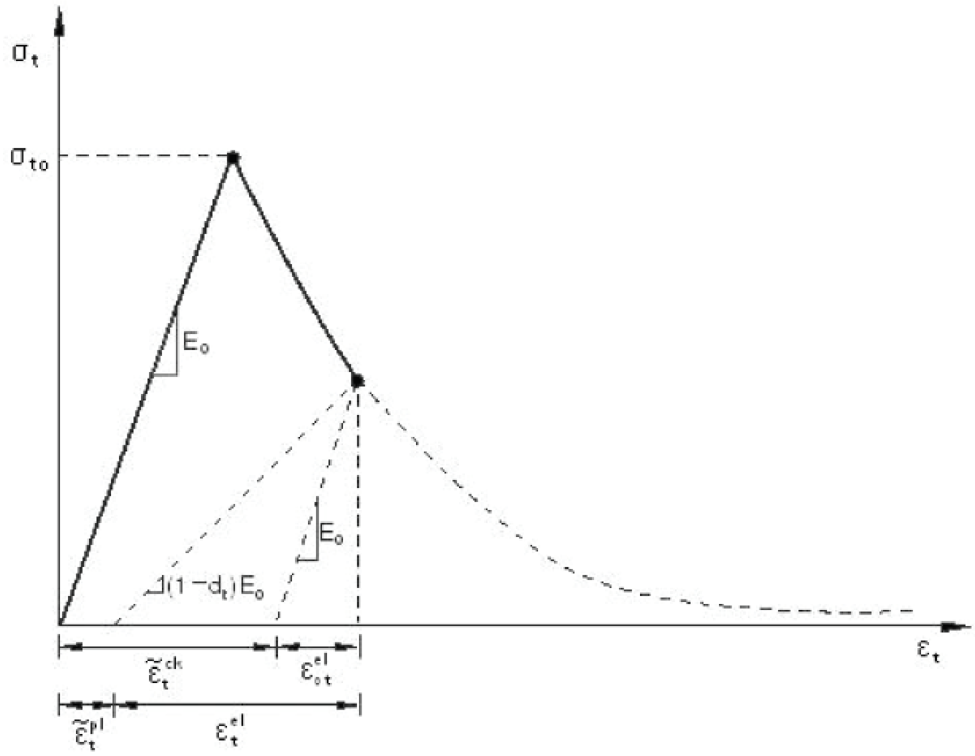


***Figure 4.7.*** Response of Concrete in Uniaxial Tensile Loading. [12]

For the tensile behavior the relation proposed by Wang and Hsu [14] is implemented. This latter is resumed in Eq. 4.9 and 4.10.

$$\sigma_t = E_c \, \epsilon_t \qquad for \qquad |\epsilon_t| \leq |\epsilon_{cr}| \tag{4.9}$$

$$\sigma_t = f_{cm} \left( \frac{\epsilon_{cr}}{\epsilon_t} \right)^n \qquad for \qquad |\epsilon_t| > |\epsilon_{cr}| \tag{4.10}$$

where

| | |
|---|---|
| $\epsilon_t$ | Tensile total strains [-] |
| $\epsilon_{cr}$ | Tensile strain at concrete cracking [-] |
| $n$ | Rate of weakening [-] |

Concrete weakening is simulated through the above mentioned rate of weakening $n$. Its value varies from 1.5, for a very weak tensile response leading to a tensile stress almost none, to 0.4, for a less weak response. The case of $n = 1.5$ provides a simulation closer to the ULS assumptions since concrete is almost non responding in tension once $\epsilon_{cr}$ is superseded. Also some intermediate values of $n$ are taken into account in order to illustrate how such factor affects the tensile response of concrete. Fig. 4.8 shows concrete tensile stress-strain relationships according to 4.9 and 4.10.

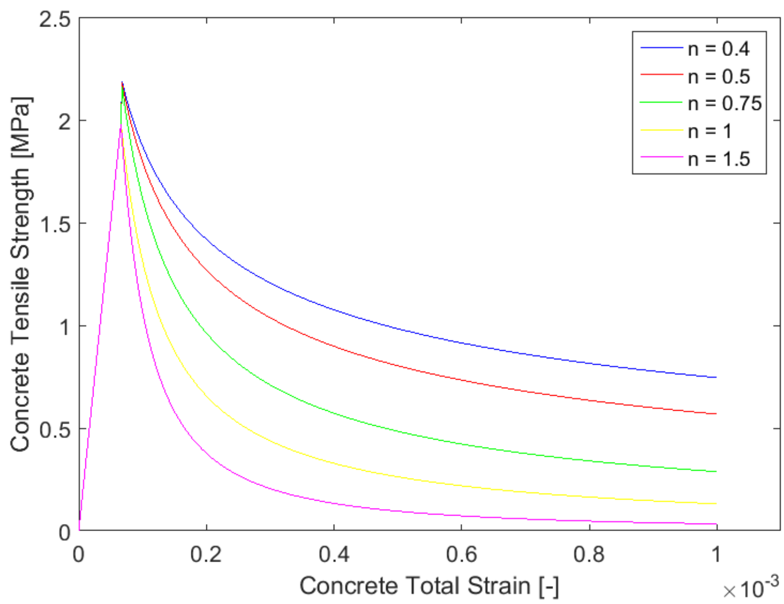


***Figure 4.8.*** Concrete Tensile Stress-Strain Relationships in function of the total strains.

The numerical analyses are carried out in function of the so called cracking strains $\tilde{\epsilon}_t^{ck}$. The cracking strains physically represent the strains after cracking, defined as the difference between the total strain ($\epsilon_t$) and the elastic strain for the undamaged material ($\epsilon_{0t}^{el}$), as shown in Eq. 4.11. [14] The elastic strain definition is also given in Eq. 4.12.

$$\tilde{\epsilon}_t^{ck} = \epsilon_t - \epsilon_{0t}^{el} \tag{4.11}$$

$$\epsilon_{0t}^{el} = \frac{\sigma_t}{E_c} \tag{4.12}$$

An illustration of the above mentioned concepts is given in Fig. 4.7, and Fig. 4.9 illustrates the stress-strain relationship in function of cracking strains.

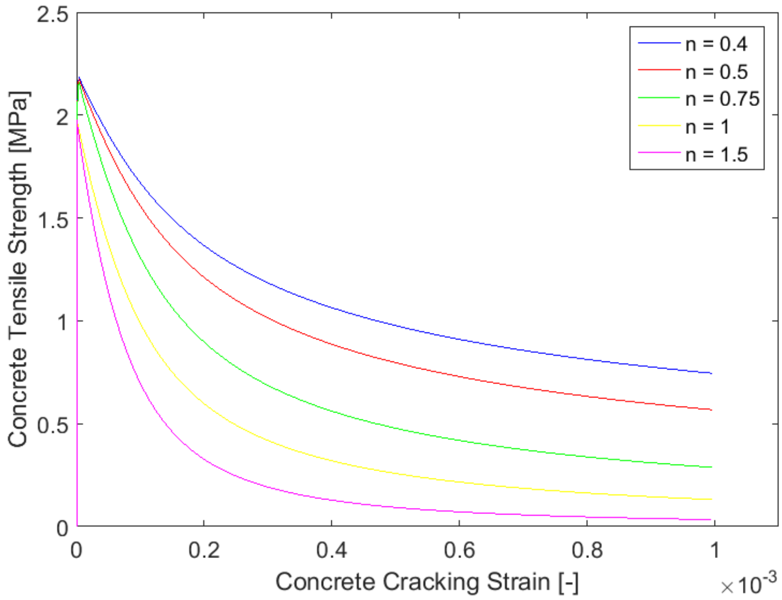


***Figure 4.9.*** Concrete Tensile Stress-Strain Relationships in function of the total strains.

Another manner of representing the 'tension stiffening' is by means of the concrete fracture energy ($G_f$). It represents the most useful parameter in the analysis of cracked concrete structures. A representation of this latter is given in Fig. 4.10.

The fracture energy is defined as the area under the tensile stress - displacement evidenced in gray. The definition of such parameter is carried out in function of the maximum tensile stress and the maximum displacement that concrete can allow.
For the case of analysis a fracture energy of 0.25 N/mm is chosen, thus providing a maximum tensile displacement of 0.25 mm, which gives good physical sense.

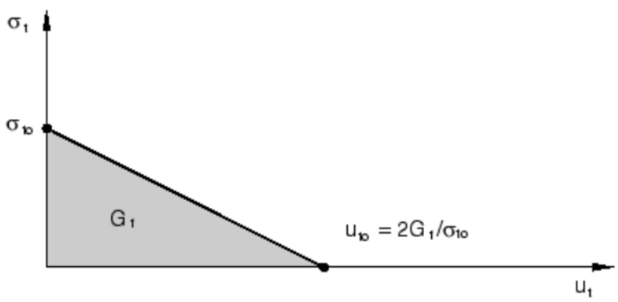


***Figure 4.10.*** Post-failure stress-fracture energy curve. [12]

On the other hand, in compression the response is linear until the initial yield stress $\sigma_{c0}$. In the plastic range between $\sigma_{c0}$ and the ultimate stress, $\sigma_{cu}$, the response is characterized by stress hardening. Beyond $\sigma_{cu}$ a softening regime takes place. [12]
The compressive stress-strain response is given in Fig. 4.11.

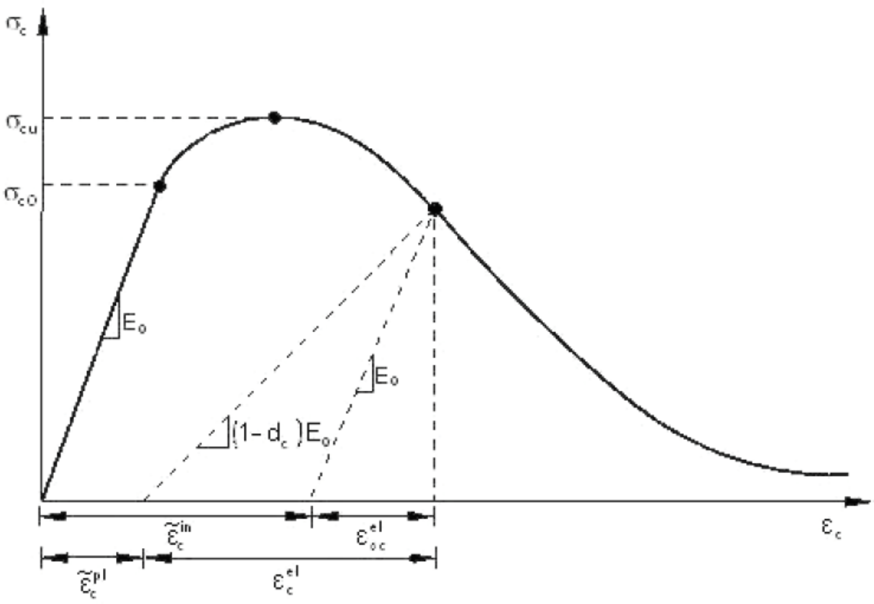


***Figure 4.11.*** Response of Concrete in Uniaxial Compressive Loading. [12]

Such response may easily be obtained by extensively applying Eq. 3.1 also for values of $|\epsilon_c| \geq |\epsilon_{c,1}|$. The obtained stress-strain relationships are illustrated in Fig. 4.12.

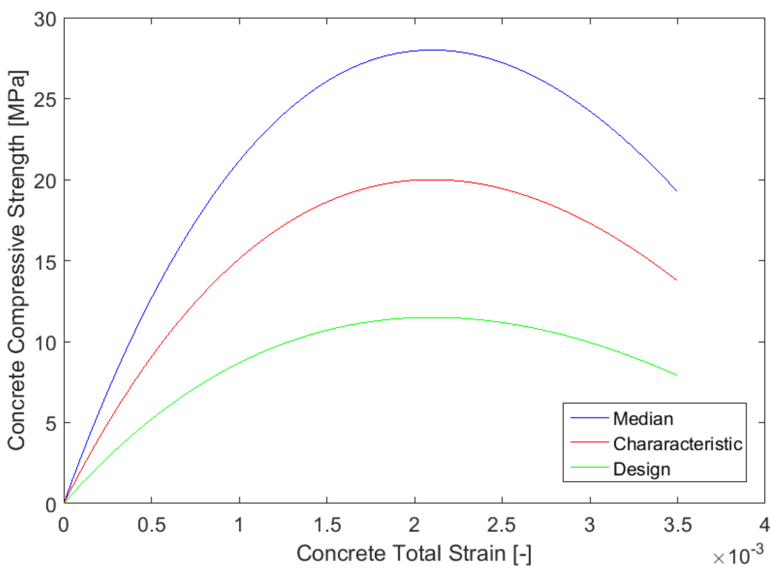


***Figure 4.12.*** Compressive Stress-Strain Relationships for softening response in function of total strains.

However the numerical analyses are, for the compressive part, carried out with reference to plastic strains. Inelastic strains, $\tilde{\epsilon}_c^{in}$, are defined by subtracting the elastic part, corresponding to the undamaged material ($\epsilon_{0c}^{el}$), to the total strains ($\epsilon_c$). The above mentioned concept is similar to the one of cracking strain, and is summarized in Eq. 4.13 and 4.14.

$$\tilde{\epsilon}_c^{in} = \epsilon_c - \epsilon_{0c}^{el} \tag{4.13}$$

$$\epsilon_{0c}^{el} = \frac{\sigma_c}{E_c} \tag{4.14}$$

When converting then inelastic strains to plastic strains it is needed to assume a stress threshold from which the response is assumed to be non-linearly elastic. Experimental tests show evidence of almost lack of linearity in the concrete compressive behavior, but in most numerical analyses the initial elastic non-linearity can be neglected. The threshold is assumed thus at a stress value of 0.4 $fc$. Such statement well fits the compressive stress-strain relationship provided in Eq. 3.1.
Fig. 4.7 and 4.11 also show the unloading behavior within the plastic regime. As previously introduced, after plastic deformations occur the initial Young's modulus, $E_0$, results to be damaged, and thus decreased. The unloading response appears to be weakened. The plastic strains can then be computed, in the compressive and tensile case, respectively as in Eq. 4.15 and 4.16.

$$\tilde{\epsilon}_c^{pl} = \epsilon_c - \frac{d_c}{(1-d_c)}\frac{\sigma_c}{E_0} \tag{4.15}$$

$$\tilde{\epsilon}_t^{pl} = \epsilon_t - \frac{d_t}{(1-d_c)}\frac{\sigma_t}{E_0} \tag{4.16}$$

In case of undamaged material ($d_c = 0$, $d_t = 0$) the plastic strains reduce to the inelastic ones, defined for the compressive case in Eq. 4.13. The compressive stress-strain relationship in function of plastic strains is given in Fig. 4.13

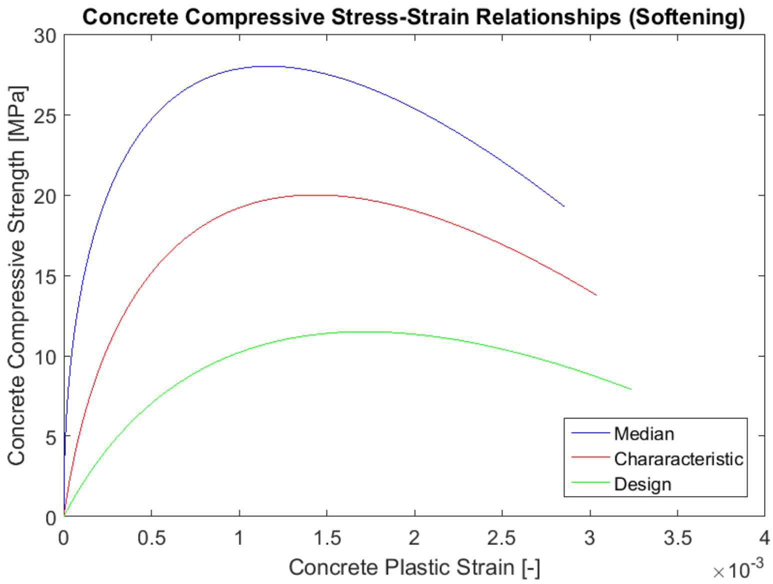


***Figure 4.13.*** Compressive Stress-Strain Relationships for softening response in function of plastic strains.

A perfect plastic response is however preferred since its implementation is simpler, and it does not significantly affect the solution. Moreover it also resembles more the parabola-rectangle stress distribution viewed in the previous chapter. The compressive stress-strain relationship for perfect plastic response in function of plastic strains is given in Fig. 4.14.

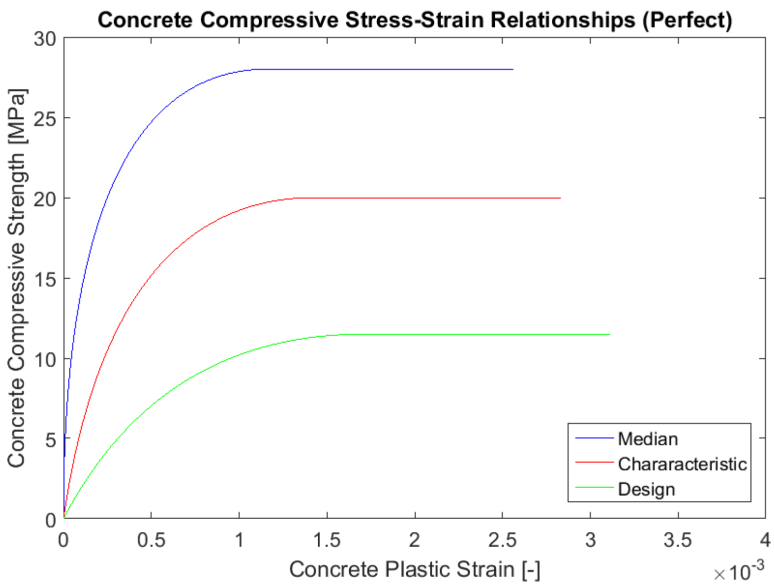


***Figure 4.14.*** Compressive Stress-Strain Relationships for perfect plastic response in function of plastic strains.

### 4.1.4 Cyclic Behavior

When the loads from static turn to dynamic the damage mechanics becomes much more complex. Cyclic behavior includes opening and closing of previously formed micro-cracks. Experimentally it is observed that the elastic stiffness partially recovers when the load changes sign in a cyclic load. Such stiffness recovery effect is usually referred in literature as unilateral effect, and it represents an essential aspect of concrete cyclic behavior.
The recovery is more conspicuous when load changes from tension to compression. [12]
The damage of Young's modulus is defined in function of the degradation variable $d$ as shown in Eq. 4.17.

$$E = E_0\,(1-d) \tag{4.17}$$

where

$E_0$ Initial undamaged Young's modulus [MPa]

The degradation variable is function of the stress state and compressive and tensile damage parameters, $d_c$ and $d_t$. Thus Eq. 4.18 follows.

$$(1-d) = (1-s_t d_c)(1-s_c d_t) \tag{4.18}$$

where

$s_t$ and $s_c$ Two parameters defining the stiffness recovery in function of stress reversals.

They are defined as in Eq. 4.19 and 4.20.

$$s_t = 1 - w_t\, r^*(\sigma_{11}) \qquad 0 \le w_t \le 1 \tag{4.19}$$

$$s_c = 1 - w_c\,(1 - r^*(\sigma_{11})) \qquad 0 \le w_t \le 1 \tag{4.20}$$

where

$\sigma_{11}$ Stress in a sample direction [MPa]
$r^*(\sigma_{11})$ $= 1$ if $\sigma_{11} > 0$
$r^*(\sigma_{11})$ $= 0$ if $\sigma_{11} < 0$

$w_t$ and $w_c$ are the, so called, weight factors which control the recovery of stiffness upon load reversal. [12].

To sum up with reference to Eq. 4.18 it can then be stated that the degradation of stiffness when cyclic loads are applied is mainly function of the compressive and tensile damage. The stiffness recovery is function of the weight factors, that for values of 0 introduce no recovery, and for values of 1 gives full recovery. Fig. 4.15 illustrates how damage parameter and weight factor affect concrete cyclic behavior. The concrete model is loaded in tension, and it is responding elastically, until it reaches its maximum tensile strength, corresponding to the point A. Within increasing strain the material is then softening until at the point B the model is unloaded. However at that stage the material stiffness is already damaged thus the unloading Young's modulus results to be smaller than the initial elastic one, and the rate of its reduction is determined by the damager parameter $d_t$. The unloading process brings the stress state from B to C, where there is a plastic strain. In case the material was not unloaded at B, it would have followed the dashed path, thus including tension stiffening in the model. At the point C the model is subjected to load reversal, and the weight factor $w_c$ determines the rate of stiffness recovery when going from tensile to compressive stress. For full recovery ($w_c = 1$) the Young's modulus coincides with initial elastic one. Upon compression load the material hardens and then softens as previously discussed. In case of no recovery ($w_c = 0$) the model would have followed the dashed stress path. At D the model is unloaded again, and the damage parameter $d_c$ determines the degradation of Young's modulus.
Upon unloading the stress is brought to zero at the point E, and plastic strain is present here as well since the strain is different from 0. At E the material is reloaded, and now again the tensile weight factor determines the stiffness recovery rate. However at this stage the tensile Young's modulus is already degraded in function of $d_t$ and $d_c$. No stiffness recovery is assumed, and the concrete is 'tension stiffening' again, and so on.

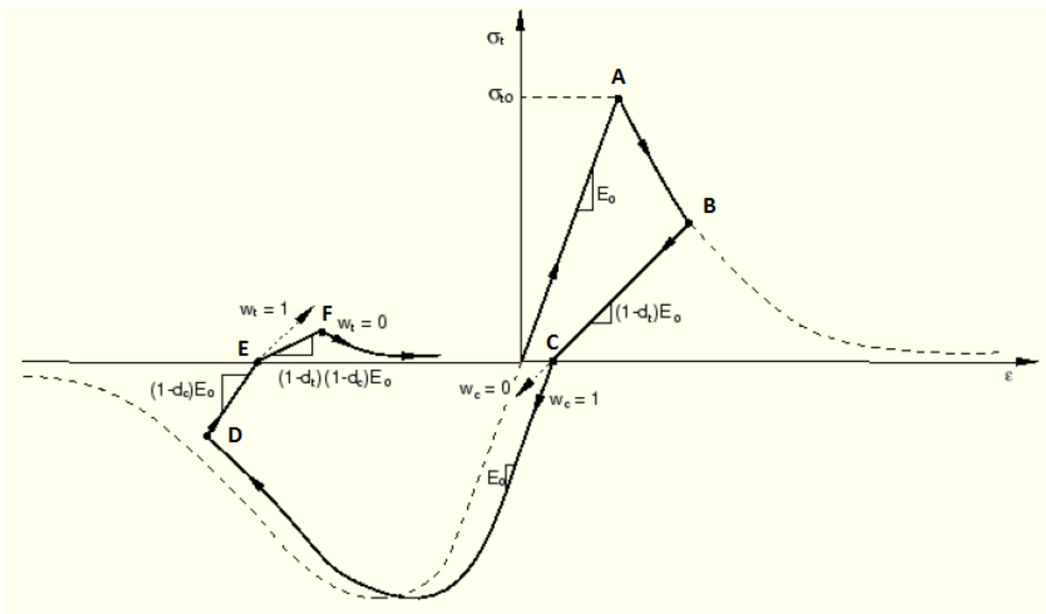


***Figure 4.15.*** Effect of damage parameters and weight factors on concrete cyclic behavior. [12]

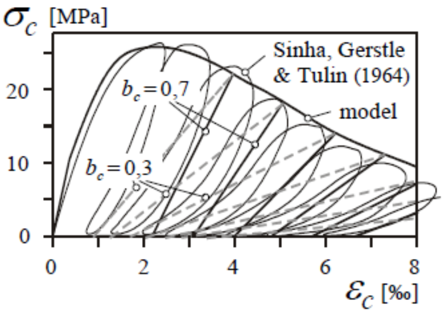


***Figure 4.16.*** Stress-strain relation for (cyclic) compressive loading. [13]

In order to implement the previously mentioned behavior into the FE model the damage parameters and weight factors have to be defined.
The evolution of the compressive damage component, as previously discussed, is directly linked to the plastic strains. Sinha, Gerstle & Tulun (1964) [13] proposed a relationship for deriving the compressive concrete damage parameter in function of the plastic strains, material properties, and a constant factor called $b_c$, with $0 \leq b_c \leq 1$. In Fig. 4.16 a representation of the cyclic behavior relationship is given for two different values of $b_c$. The $b_c$ parameter then seems to control the amount of damage to include in function of the plastic strains evolution. Sinha, Gerstle & Tulun (1964) chose a value of 0.7 since it seems to include damage more gradually and realistically into the model, and moreover their tests were carried out on a C20/25 concrete, thus perfectly fitting the current analysis.
The concrete damage parameter, $d_c$, is found through the relationship given in Eq. 4.21. [13]

$$d_c = 1 - \frac{\sigma_c \, E_c^{-1}}{\tilde{\epsilon}_c^{pl} \, (1/b_c - 1) + \sigma_c \, E_c^{-1}} \tag{4.21}$$

A representation of the obtained results for median, characteristic and design compressive strength values over inelastic strains is given in Fig. 4.17

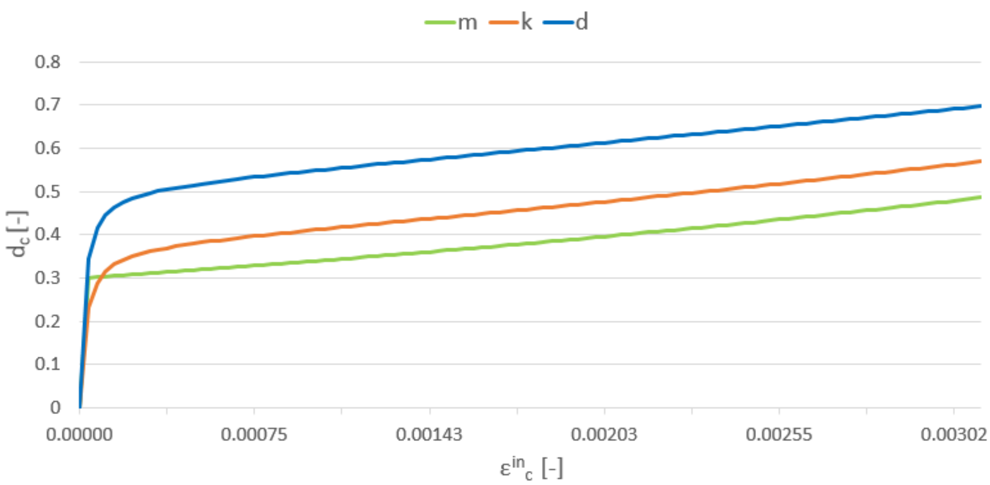


***Figure 4.17.*** Compressive damage parameter evolution with compressive inelastic strains.

The same concept applied for the tensile damage parameter. Fig. 4.18 gives an illustration

The evolution of the tensile damage component is directly linked to the tensile cracking strains. Reinhardt and Cornelissen (1984) [13] proposed a relationship for deriving the tensile concrete damage parameter. Such equation is based on the same principles as in Eq. 4.21, and it is given in Eq. 4.22. A constant factor, experimentally derived, called $b_t$, is introduced, and is set to be 0.1. [13]

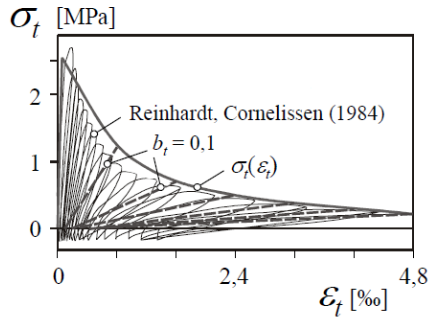


***Figure 4.18.*** Stress-strain relations for (cyclic) tensile loading. [13]

$$d_t = 1 - \frac{\sigma_t\ E_c^{-1}}{\tilde{\epsilon}_t^{pl}\ (1/b_y - 1) + \sigma_y\ E_c^{-1}} \tag{4.22}$$

A representation of the obtained tensile damage parameters over inelastic strains is given in Fig. 4.19

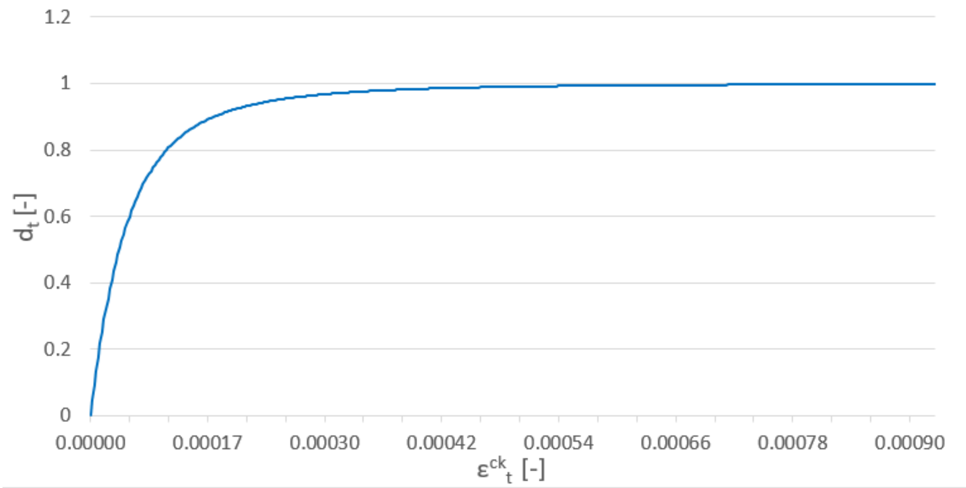


***Figure 4.19.*** Tensile damage parameter evolution with tensile cracking strains.

The weight factors used for modeling the stiffness recovery are given in Tab. 4.2. The compressive stiffness recovery is modeled with the maximum weight factor, while the tensile one with the lowest.

| Weight Factors | | |
|---|---|---|
| - | $w_c$ [%] | $w_t$ [%] |
| min | 10 | 70 |
| max | 20 | 80 |

***Table 4.2.***

## 4.2 Rebar Plastic Model

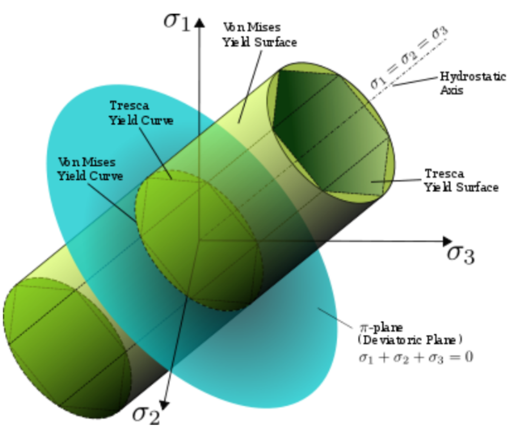


***Figure 4.20.*** Mises yield surface in a 3D principal stresses space. [16]

The definition of steel is carried out by assuming an elasto-plastic model with Mises yield surface, and associated plastic flow. Moreover the material model may also include either hardening or perfect plastic behavior.
The Mises yield criterion assumes yielding to be independent of the pressure stress since its shape does remains constant along the hydrostatic axis.
The Mises yield surface is defined by inputting the value of uniaxial yield stress as a function of the uniaxial equivalent plastic strain. [17] Isotropic hardening means that the yield surface changes size uniformly so that the yield stress increases in all the directions when plastic strains develop. [17]
In the case of analysis a perfect plastic behavior is preferred for modeling the rebars. Such model is chosen since it well fits the steel behavior. An illustration of the implemented model is given in Fig. 3.4. Moreover, for the rebar as well, the constitutive model needs to be expressed in function of plastic strains. The elastic part of the stress-strain relationship is thus removed, leading to a perfect plastic model as shown in Fig. 4.21.

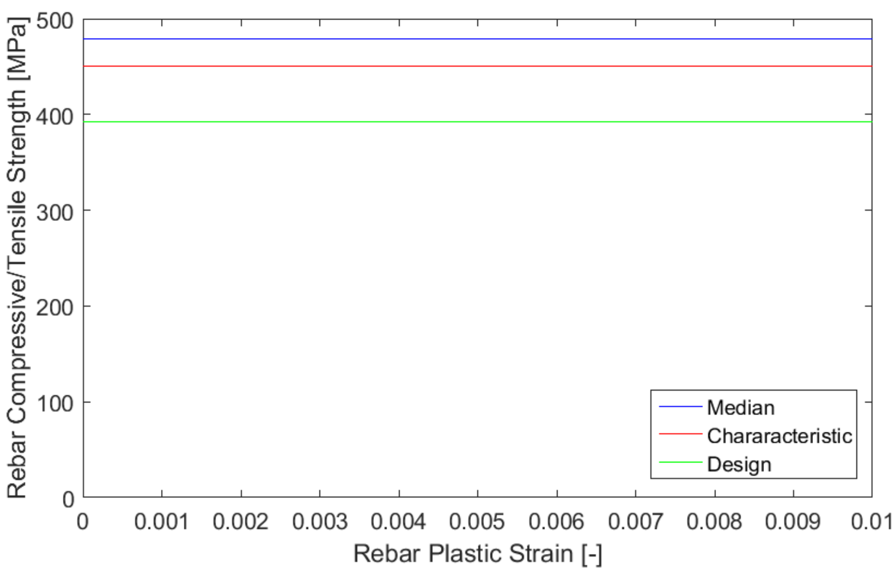


***Figure 4.21.*** Steel Perfect-Plastic Model in function of plastic strains.

# Static Non-Linear FE Analyses 5

*In this chapter the general framework on the basis of the non-linear FE analysis is introduced, with its relative solution method for time-independent problems. A shell and a solid model of the RC beam are built up. The finite elements constituting the models are illustrated. Finally the models' set-up and the results are shown and commented.*
*The FE analyses are carried out with ABAQUS/CAE*

## 5.1 Introduction to Non-Linear FE Analysis

In structural mechanics, as introduced in the previous chapter, materials may yield, harden or soften, leading to non-linearities in their constitutive models. Non-linear problems result to give more difficulties in describing them by realistic mathematical and numerical models. The analyst is required to put much more effort in non-linear analyses than for linear cases. Computational cost is also a big concern since the solving time is much increased.[18] Non-linearities can be introduced through material, contact and/or geometric non-linearities. For the case of analysis the constitutive models result to be non-linear, as discussed in the previous chapter, since plasticity is introduced to model concrete and steel behavior. No geometric non-linearities are given since the beam geometry is quite regular, and neither contact ones are present.
The usual FE equation implemented is given in Eq. 5.1

$$[K]\,\{D\} = \{R\} \tag{5.1}$$

where

| | |
|---|---|
| $[K]$ | Stiffness Matrix [N/mm] |
| $\{D\}$ | Displacement Vector [mm] |
| $\{R\}$ | Loads Vector [N] |

For non-linear FE analyses the solution cannot immediately be obtained for $\{D\}$ through Eq. 5.1 since informations are neededto construct $[K]$, and $\{R\}$ is now known a priori. An iterative process needs to be carried out to obtain $\{D\}$ and its connected $[K]$, such that equilibrium is provided through Eq. 5.1. [18] The satisfactory end of the above process for every iteration is usually argued in literature as solution convergence.
A further disadvantage on non-linear analysis is that solutions cannot be superposed since the equilibrium equations are non-linear.
The applied solution method is introduced as it follows.

### Time-Independent Solution Methods

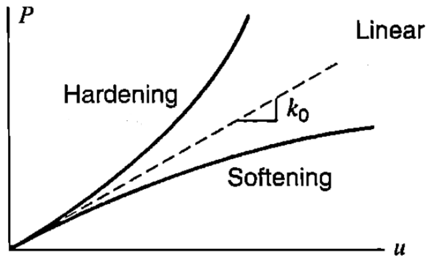


***Figure 5.1.*** Hardening and Softening behavior compared to a linear one. [18]

One of the iterative solution methods that can be applied for the previously introduced process is introduced for static problems.
The Newton-Raphson iterative method is given in the following, for more informations regarding other static solution methods please refer to [18].
Let's suppose to analyse a 1D problem where $u$ is the displacement, $k$ the stiffness, and $P$ the load. As shown in Fig. 5.1 the $k\ u$ provides a linear interpretation of the problem, however the relationship can either non-linearly harden or soften. It is clear that, if $P$ is known in advance, by applying Eq. 5.1 a solution for $u$ cannot be reached. The displacement, $u$, is instead obtained by iterations over increasing steps corresponding to load variations. The calculation procedure use the tangent stiffness $k_0$.
Fig. 5.2 gives an illustration of the Newton-Raphson iterations. The first iteration is carried out for a step-load of $\Delta P_1$ giving a load of $P_1$ with a tangent stiffness of $k_{t0}$. This latter intersect the load in $A$, at which a displacement of $a$ corresponds. However the load value at $a$ is lower than $P_1$ of a value of $e_{PA}$, thus the solution did not converge yet. Then in $a$ the tangent stiffness $k_{ta}$ is used. This latter brings the iteration to the point $B$ and subsequently to $b$, for which the load is still lower than $P_1$. The above process is carried out until the displacement corresponding to the point 1 is found. Another iteration is then required to find the values of $k$ and $u$ giving equilibrium. The implemented procedure is exactly alike the one previously introduced, and so on for more values of loads.

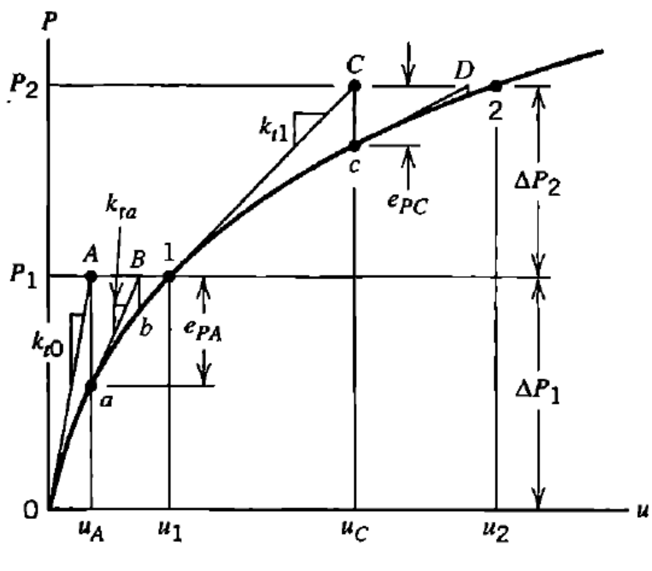


***Figure 5.2.*** Iterations procedure to convergence for two load levels $P_1$ and $P_2$. [18]

## 5.2 Finite Elements

A shell and a solid FE models are built up with the CDP model introduced in the previous chapter. The present section's aim is to introduce the FE which are implemented in the above mentioned models.

### 5.2.1 Shell Elements

Shell elements are characterized for having a significantly smaller dimension in the thickness direction than the other two dimensions. Shell FE analyses can be carried out either for thin or thick shell elements. Thin shell elements are described by classical Kirchhoff theory, while thick shell elements' kinematic relations are based on Reissner-Mindlin theory.[19]
For the current case thick elements are preferred since a shell model is used as an approximation of the RC beam, that in reality has a non-zero thickness.
The chosen shell section is homogeneous along the length of the beam, and it is defined by a shell thickness, a Poisson's ratio, rebar layers, and material models for concrete and steel. However the shell elements' thickness changes according to the FE analyses results in function of the defined Poisson's ratio $\nu$. Triangular and quadrilateral conventional shell elements could have been chosen for building up the shell model. Quadrilateral shell elements are however preferred since they can more accurately describe the bending behavior.
Moreover two different types of interpolation functions can be applied to the shell elements: linear and quadratic, respectively leading to the creation of the S4 and S8 elements, including 4 and 8 nodes. An illustration of such elements is given in Fig. 5.3. In the case of analysis the RC beam is mainly subjected to bending, thus quadratic elements shall give more accurate results since they can better represent such behavior. However acceptable results are also expected to be obtained from a linear elements mesh since the phenomenon of shear locking should not occur. The linear element may then be lock-free because they are bended in the direction perpendicular to their surface.

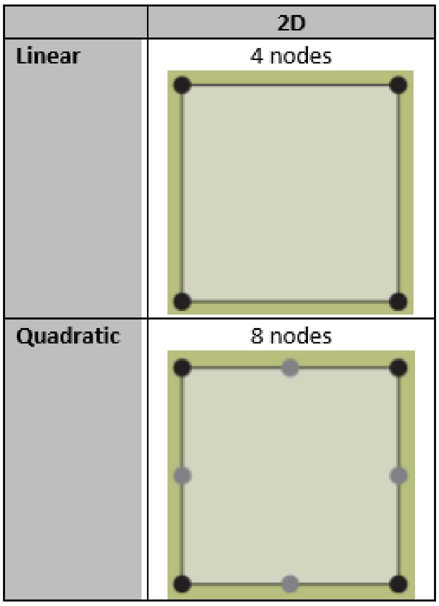


***Figure 5.3.*** Illustration of chosen elements for the shell model. [20]

Another important aspect in the choice of the shell elements is the integration method. For the case of a bending beam the strains linearly change along its thickness, and the stress distribution is assigned in correspondence to the strains' one. As previously illustrated the RC cross-section is subjected to negative (compressive) and positive (tensile) stresses when bending. The shell element provides informations only in the so called section points, which are the integration points along

the thickness.
If reduced integration is applied, meaning that only one integration point is used instead of four leading informations loss.
In this case is preferable to choose a greater amount of section points in order to better represent the bending behavior.
The position of the section points along the thickness of the beam is function of the chosen integration method.
Gauss quadrature integration tends to accumulate them to the edges in function of the amount of section points chosen. An illustration of such concept is given in Fig. 5.4.
The Simpson integration, shown in Fig. 5.5, give always an uneven amount of section points. This type of integration tends to place one section point always in the middle, and then equally distribute the resting points along the beam thickness.

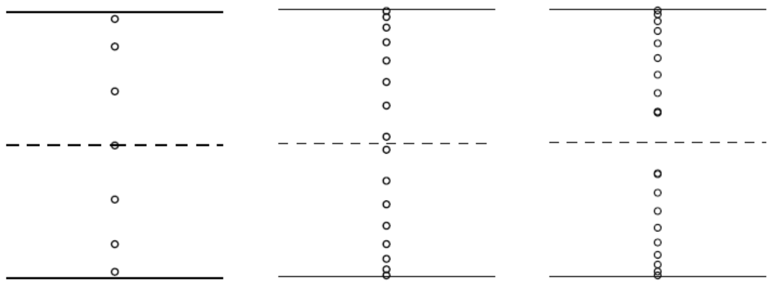

(a) 7 section points. (b) 16 section points. (c) 20 section points.

***Figure 5.4.*** Section points for Gauss quadrature integration. [21]

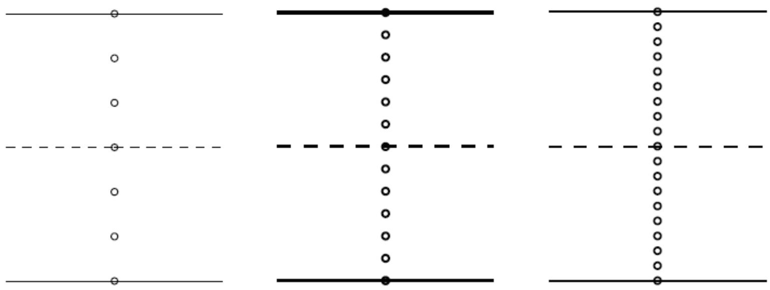

(a) 7 section points. (b) 17 section points. (c) 21 section points.

***Figure 5.5.*** Section points for Simpson integration. [21]

For the case of analysis the Simpson integration is preferred since it can better model the RC cross-section strain and stress distribution. An amount of 11 section points is taught to be sufficient, meaning that from top to bottom edge there is approximately one section point every 5.8 cm.
The position of the integration points in the quadrilateral element are not affected by the choice of using a Simpson integration, thus their position is equal to the one for Gauss quadrature integration. An illustration of their placement in isoparametric local coordinates is given in Fig. 5.6 (a).

Fig. 5.6 (b) is instead showing the position of the section points along the thickness for an example of 5 section points. Face SPOS and SNEG respectively refer to positive and negative surface.

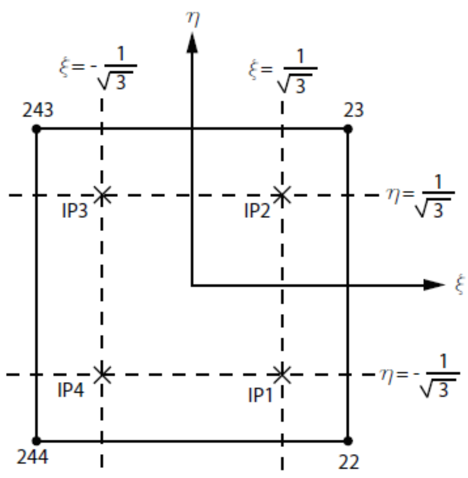


(a) Placement of Gauss points.

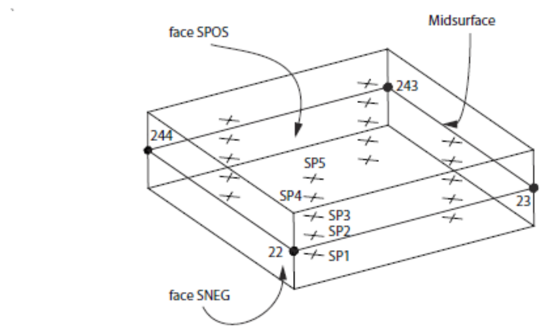


(b) Integration points and section points throught the thickness.

***Figure 5.6.*** Integration points in a quadrilater element. [19]

At last the rebar needs to be defined. Rebars are modelled through additional layers that can be oriented along the longitudinal direction of the beam, or either along the width one. Fig. 5.7 gives an illustration of the above mentioned concept. For the case of analysis two rebar layers need to be defined, since the RC beam geometry includes upper and lower rebars. To such layers is then assigned the elasto-plastic model for steel as outlined in the previous chapter.

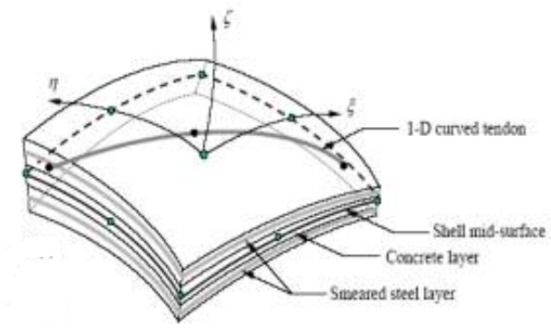


***Figure 5.7.*** Multi-layer shell element including rebars layers. [22]

The rebars layer are smeared on the whole rebars surface, which has size equal to the concrete one. According to the amount of rebar and to their area the layer is defined for providing equal steel area.

### 5.2.2 Solid Elements

In order to provide a more realistic and reliable solution a 3D FE model has to be created. The solid elements library provided by ABAQUS/CAE includes isoparametric elements. They are generally preferred for their cost-effectiveness. For a solid model the computational cost becomes of primary interest since the analysis turns to be way more complex. An illustration of the chosen solid elements is given in Fig. 5.8. Such elements are provided with a linear and quadratic interpolation function as well, and they are respectively referred as C3D8 and CRD20, including 8 and 20 nodes. The same concepts expressed for the first- and second-order interpolation function shell elements apply to the solid ones as well. Linear interpolation function elements give constant strain with the element, thus the final solution may be affected by the model mesh. Moreover the higher-order content of the solution is generally not very accurate. On the other hand quadratic interpolation function elements are capable to represent linear strain fields, and they are particularly effective for bending problems. [23]

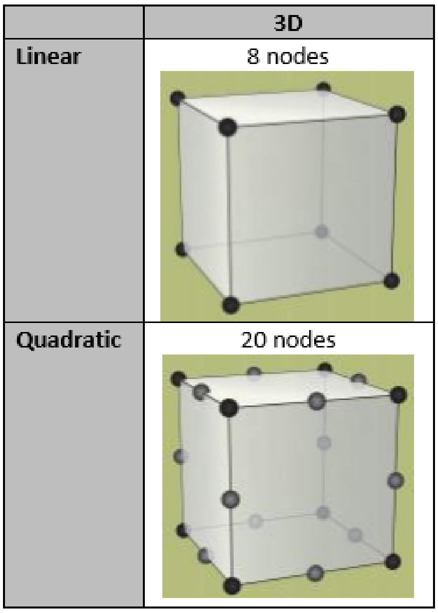


***Figure 5.8.*** Illustration of chosen elements for the solid model. [20]

First-order isoparametric elements also suffer 'shear locking' when performing in bending problems. They cannot provide a good bending solution since the linear interpolation function cannot describe accurately the problem, thus providing stiffer solutions. Such problem may be avoided by using reduced integration, but with the disadvantage of allowing spurious singular modes. Second-order isoparametric elements are locking-free, and, as previously introduced, their linear strain field can describe quite accurately bending behavior within thin FE. [23] An illustration of the physical meaning of linear and quadratic interpolation function is given in Fig. 5.9.

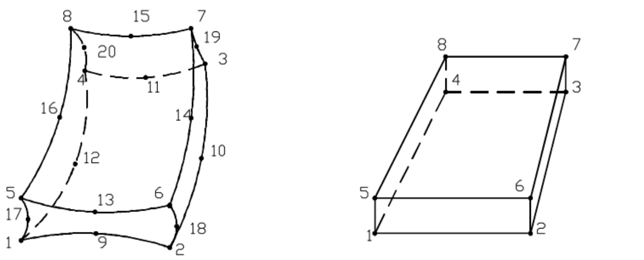


(a) C3D20 Element Type (b) C3D8 Element Type

***Figure 5.9.*** Illustration of first- and second-order interpolation function of solid elements. [24]

### 5.2.3 Truss Elements

In a 3D FE model solid elements are used to describe concrete regions, and truss elements are inserted for simulating the presence of rebars. in this context a 'truss element' is a 1D element that can randomly be oriented in a 3D space. Such element has one node at each extremity of the element, and it is able to transmit only axial forces. Fig. 5.10 gives an example of truss element. By definition trusses have no rotational degrees of freedom (DOF), they only have three translational DOF (depicted as $Dx$, $Dy$, $Dz$ in Fig. 5.10) per node. [25]

A cross-sectional area corresponding to the rebar is given to every truss element. Steel material properties, previously introduced, are also applied to them.

In RC concrete applications they are usually implemented in order to model rebar by embedding them to the concrete model. Their behavior is then entirely dependent on the concrete one.

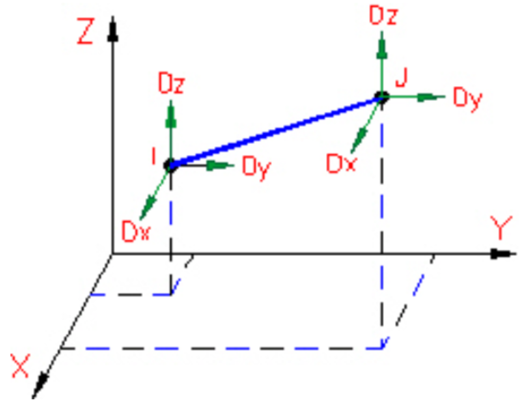


***Figure 5.10.*** Example of truss element randomly oriented in a 3D space. [25]

## 5.3 Shell Model Set-Up

The models are set up in the FE software Abaqus. Three models are built up including median, characteristic and design material properties, with its respective maximum loads previously computed in the ULS analysis.

The model set-up is shown in Fig. 5.11.

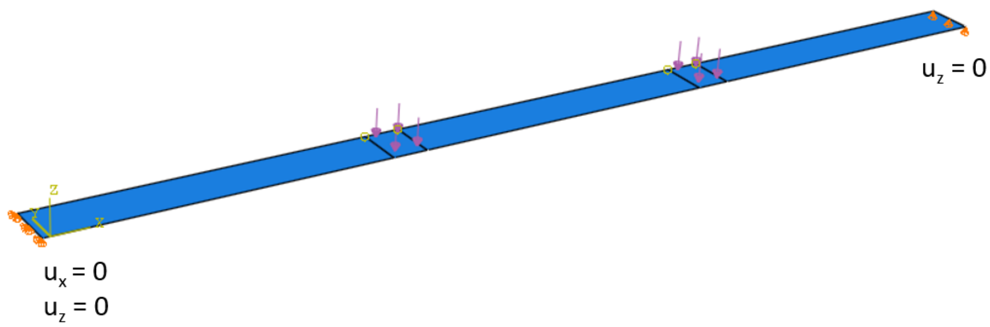


***Figure 5.11.*** Representation of Beam Shell Model Set-Up

The loads are applied over 200 mm wide areas (in the x-direction). The yellow-circled points are datum points, which are created in order to define the load area.

The boundary conditions impose no translational displacement in the x- and y-direction on one end of the beam, and no translational displacement in the y-direction on the other end.

Tension stiffening is introduced in the model through the stress-strain relationship illustrated in Fig. 4.9 with n = 1.5.

The mesh is defined simply by specifying a general elements size. An illustration of the bending behavior of the shell RC beam for the design case is given in Fig. 5.12

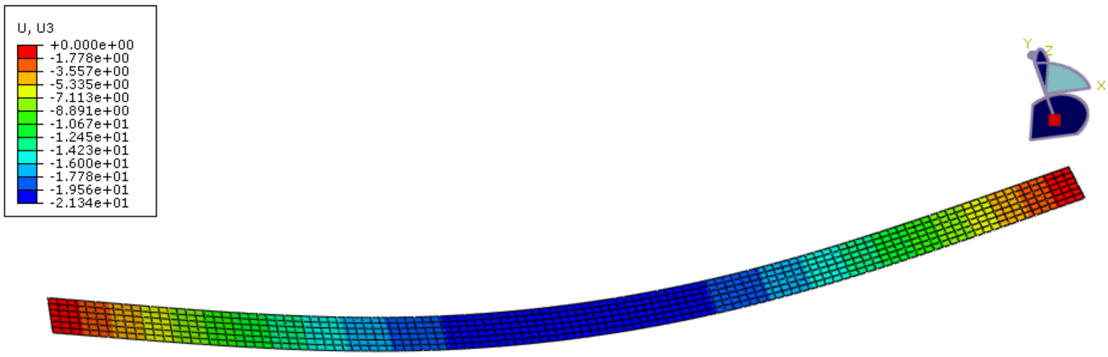


***Figure 5.12.*** Example of Beam Shell Model Deflection for the design case

## 5.4 Solid Model Set-Up

The solid model set-up results to be a little bit more complex than the shell one.
In this case the application of the boundary conditions directly on the model leads to unreliable bending results. When creating FE models it is the analyst's duty to ensure that the model behavior resembles its expectations. An illustration of the solid model set-up is given in Fig. 5.13.

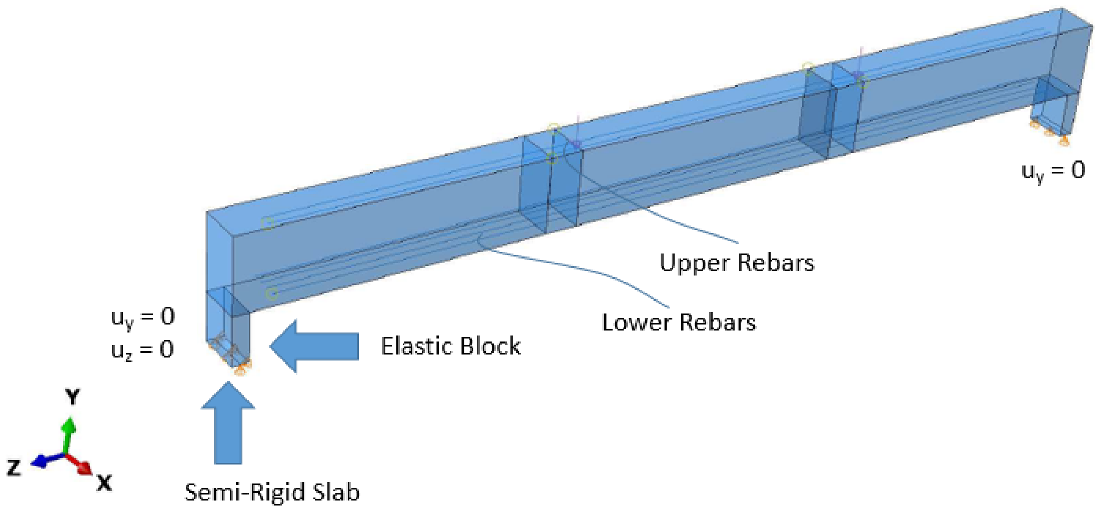


***Figure 5.13.*** Representation of Beam Solid Model Set-Up

The mesh is constituted over its height of 11 elements. The reason of such choice is that more elements are required along the beam height in order to well define the bending behavior. The amount of elements is defined matching the number of section points chosen for the shell model, in order to make better match the results.
The concrete beam is placed over two blocks made of 'elastic concrete'. Moreover such blocks are placed over shell slabs made of a semi-rigid material. The boundary conditions are applied on the bottom of such slab, and they are identical to the shell case.
With this model set-up the semi-rigid slab is capable of simply rotating around the pins without experiencing any deformation, the elastic blocks deform elastically and the RC beam follows such deformation providing a good bending behavior.
The parts are constrained by defining master and slave surfaces. The slave surfaces follow the deformations of the master surfaces.
The lower and upper rebars can also be seen in the model set-up above, and they are embedded into the concrete beam.
Tab. 5.1 underlines how the elastic, and semi-rigid materials are defined.

| Additional Materials for Solid Model Set-Up | | | |
|---|---|---|---|
| Part | Behavior | $E$ [MPa] | $\nu$ |
| Elastic Block | Elastic | 30000 | 0.20 |
| Semi-Rigid Slab | Elastic | 3000000 | 0.49 |

***Table 5.1.***

An illustration of the bending behavior of the RC beam is provided in Fig. 5.14 for the design case.

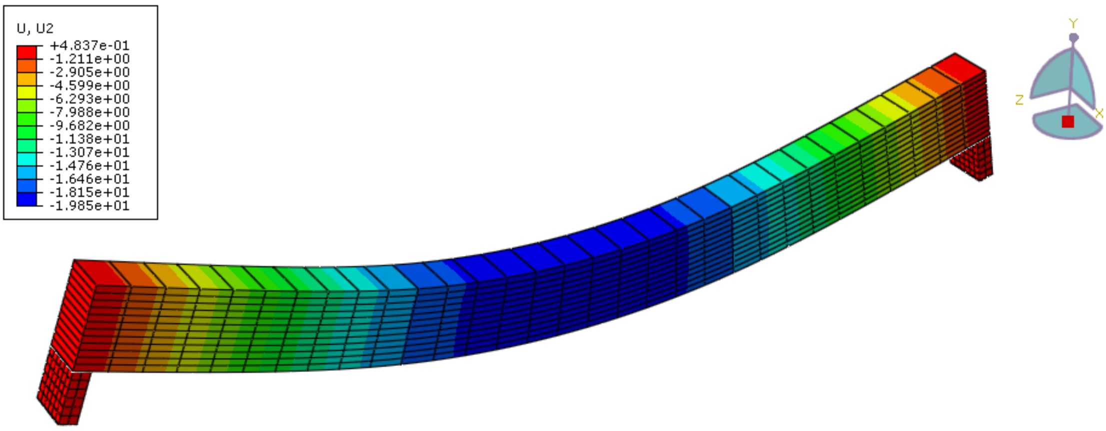


***Figure 5.14.*** Example of Beam Solid Model Deflection for the design case.

Due to the higher complexity of the model if the tensile behavior of concrete is given through the stress strain relationships, shown in Fig. 4.9, a converged solution results hard to reach. Thus the fracture energy approach is preferred for inserting tension stiffening in the model.

## 5.5 Analysis of the Results

In this section the results derived from the above mentioned models set-up are shown and discussed for both models.

### 5.5.1 Convergence Analysis

At first the convergence analysis is shown in order understand for both models which element is more effective and with how many elements.

For the shell model the used elements are shown in Fig. 5.15

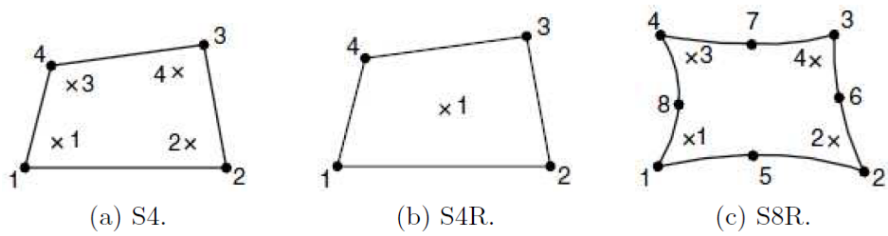


***Figure 5.15.*** Shell Elements used in the convergence analysis. [19]

The convergence analysis results for the shell model are illustrated in Fig. 5.16 and 5.17, and the rate of difference in terms of maximum vertical displacement ($u_{max}$) and computation time when increasing the seeds size are given in Tab. 5.2 and 5.3.

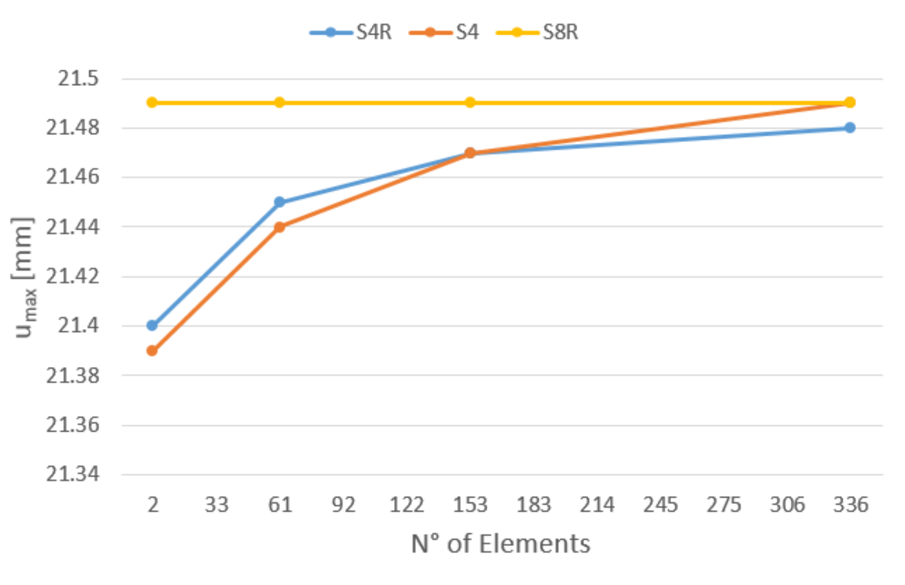


***Figure 5.16.*** Convergence Analysis for Shell Model

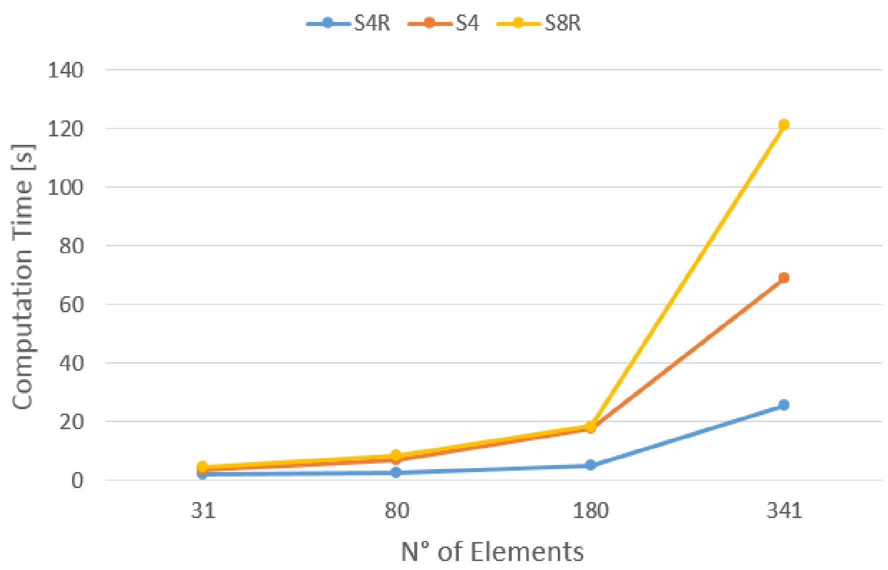


***Figure 5.17.*** Computation Time against Number of Elements for the Shell Model

| Convergence Rates of Vertical Displacements | | | |
|---|---|---|---|
| Elements Increase | S4R [%] | S4 [%] | S8R [%] |
| 31 - 80 | 0.23 | 0.23 | 0 |
| 80 - 180 | 0.093 | 0.14 | 0 |
| 180 - 341 | 0.046 | 0.093 | 0 |

***Table 5.2.***

| Percentages of increase of computation time | | | |
|---|---|---|---|
| Elements Increase | S4R [%] | S4 [%] | S8R [%] |
| 31 - 80 | 26.31 | 97.14 | 82.97 |
| 80 - 180 | 104.16 | 157.97 | 113.95 |
| 180 - 341 | 416.32 | 287.64 | 559.78 |

***Table 5.3.***

As it can be deducted the quadratic element offers the best performance since it converges way faster than the linear ones. The same result is obtained also using linear elements but only at the finest mesh. It is however important to notice that displacement results differ each other in the order of the second decimal number, and such a distance is not even visible by the human eye. Such statement is confirmed by the very low convergence rates of vertical displacements shown in Table 5.2.
An important aspect of FE modeling is also the computation time. The finest mesh constituted by S8 elements leads to way slower computations than the linear elements' case.

It can be noticed that the percentages of increase of computation time are generally very high when raising the amount of elements to the maximum one.
To conclude the S8 element provides the most precise results even with a coarse mesh, nonetheless the linear elements results are also judged to be reliable.

On the other hand the elements used for the solid model are illustrated in Fig. 5.18, 5.19, and 5.20.

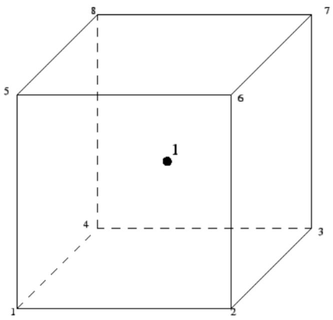

***Figure 5.18.*** CRD8R: 1x1x1 integration point scheme. [23]

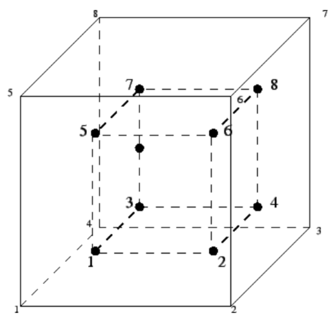

***Figure 5.19.*** C3D8: 2x2x2 integration point scheme. [23]

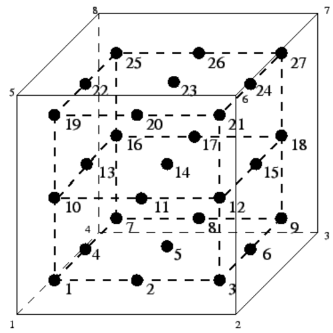

***Figure 5.20.*** C3D20: 3x3x3 integration point scheme.[23]

The convergence analysis results for the solid model are illustrated in Fig. 5.21 and 5.22, and the rate of difference in terms of maximum vertical displacement and computation time when increasing the seeds size are given in Tab. 5.4 and 5.5.

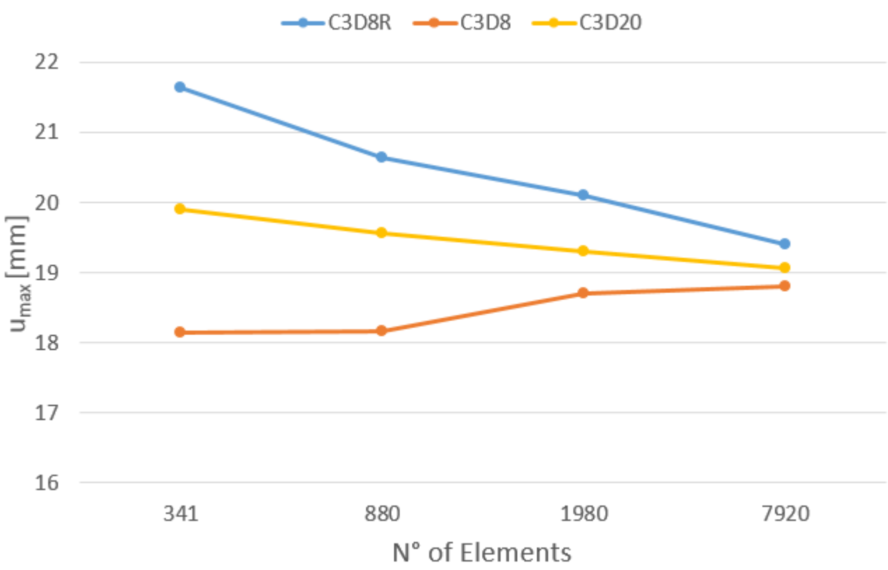


***Figure 5.21.*** Convergence Analysis for Solid Model

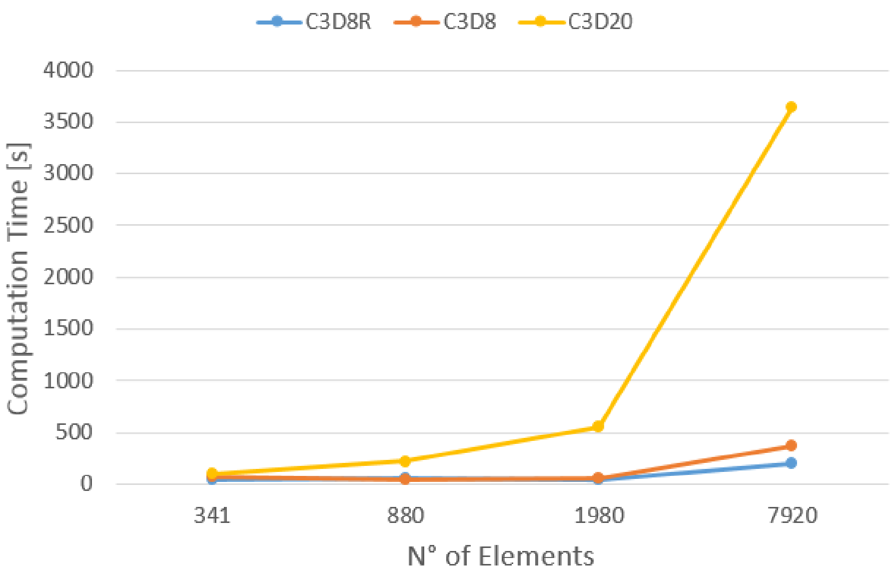


***Figure 5.22.*** Computation Time against Number of Elements for the Solid Model

| Convergence Rates of Vertical Displacements | | | |
|---|---|---|---|
| Elements Increase | C3D8R [%] | C3D8 [%] | C3D20 [%] |
| From 341 to 880 | -4.57 | 0.11 | -0.017 |
| From 880 to 1980 | -2.66 | 2.97 | -0.013 |
| From 1980 to 7920 | -3.48 | 0.53 | -0.012 |

***Table 5.4.***

| Percentages of increase of computation time | | | |
|---|---|---|---|
| Elements Increase | C3D8R [%] | C3D8 [%] | C3D20 [%] |
| From 341 to 880 | 11.51 | -43.93 | 1.37 |
| From 880 to 1980 | -4.25 | 65.67 | 1.54 |
| From 1980 to 7920 | 312.26 | 489.88 | 5.53 |

***Table 5.5.***

From the convergence analysis it can clearly be seen that both linear and quadratic elements mesh tend to converge with increasing amount of elements. In this case the rates of convergence are higher. The results difference is also more evident, for example for the coarsest mesh the vertical displacements are between a range of around 18 mm to almost 22 mm. For an amount of elements even higher than 7920 the results would have probably converged even more. However the convergence analysis is stopped at such point since the computation time already increased dramatically. It is curious to notice that in some case by increasing the amount of elements the computation time decreases, meaning that the

solutions convergence, at each step, sometimes tend to be faster with finer mashes.
A mesh constituted by C3D20 elements converges faster, in fact its convergence rate is within the second decimal number. However in general solid models computations result to be slower.
To sum up, for the solid model as well, the more reliable results are provided by the quadratic elements. Linear elements' results are also precise, but only with the finest mesh.

### 5.5.2 The Influence of Rate of Weakening

In this subsection the influence of the rate of weakening on shell model results in terms of normal stresses and vertical displacements is investigated.
As previously introduced the rate of weakening ($n$) affects the tensile behavior of concrete, defined through Eq. 4.10.
The stress distributions for different values of $n$ is given in Fig. 5.23, 5.24, 5.25, 5.26, and 5.27.

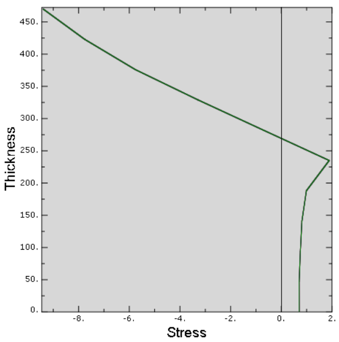


***Figure 5.23.*** Normal Stress Distribution for $n = 0.4$

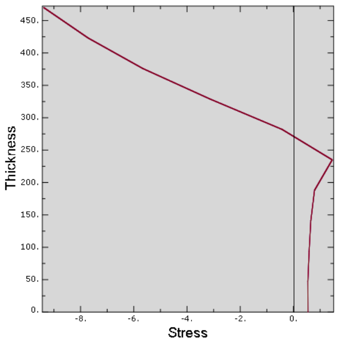


***Figure 5.24.*** Normal Stress Distribution for $n = 0.5$

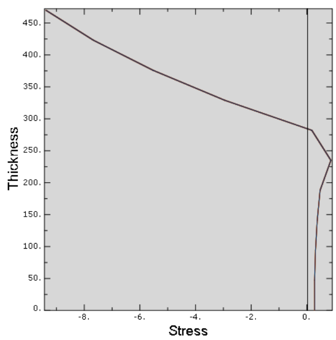


***Figure 5.25.*** Normal Stress Distribution for $n = 0.75$

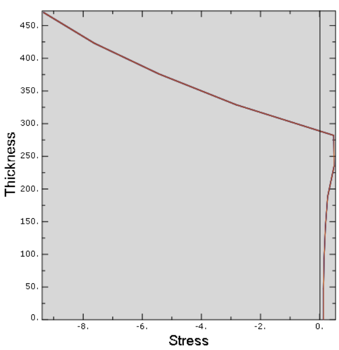


***Figure 5.26.*** Normal Stress Distribution for $n = 1$

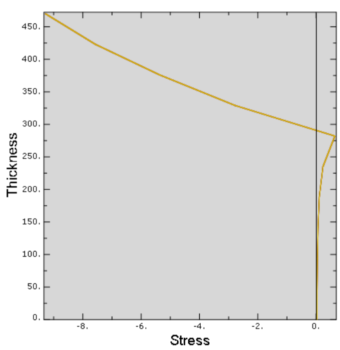


***Figure 5.27.*** Normal Stress Distribution for $n = 1.5$

As expected the normal stresses are affected, especially in tension, by the change of rate of weakening. The tensile stress distributions resemble the curves illustrated in Fig. 4.8, which also match the a priori expectations.
The compressive normal stresses should also be affected by a variation of $n$, or, more logically, by a change in tensile stresses. As the positive (tensile) stresses vary, the negative ones also have to change in order to satisfy normal equilibrium conditions. However the above figures evidence a very small difference in terms of compressive stresses. Almost no variation is given since as concrete carries less and less tensile stresses, the rebar 'absorbs' such loss of stresses, thus no increase in concrete compressive stresses is required.
The influence of $n$ on the maximum vertical displacements ($u_{max}$) is shown in Fig. 5.28

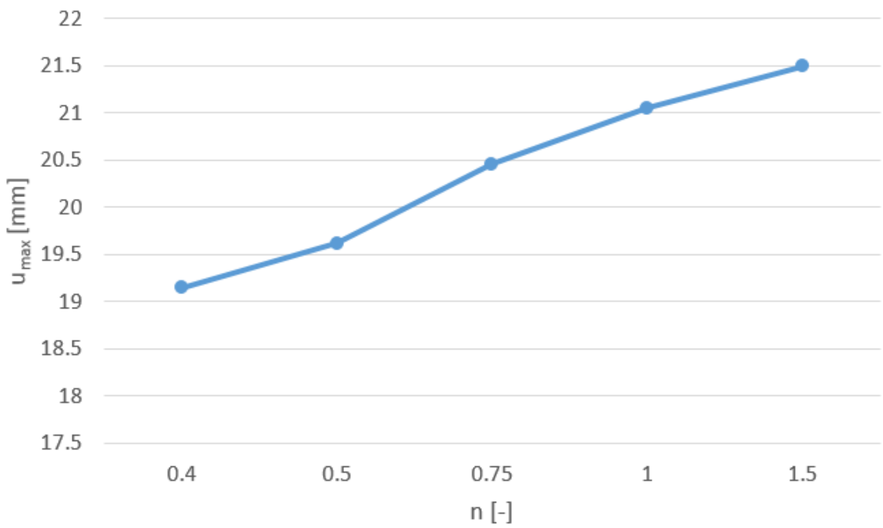


***Figure 5.28.*** Maximum Vertical Displacement values with varying rate of weakening.

According to what was previously introduced by raising $n$ the contribution of concrete in tension decreases, and the one of the rebars increase. The above results also give good physical sense since once the rebars are in plastic zone the strains increase more rapidly, thus introducing more ductility in the model, and providing higher displacements. Fig. 5.28 shows that in the case of analysis the same thing is happening.

### 5.5.3 The Influence of Fracture Energy

In this subsection the influence of fracture energy on solid model results in terms of normal stresses and vertical displacements is investigated.
By increasing or decreasing the fracture energy in the model the displacement required for producing fractures respectively increases or decreases linearly according to the relationship given in Fig. 4.10.
A physical representation of such concept is given by Fig. 5.29 on a tensile displacement, $u_t$, tensile strength, $\sigma_t$ graph.

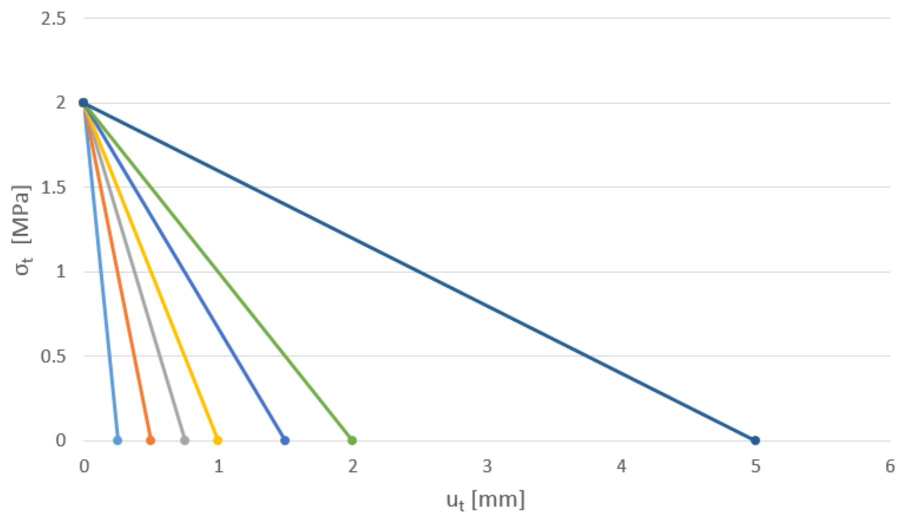


***Figure 5.29.*** Representation of different fracture energies on a stress against displacement graph.

$G_f$ also regulates the amount of tension stiffening to include in the model through the decreasing tendency of tensile stress. For decreasing values of fracture energy the tensile stresses in concrete get lower, thus providing higher displacement, and slightly higher compressive stresses. Such concept is identical to the one expressed for the shell model with the rate of weakening.
The maximum normal compressive stresses, $\sigma_{c,max}$, and vertical displacements, $u_{max}$, are plotted in function of varying values of $G_f$ in Fig. 5.30

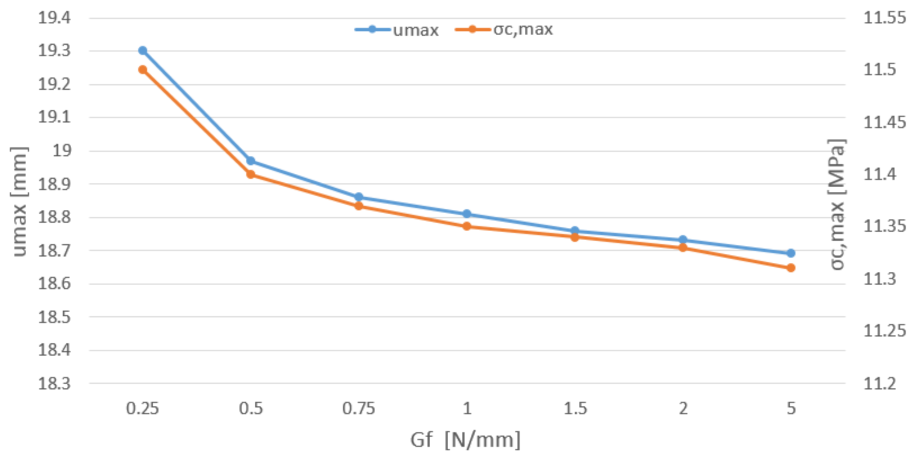


***Figure 5.30.*** Maximum compressive stresses and vertical displacements against fracture energy.

The above mentioned expectations are met, and in this case as well the compressive stresses variation is not high due to the presence of rebars. On the other hand the RC beam displacement difference between minimum and maximum fracture energies is of the order of about 1 mm.

### 5.5.4 Comparison of Shell and Solid Models Results

In this subsection the obtained results for the two previously introduced FE models are presented and discussed.
At first the FE analyses are carried out with respect to the maximum loads based on the ULS calculations, deriving then the maximum vertical displacement ($u_{max}$). However the two models' bearing capacities are found to be slightly higher than the ones at the ULS. Another analysis is thus carried out for deriving the value of the maximum loads the two FE models can carry ($P_{max}$), and the maximum normal compressive stress ($\sigma_{c,max}$).
The above mentioned analyses are performed for median, characteristic and design values (d, k, m) of concrete compressive strength ($f_c$), and rebars strength ($f_y$). The obtained results for the shell and solid models are given in Tab. 5.6, and the percentages of difference between shell and solid results are summarized in Tab. 5.7.

| Shell Models Results | | | | | |
|---|---|---|---|---|---|
| - | $f_c$ [MPa] | $f_y$ [MPa] | $u_{max}$ [mm] | $\sigma_{c,max}$ [MPa] | $P_{max}$ [kN] |
| d | 11.5 | 391.3 | 21.5 | 11.2 | 69.8 |
| k | 20.0 | 450.0 | 22.9 | 19.0 | 84.8 |
| m | 28.0 | 479.2 | 26.9 | 23.5 | 89.7 |
| Solid Models Results | | | | | |
| d | 11.5 | 391.3 | 19.1 | 11.4 | 72.1 |
| k | 20.0 | 450 | 19.8 | 19.8 | 88.6 |
| m | 28.0 | 479.2 | 22.6 | 25.1 | 94.0 |

***Table 5.6.*** Comparison of Shell and Solid FE Models Results

| - | $u_{max}$ [%] | $\sigma_{c,max}$ [%] | $P_{max}$ [%] |
|---|---|---|---|
| d | 11.30 | -3.84 | -3.36 |
| k | 13.36 | -4.31 | -4.45 |
| m | 15.98 | -7.02 | -4.85 |

***Table 5.7.*** Percentages of difference between Shell and Solid Models' Results

From the above tables good similarities can generally be appreciated between the FE models results.
Roughly the solid model appears to be stiffer than the shell one, thus providing lower displacements, and higher stresses and maximum bearing load, which makes good physical sense. However the solid model is more accurate than the shell one, thus its behavior provides more likely a better representation of the RC beam behavior.
The maximum vertical displacements biggest difference is noted for the median strengths case with 4.3 mm, corresponding to a 15.98 % difference. Moreover the difference in terms of $\sigma_{c,max}$ and $P_{max}$ is even lower, confirming once more a good match between the two

models.
However it can also be noticed how the maximum concrete compressive strengths of the solid models got closer to the $f_c$ values depicted in Tab. 2.2.

# Comparison of Static Analyses Results 6

*In this chapter the obtained results from ULS, SLS and FE analyses are compared and analyzed. The applicability of the used methods is also discussed. Finally the RC beam behavior under monotonic load is shown.*

## 6.1 Stresses and Displacements Comparison

The obtained results are presented through values of maximum vertical displacement, bearing loads, and compressive stresses. The limit state and FE analyses are carried out for design, characteristic and median values of strength of concrete and steel. Fig. 6.1 shows values of $u_{max}$ for varying concrete compressive strengths.

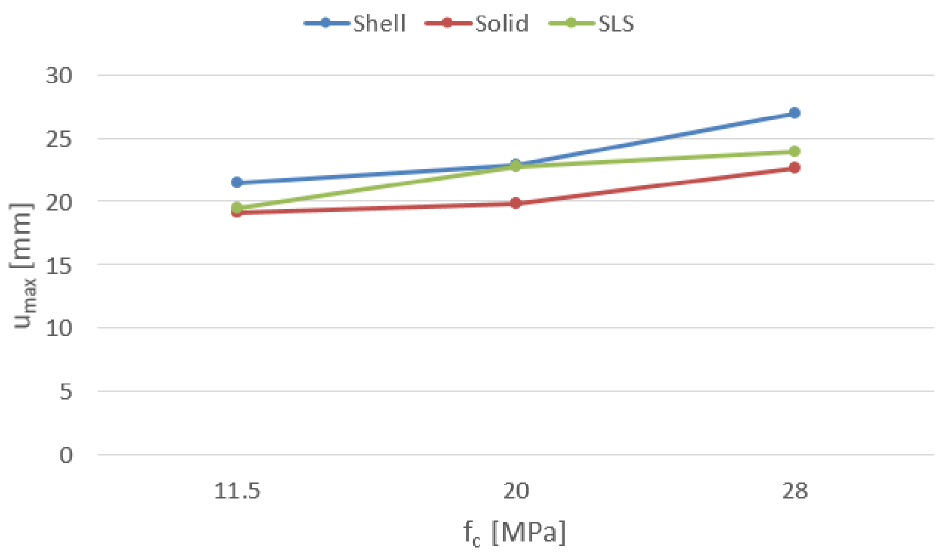


***Figure 6.1.*** Maximum vertical displacement values from SLS, and FE analyses in function of concrete strength.

The SLS displacements are between the ones obtained for shell and solid FE models. However the results show generally a good match in terms of displacements.
It is also clear how the behavior of the beam is affected by the materials strength definition. It can be noticed how the FE models results follow more or less the same trend, while that is not the case for the SLS ones. Such statement gives confirmation that the definition of concrete and steel strengths affects the results depending on the type of analysis that is carried. FE and limit state methods are respectively analytical and numerical, thus their different approach justifies the detected divergent behaviors.

Fig. 6.2 illustrates values of maximum bearing loads in function of concrete strengths.

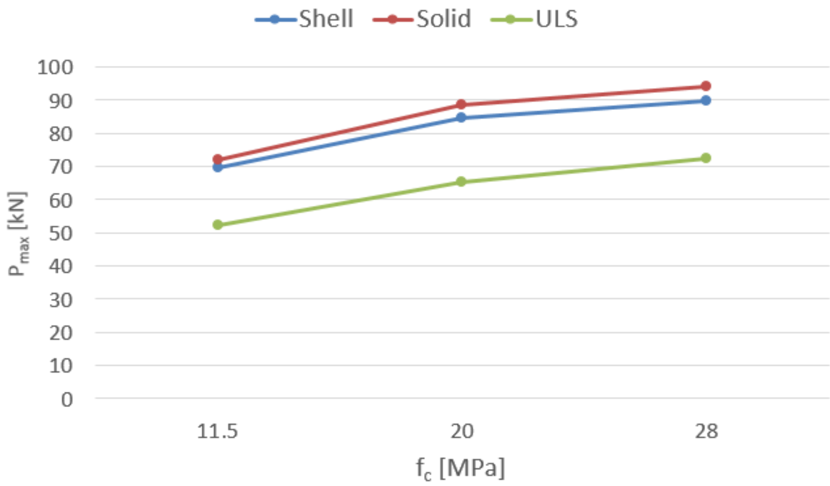


***Figure 6.2.*** Maximum bearing load values from ULS, and FE analyses in function of concrete strength.

From the above results it can be appreciated an higher bearing capacity of the FE models. The ULS calculations are less accurate than the FE ones. The limit state approach is however on the 'safe side' since its values of $P_{max}$ are lower, which is in accordance with the Eurocode 2 design principles. As it was already discussed in the last chapter the solid model bearing capacity is slightly higher than the shell one.
Fig. 6.3 depicts the maximum compressive stresses ($\sigma_{c,max}$) in function of the bearing loads. Also in this case the two approaches give a good match. It can be observed good similarity between the two FE analyses' trends.

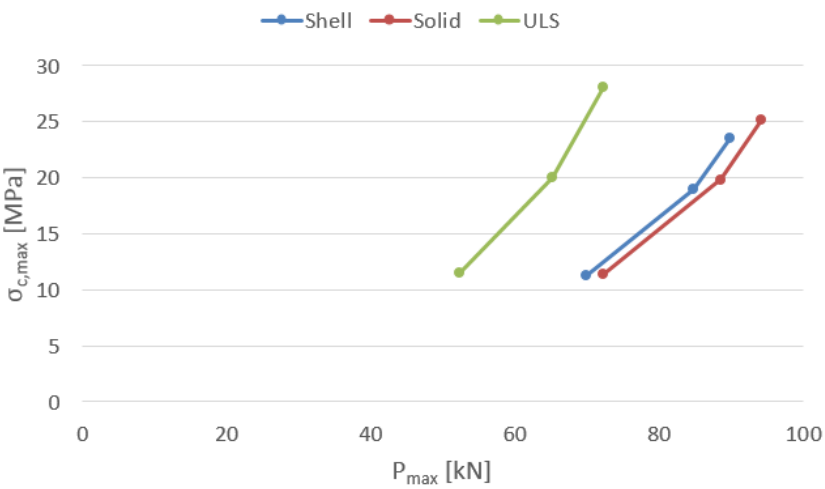


***Figure 6.3.*** Maximum compressive stress values from ULS, and FE analyses in function of maximum bearing loads.

## 6.2 RC Beam Behavior due to Monotonic Loading

In this section the behavior of the beam due to monotonic loading is discussed. Such analysis is carried out by extracting the FE results at certain load steps corresponding to given percentages of the maximum bearing load. The figures below show the normal stress distribution for monotonically increasing loading.

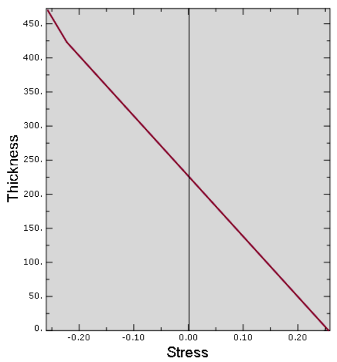


***Figure 6.4.*** Normal Stress Distribution for a load of 2% of $P_{max}$.

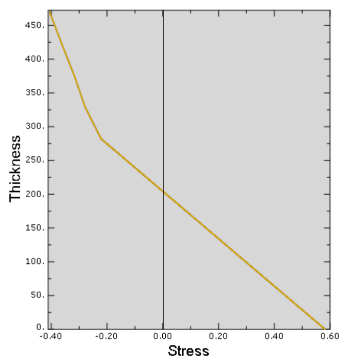


***Figure 6.5.*** Normal Stress Distribution for a load of 5% of $P_{max}$.

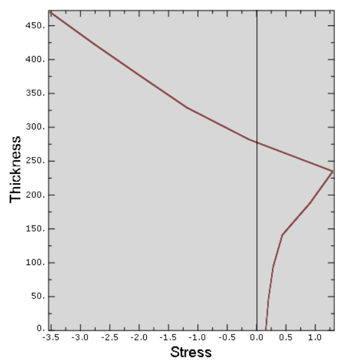


***Figure 6.6.*** Normal Stress Distribution for a load of 24% of $P_{max}$.

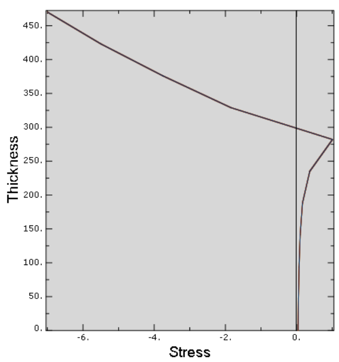


***Figure 6.7.*** Normal Stress Distribution for a load of 50% of $P_{max}$.

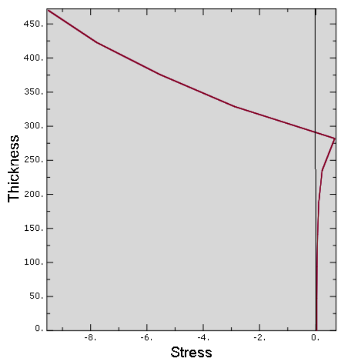


***Figure 6.8.*** Normal Stress Distribution for a load of 77% of $P_{max}$.

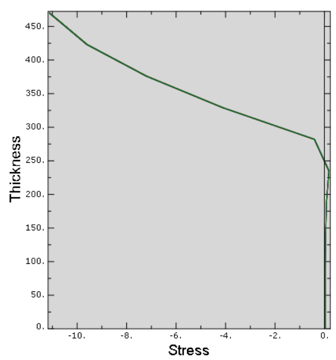


***Figure 6.9.*** Normal Stress Distribution for a load of 100% of $P_{max}$.

In Fig. 6.4 the normal stress distribution is depicted for the 2 % of the maximum bearing load. It can be seen an linear elastic behavior in tension, meaning that tensile cracking did not occur yet. In compression the concrete behavior is also linear with a slight change of slope close to the upper edge, meaning probably that plasticity is occurring.
In Fig. 6.5 the load is increased by a 3%, the tensile behavior is still linear elastic, while the previously mentioned change of slope becomes more pronounced.
In Fig. 6.6 at a load of 24 % the compressive stress distribution is clearly non-linear, while the maximum tensile strength is now reached.

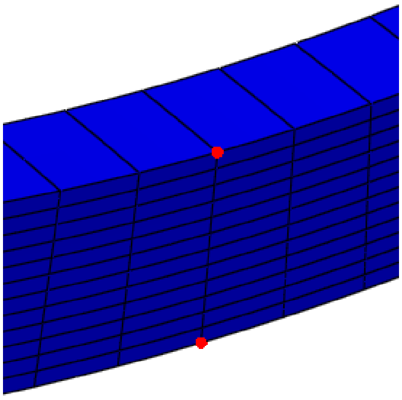

***Figure 6.10.*** Illustration of points in which the stresses are tracked at mid-length of the beam.

At this step tension stiffening is thus included in the model. By further increasing the load until 50%, as shown in Fig. 6.7, the shape of the stress distribution remains more or less alike, with a raise of tension stiffening since the tensile stresses get closer to 0.
In Fig. 6.8 and 6.9 the load is brought up to, respectively, 77% and 100%. Within the load augmentation the compressive stresses tend to increase, and the tensile ones to decrease. The normal stress distribution with a load of $P_{max}$ represents the RC beam behavior when carrying the maximum bearing load, and it resembles very much the ULS stress profile.

Fig. 6.11 shows the evolution of tensile ($\sigma_t$) and compressive ($\sigma_c$) stresses with monotonic loading at the lower and upper edges at mid-length of the beam, as shown in Fig. 6.10.

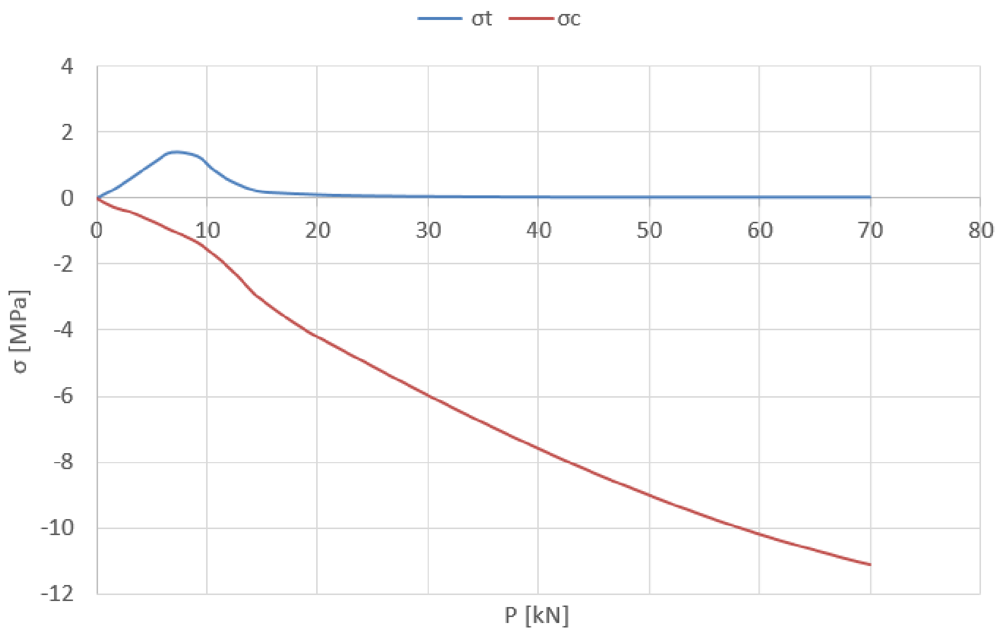


***Figure 6.11.*** Compressive and tensile stresses evolution with monotonic loading.

Through the above figure informations can be extracted on the load step at which plasticity is introduced in the model in tension and in compression.
The blue line represents the tensile stresses, and it shows an almost linear increase until a load of about 7 kN. For higher loads the model responds plastically with the tensile stresses tending asymptotically to 0.

The interpretation of the compressive stresses, depicted by the red line, results however to be harder. Non-linearities can be appreciated from a load of about 2 kN, giving reason to the small non-linearity evidenced in Fig. 6.4.
Then it seems that the curve starts following the same non-linear trend from a load of about 14 kN. An explanation for this phenomenon can be given by comparing Fig. 6.5 and 6.6. They both include plasticity in the compressive behavior but with different shapes. By then looking at Fig. 6.6, 6.7, 6.8 and 6.9 the compressive stress distribution maintains the same shape, corresponding to the non-linear trend previously mentioned.

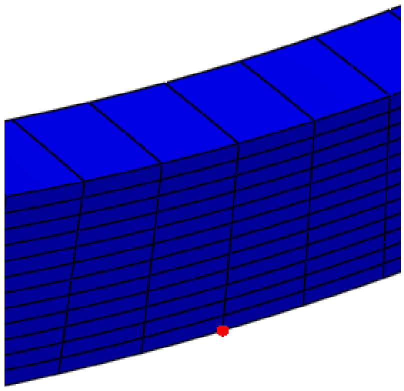

***Figure 6.12.*** Nodal point where the load-displacement data are tracked at mid-length of the beam.

Finally data regarding load-displacement for median, characteristic and design values of materials strength are extracted and plotted in Fig. 6.13. The chosen nodal point from data extraction is the one giving maximum displacement, placed at the mid-length of the beam, and it is evidenced in Fig. 6.12.

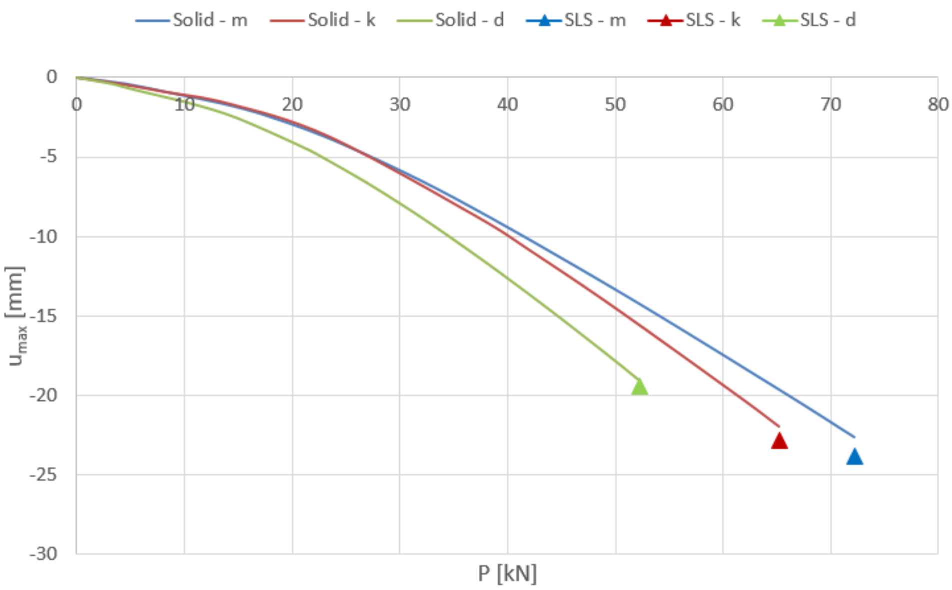


***Figure 6.13.*** Load-displacement curves representation.

The above load-displacement curves make good physical sense since for a given value of load the displacements result always higher for the case of lower materials strengths.
Fig. 6.13 also includes the displacements derived through the SLS analysis, which result to almost coincide with the last point of the curves.

# Dynamic Non-Linear FE Analyses 7

*In this chapter a dynamic non-linear FE analysis is carried out for a RC column. Two FE models are created using shell and solid FE. The eigenfrequencies of the column are evaluated through a modal analysis, and damping is defined. The compressive and tensile damage parameters are computed in order to describe the cyclic behavior in concrete. Finally the earthquake excitation is adjusted with reference to such eigenfrequencies in order to provoke resonance in the structure.*

For a dynamic non-linear analysis it is preferred to analyse a column instead of a beam. The reason of such choice is that a column is the structural element to which the earthquake excitation is directly applied. Moreover buildings failure due to earthquakes usually occurs at first in the column.
The column cross-section is illustrated in Fig. 7.1, and its geometrical properties are given in Table 7.1. The column height is 3.2 m. The materials used for modeling concrete and steel are the same as for the beam, thus respectively C20/25 and B450C. In this case the design value of such properties, given in Tables 2.2 and 2.3 are chosen.

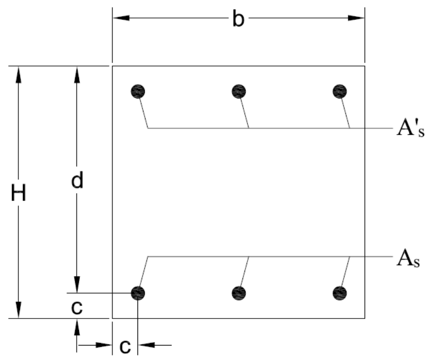


***Figure 7.1.*** Representation of column cross-section.

| Cross-Section Properties | | | | |
|---|---|---|---|---|
| $b$ [mm] | $H$ [mm] | $c$ [mm] | $d$ [mm] | $A_s = A'_s$ [mm$^2$] |
| 450.0 | 450.0 | 45.0 | 455.0 | $3\phi12 = 339.1$ |

***Table 7.1.*** Column Cross-Section Properties as indicated in Fig. 7.1

## 7.1 Time-Dependent Solution Methods

In dynamic analyses the structure is subjected to a time-dependent load or displacement. To each time step a certain value of load or displacement is associated. The FE approach is implemented in order to find an equilibrium configuration at every time step.
In this case a dynamic analysis is carried out for modeling the structure response to an earthquake excitation, which is applied in terms of time-dependent displacements.
The FE models are built in the software Abaqus, and a dynamic implicit approach is chosen.
In this latter a set of equilibrium equations are solved at each time increment.
When analyzing the dynamic response of a structure with elastic material properties the FE approach is simply applying such equilibrium equations, as shown in Eq. 5.1, linear in this case. Thus the global equations of motion are simply integrated through time for a defined time step increment.
When turning to non-linear FE analyses, as previously introduced in the static case, the problem becomes more complex. In such case Newton-Raphson iterations, illustrated in Fig. 5.2, are used to find the equilibrium configuration at each time step.
To sum up the time-dependent solution method for both cases, linear and non-linear, is alike the one implemented in the static case, and is integrated through time

## 7.2 Shell Model Set-Up

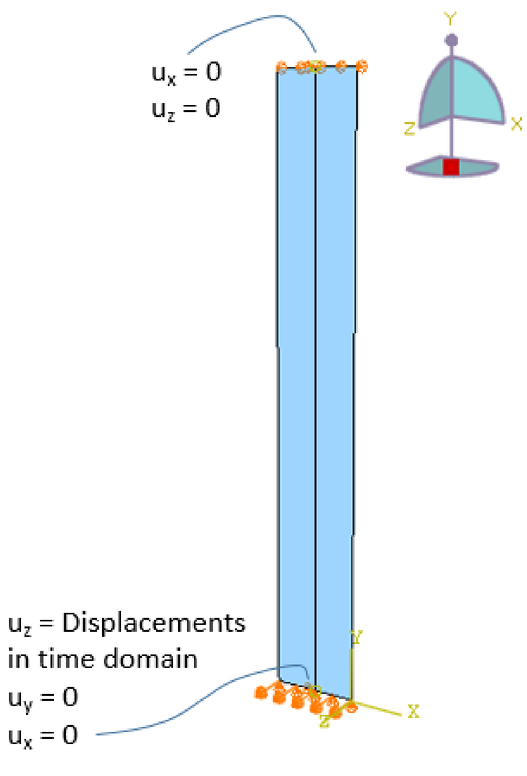


***Figure 7.2.*** Representation of Column Shell Model set-up.

The shell model set-up is presented in this section. A representation of this latter is given in Fig. 7.2.
The applied boundary conditions are also illustrated.
The displacement in the x-direction is constrained in the middle points at the upper and lower edge of the column. Then at the upper edge the displacement is constrained also in the z-direction over the whole column width. In this way the structure is free to rotate around the x-axis. At the lower edge, over the column width, the displacement is constrained in the y-direction and time-dependent displacements are applied in the z-direction.

Quadratic elements (S8), as illustrated in Fig. 5.3, are chosen since they better fit the bending behavior of the column even though they lead to an increase in computation time.
Regarding the mesh only two elements are used over the column width since the core of the analysis is the bending behavior which takes place in the z-direction and around the x-axis.
The model is built up with an amount of integration points over its thickness of 9, as for the beam model. Such choice is justified by the fact that since the earthquake excitation is applied in the z-direction an higher amount of integration points over the thickness would lead to a better interpretation of the bending behavior.
Rebars along the column height are also inserted in the model.

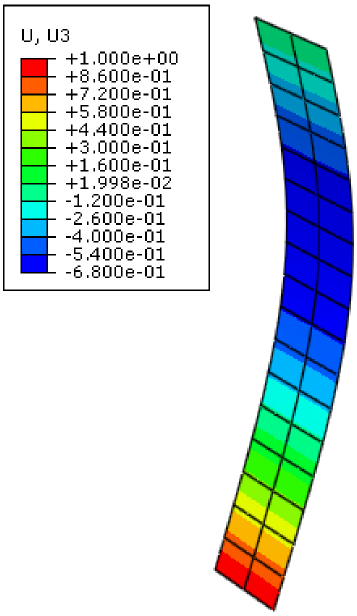


***Figure 7.3.*** Example of Column Shell Model Deflection in the 1st eigenmode for a unit displacement at the bottom.

## 7.3 Solid Model Set-Up

The solid model set-up is presented in this section. A representation of this latter is given in Fig. 7.4. The model is built up by assembling two semi-rigid slabs to the top and the bottom sections of the concrete column. Rebars are embedded in the concrete column along the column height.
The concrete column is tied to such slabs through the tie constraint. The slabs region are defined as master surfaces, and the concrete ones as slave surfaces, thus the concrete upper and lower faces follow the slabs displacements and rotations.
The boundary conditions are applied to the semi-rigid slabs. Displacements in the x-direction are constrained along the middle edge oriented along the z-direction at the top and bottom surfaces.

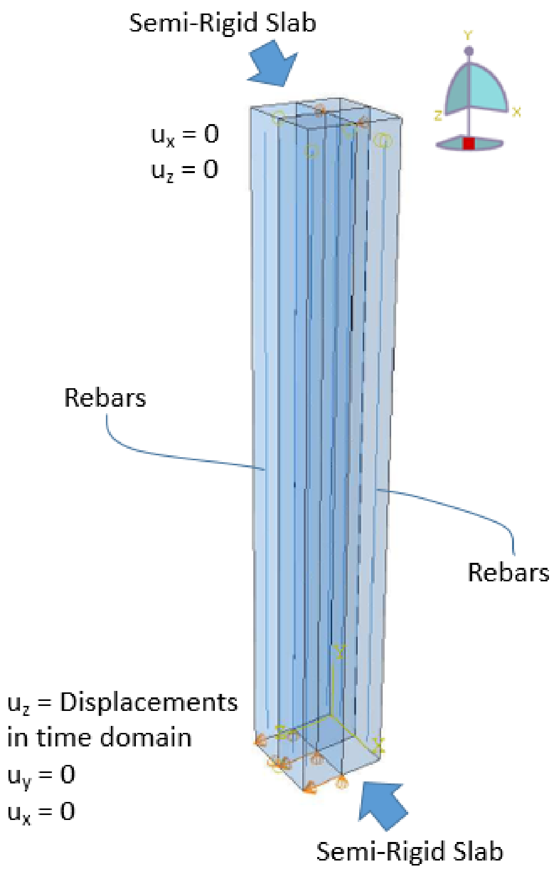


***Figure 7.4.*** Representation of Column Solid Model set-up.

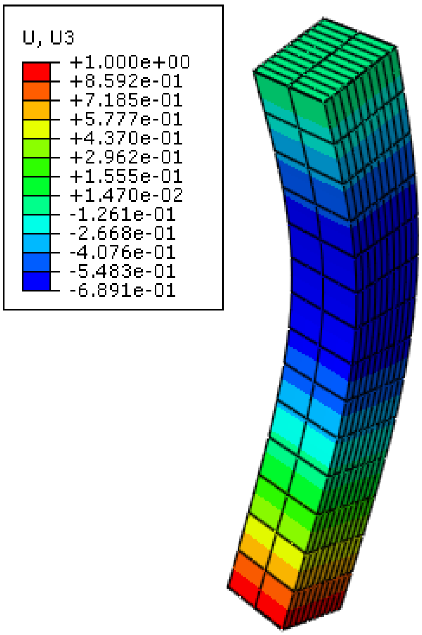


***Figure 7.5.*** Example of Column Solid Model Deflection in the 1st eigenmode for a unit displacement at the bottom.

On the top section displacements are set to be 0 in the z-direction along the middle edge oriented in the x-direction. At the bottom face on the middle edge oriented in the x-direction displacements are constrained in the y-direction, and time-dependent displacements are applied in the z-direction.
Fig. 7.5 gives an illustration of the bending behavior of the solid model. Quadratic elements (C3D20), as illustrated in Fig. 5.20, are chosen to build up the model. Regarding the mesh only two elements are used over the column width, like in the shell one, for the same reason. Contrariwise 10 elements are included over the column thickness to better represent the column bending behavior.
However from Fig. 7.5 it can be derived that the column seems to bend in a physically realistic manner, thus the model is working correctly.

## 7.4 Eigenfrequencies Extraction and Damping Definition

The eigenfrequency ($\omega_n$) is the frequency at which the system tends to oscillate in absence of any driving or damping force. At each eigenfrequency various parts of the structure tend to move together sinusoidally at the same frequency (eigenmodes). In case the eigenfrequency matches the forced frequency, which represents the frequency of an applied force, the amplitude of the vibration tends to increase. This phenomenon is commonly known as resonance. [26]
The designer must then always be aware of what are the eigenfrequencies of the structure, and of what are the usual forced frequencies at the building site, in order to avoid resonance to occur.
Eigenfrequencies can be computed by solving the so called eigenvalue problem given in Eq. 7.1

$$([K] - \{\omega_n^2\}\,[M])\,\{\phi\} = 0 \tag{7.1}$$

where

| | |
|---|---|
| $\{\omega_n\}$ | Natural eigenfrequencies vector [rad/s] |
| $\{\phi\}$ | Eigenvector [-] |

For giving a better understanding of the structure dynamic behavior in resonance it is fundamental to introduce damping.
Damping ($\zeta$) is an influence on the structure that uses to reduce and restrict its oscillations. Physically damping is produced by the dissipation of the energy stored in the oscillation, and it can be defined as it follows. [27]

- No damping ($\zeta = 0$): The structure oscillates with no decay in amplitude.
- Under-damping ($0 \leq \zeta \leq 1$): The structure oscillates with the amplitude gradually decreasing to zero.
- Critical damping ($\zeta = 1$): The structure returns to equilibrium without oscillating.

The influence of damping on the resonance phenomenon is illustrated in Fig. 7.6, where $\omega$ is the forced frequency.

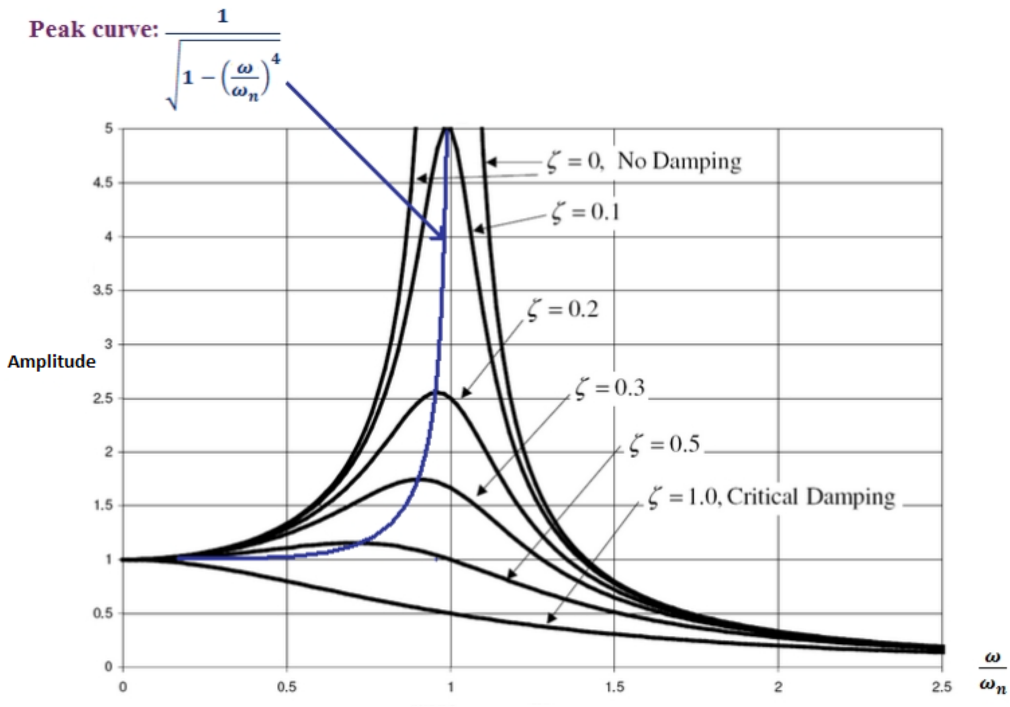


***Figure 7.6.*** Resonance amplitude change with damping ratio. [28]

In the above figure it can be seen that the amplitude tends to increase when the ratio $\omega/\omega_n$ tends to 1, thus when the forced frequency matches the eigenfrequency. The high influence of $\zeta$ on the amplitude can also be appreciated.

The eigenfrequencies are then computed for the shell and solid model from Eq. 7.1, and are summarized in Table 7.2. The eigenmodes are displayed in Fig. 7.7 and 7.8. As expected the eigenfrequencies of the two models provide almost a perfect match.

| Eigenmode | Shell Eigenfrequencies [Hz] | Solid Eigenfrequencies [Hz] |
|---|---|---|
| 1 | 10.26 | 10.54 |
| 2 | 30.47 | 31.29 |
| 3 | 57.11 | 58.60 |
| 4 | 87.29 | 89.54 |

***Table 7.2.*** Eigenfrequencies of the shell and solid model.

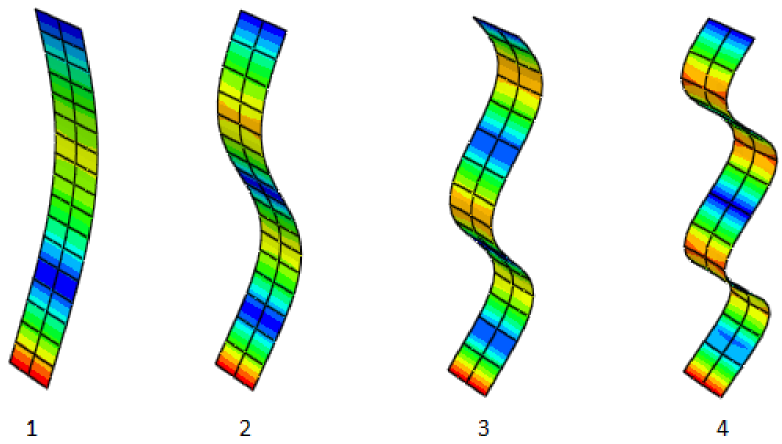


***Figure 7.7.*** Eigenmodes 1, 2, 3, and 4 for the shell model.

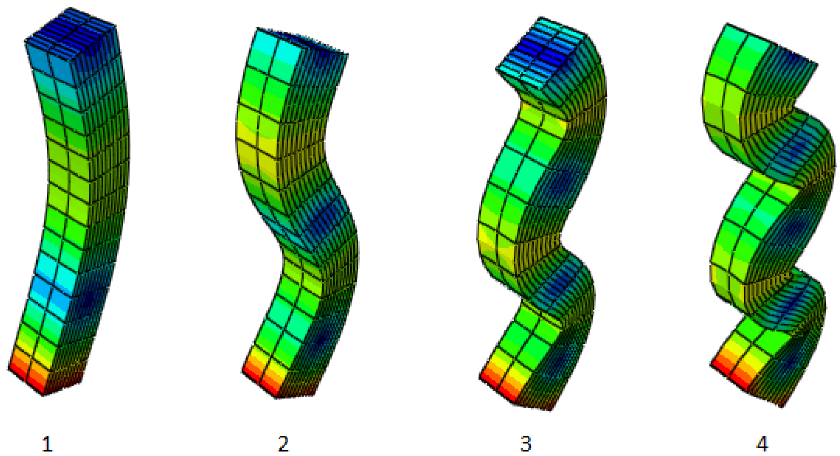


***Figure 7.8.*** Eigenmodes 1, 2, 3, and 4 for the solid model.

As previously discussed at the beginning of this chapter the dynamic implicit procedure involves a time-integrated procedure. Damping is usually introduced in dynamic non-linear analyses through a mass- and stiffness-proportional damping, so called Raylegh damping. Its approach is based on the proportionality of the damping matrix, $[C]$, to the mass and stiffness matrices, respectively $[K]$ and $[M]$. Such statement is expressed in Eq. 7.2.

$$[C] = \alpha\,[M] + \beta\,[K] \tag{7.2}$$

where

$\alpha$ Mass-proportional damping coefficient [-]
$\beta$ Stiffness-proportional damping cooefficient [-]

Relationships between the equations contained in Eq. 7.2 and orthogonality conditions allow Eq. 7.2 to be rewritten as Eq. 7.3.

$$\zeta = \frac{1}{2\,\omega_n}\alpha + \frac{\omega_n}{2}\beta \tag{7.3}$$

The damping ratio then varies with the natural frequencies. The damping coefficient, $\alpha$ and $\beta$, are usually selected according to engineering judgment by specifying the damping for the most significant eigenmodes, and thus eigenfrequencies.
The structure will be mainly excited in a way to vibrate in the $1^{st}$ and $2^{nd}$ eigenmodes. Damping ratios are then equally specified at these eigenfrequencies for concrete and steel, respectively as 5% and 2%.
If the damping ratios ($\zeta_i$ and $\zeta_j$), associated with these two specified eigenfrequencies ($\omega_i$ and $\omega_j$), are known, and set equal ($\zeta_i = \zeta_j$), the conditions associated with the proportionality factors simplify, and two Raylegh damping factors can be computed as in Eq. 7.4. [29]

$$\beta = \frac{2\zeta}{\omega_i + \omega_j} \qquad \alpha = \omega_i\,\omega_j\,\beta \tag{7.4}$$

The values of Raylegh coefficients are computed in function of the shell and solid models eigenfrequencies given in Tab. 7.2, and the results are summarized in Tab. 7.3.

| - | Concrete (Shell) | Steel (Shell) | Concrete (Solid) | Steel (Solid) |
|---|---|---|---|---|
| $\zeta$ [%] | 5 | 2 | 5 | 2 |
| $\alpha$ [rad/s] | 31.93 | 12.10 | 31.09 | 12.43 |
| $\beta$ [s/rad] | $3.91 \cdot 10^{-3}$ | $1.56 \cdot 10^{-3}$ | $3.81 \cdot 10^{-3}$ | $1.52 \cdot 10^{-3}$ |

***Table 7.3.*** Raylegh coefficients for the shell and solid model for concrete and steel.

## 7.5 Earthquake Excitation

In this section the earthquake excitation data manipulation and adjustment to fit the structure eigenfrequencies are presented.
The data used refer to El Centro earthquake, previously mentioned in the introduction, and an illustration of them in time domain was given in Fig. 1.6.
Since the structure after the excitation ends will still vibrate it is needed to adjust the earthquake data, and thus add trailing zeros. By such operation the FE model will then continue to vibrate, fitting better the real behavior of the structure.
The length of the time domain needs to be prolongated until a certain time at which the structure will stop to vibrate. Also the objective of the upcoming analysis is to obtain the earthquake amplitudes in frequency domain. Such operation is carried out through the famous Discrete Fourier transform (DFT). This latter transforms a function (or, as in this case, a discrete set of data) of one variable, acceleration in this case, which lies in the time domain (s), to another function (a discrete set of data) lying in the frequency domain (Hz), and changes the basis of the data to cosines and sines.
The expression of this latter is given in Eq. 7.5.

$$F(\omega) = \int_{-\infty}^{+\infty} f(t)\, e^{-i\omega t} dt \tag{7.5}$$

where

| | |
|---|---|
| $\omega$ | Set of frequencies points with constant frequency increment [Hz] |
| $t$ | Set of time points with constant time increment [-] |
| $F(\omega)$ | Function in frequency domain |
| $f(t)$ | Function in time domain |

Commonly such operation is instead computed through the so called Fast Fourier Transform (FFT). This latter consists in an ingenious algorithm capable to reduce the complexity of computing the DFT from $O(n^2)$, to $O(n \log n)$, where $n$ is the data size. [30]
Such algorithm is extremely efficient if the amount of data coincides with a power-of-2.
For the above mentioned reason the data size is increased to three power-of-2 as illustrated in Tab. 7.4.

| Power-of-2 | Data size |
|---|---|
| $2^{12}$ | 4096 |
| $2^{13}$ | 8192 |
| $2^{14}$ | 16384 |

***Table 7.4.*** Data size computed corresponding to powers-of-2.

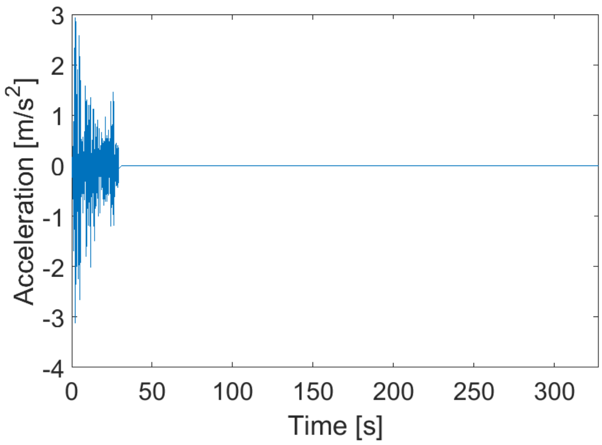


***Figure 7.9.*** El Centro acceleration data extended to a $2^{14}$ size.

The acceleration data, illustrated in Fig. 7.9 for $2^{14}$ time steps, are then integrated through the trapezoidal rule to obtain velocities. However the trailing zero accelerations result in a constant value of velocity (drift) which is an unrealistic hypothesis. The data are thus adjusted using the baseline correction.

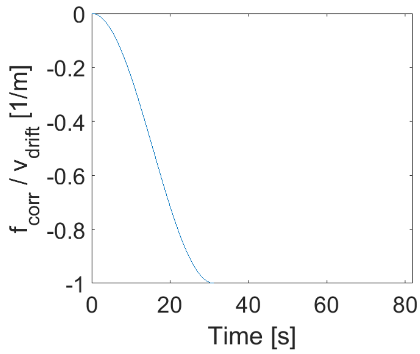


***Figure 7.10.*** Baseline Correction Factor evolution in time domain.

This latter works through the generation of a cosine correction factor that is then added to the data. The ratio of the correction factor over the drift against time is represented in Fig. 7.10.

The velocity data and the baseline corrected ones are represented in time domain in Fig. 7.11. The difference between the original data and the baseline corrected ones appears to be almost imperceptible. However a further integration of the original velocity data would have lead to a linear variation of displacements resulting in a wrong interpretation of the data.

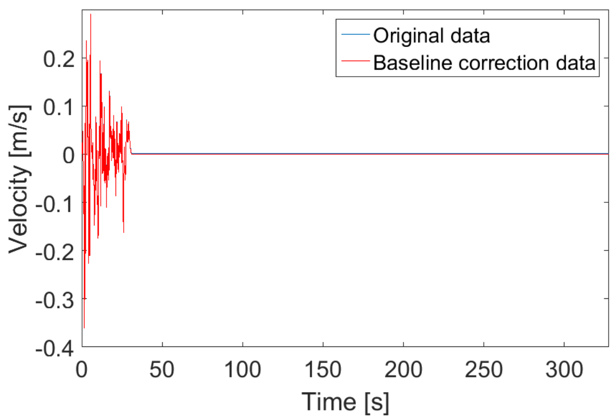


***Figure 7.11.*** El Centro velocities data extended to a $2^{14}$ size.

By applying the trapezoidal rule of integration once more the displacement data are obtained. In such data a constant value of displacement is present again, but in such case the baseline correction is not applied since it is realistic that after an earthquake excitation there can still be residual displacements.
A representation of the obtained displacement data in time domain is given in Fig. 7.12.

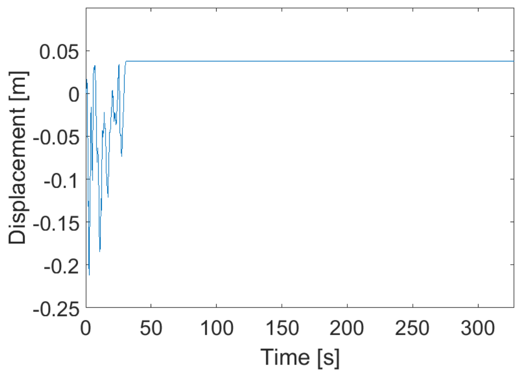


***Figure 7.12.*** El Centro displacement data extended to a $2^{14}$ size.

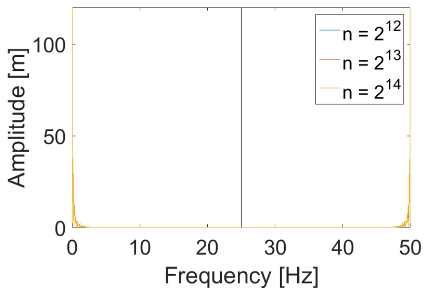


***Figure 7.13.*** Displacements Amplitude in Frequency Domain.

A FFT is then performed obtaining the data conversion to frequency domain. Fig. 7.13 gives a representation of the amplitudes in frequency domain for the three performed power-of-2 increments. The FFT returns mirror data with respect to the so called Nyquist frequency, represented by the vertical black line, which is a half of the sample frequency. The FFT results are thus represented again in Fig. 7.14 for a lower frequency interval. In such figure only a slight difference between the obtained data set can be appreciated. A close-up of the highlighted black square is given in Fig.7.15.

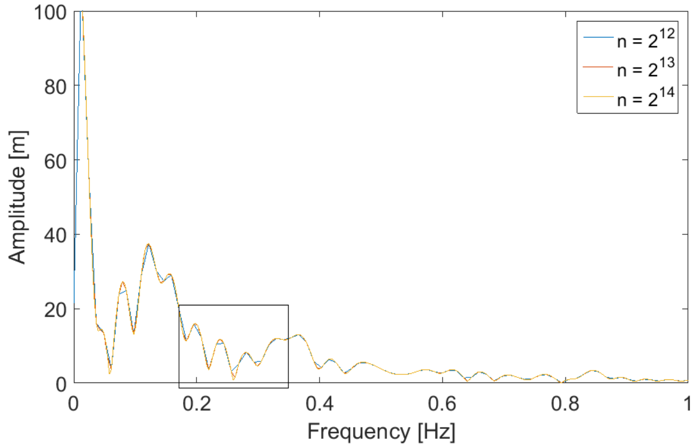


***Figure 7.14.*** Displacements Amplitude in Frequency Domain for a lower frequency interval.

From such figure it can be deducted the difference between the powers-of-2 data sizes. The blue line corresponding to $2^{12}$ data is obviously the less accurate since it contains the lower amount of data points. The orange line ($2^{13}$ data) contains the double of the data point of the previously analyzed case, thus in between two data points of the blue line, the orange one contains one point more. The same concept applies for the case of the data size of $2^{14}$. Then the shape of this latter is obviously smoother and more precise than the ones corresponding to lower powers-of-2. Contrariwise the blue line shape appears to be more piece-wise for the contrary reason.

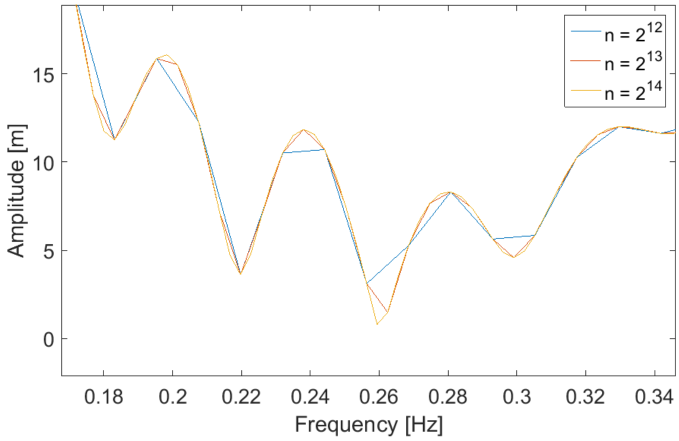


***Figure 7.15.*** Close-up of Displacements Amplitude in Frequency Domain.

After having tested the elastic dynamic behavior of the column the highest power-of-2 is chosen for the upcoming analyses since it is the only one providing enough data points to make the structure stop vibrating. Moreover, as it was already remarked in precedence, it returns the most accurate results when transforming the data to frequency domain.

At this point the data need to be adjusted in order to make the forced frequency match the eigenfrequency at a higher amplitudes. For such scope a reduction factor ($r$) is introduced. The time domain is reduced by this factor to vary the frequency domain, while the amplitudes will remain non-altered.
The procedure for deriving the displacements is alike the one previously introduced. The obtained results in terms of displacements are given in Fig. 7.16

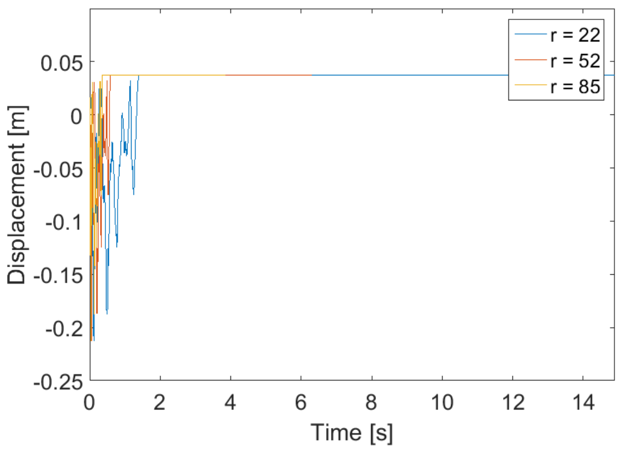


***Figure 7.16.*** Squeezed Displacements Time Domain.

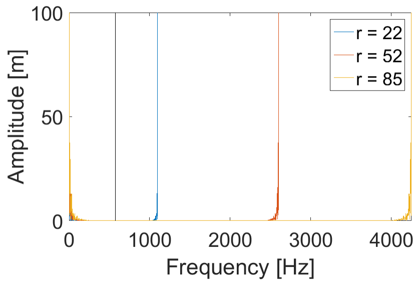


***Figure 7.17.*** Amplitudes of Squeezed Displacements in Frequency Domain.

The used reduction factors are depicted in such figure. Those numbers were obtained through an iterative process in which they were varying while observing the changes in the frequency domain.
The FFT results of the above displacements are given in Fig. 7.17.
Obviously the sampling frequencies vary in function of $r$ since the time steps are reduced by this latter. The results of the FFT can then be compared only for values below the Nyquist frequency, depicted by the vertical black line again.
A close-up of Fig. 7.17, is given in Fig. 7.18, and it can give a better clarification of the meaning of such reductions.
Higher importance is given to the first two eigenmodes, which are the most predominant in the structural response.
The reduction factors are derived in a manner that the first two eigenfrequencies correspond to some peaks of forced frequencies. The $4^{th}$ eigenmode is disregarded since it takes place at too high frequencies, which are occurring only in the very initial part of the earthquake excitation, and the amplitudes is also not significant. The same concept applies for the $3^{rd}$ eigenmode even though it occurs at lower frequencies and has higher amplitudes, and it can be slightly observed at the beginning of the excitation.

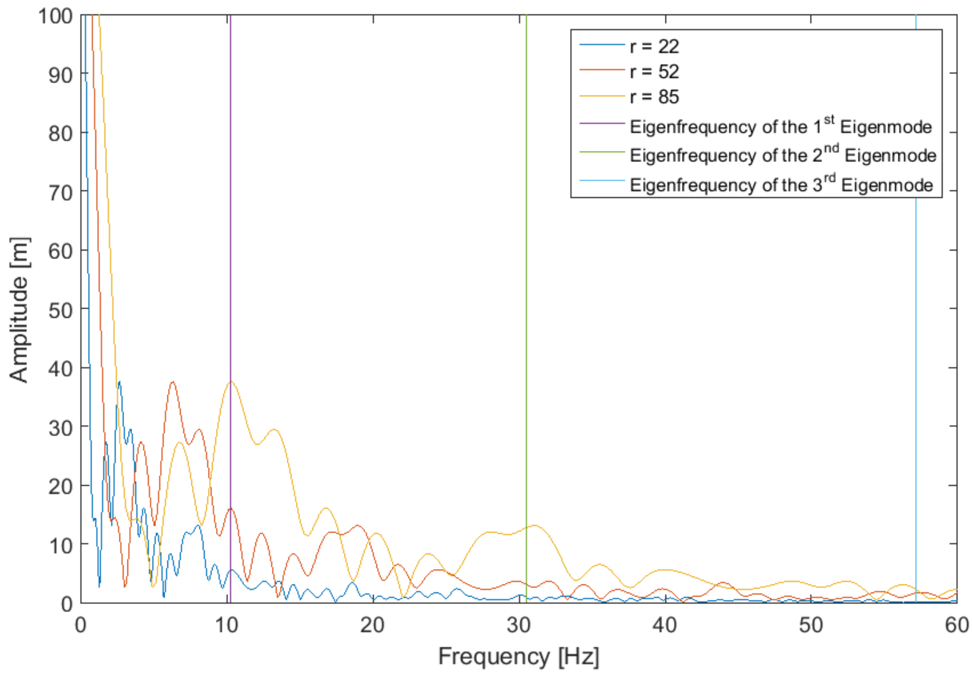


***Figure 7.18.*** Close-up of amplitudes of squeezed displacements in frequency domain.

# Dynamic Analyses Results 8

*The dynamic response of the structure is evaluated at first elastically, and then plastically for the shell model. A plastic analysis of the solid model is then also carried out. Finally the obtained results are analyzed and discussed.*

## 8.1 Elastic Analyses of Shell Model

Preliminarily an elastic analysis is performed on the shell model in order to test the resonance phenomenon.

The normal stresses in the longitudinal direction of the column (y-direction) are tracked in the point highlighted in Fig. 8.1, and the obtained results are given in Fig. 8.2.

It is important to remark that this kind of analysis is carried out only for having an idea of how the structure would respond to the earthquake excitation. Such analysis is very useful since the computation time of a dynamic non-linear problem is way higher than the one of a linear problem. However in elastic materials the stress values are simply directly proportional to strains, while in a plastic one the material model is, as previously discussed, more complex.

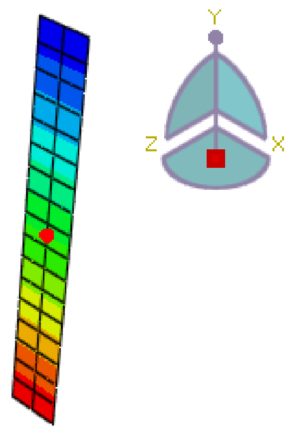


***Figure 8.1.*** Point in which the normal stresses are tracked in the shell model.

The values of the normal stresses appear to be way higher than the maximum allowable stress limits of concrete.

The application of these displacements time-series would then lead to the occurrence of failure so soon that the dynamic response of the structure could not be observed. However such an analysis is carried out only for an illustrative scope, and is presented in the next section.

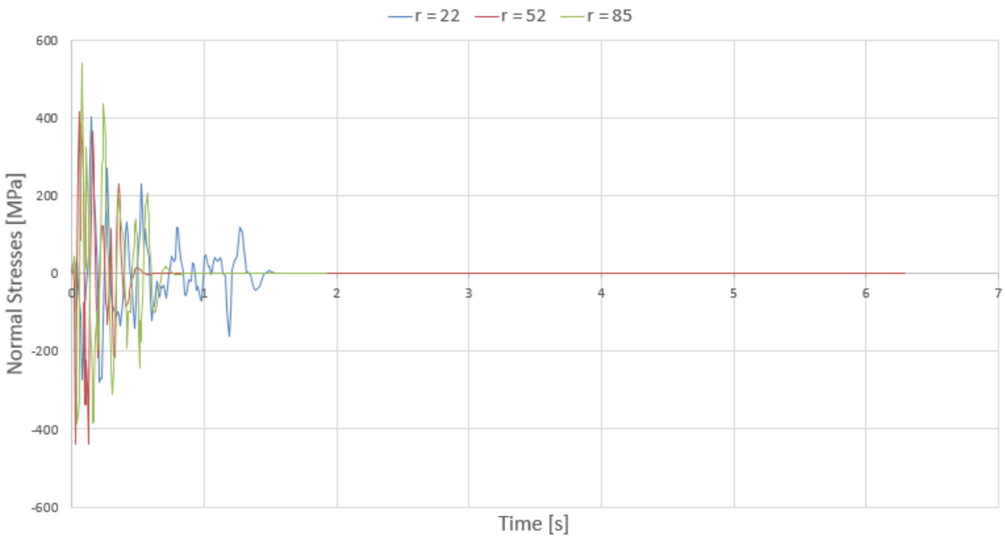


***Figure 8.2.*** Shell Model Elastic Dynamic Response to the earthquake excitation given in Fig. 7.16 and 7.17.

The overall stresses need then to be decreased by a certain new reducing factor ($d$). The value of this latter is set to 17. The definition of $d$ is carried out by reducing the normal stresses and monitoring the amount of points crossing the concrete compressive strength threshold. The decreased displacements in time domain are given in Fig. 8.3.

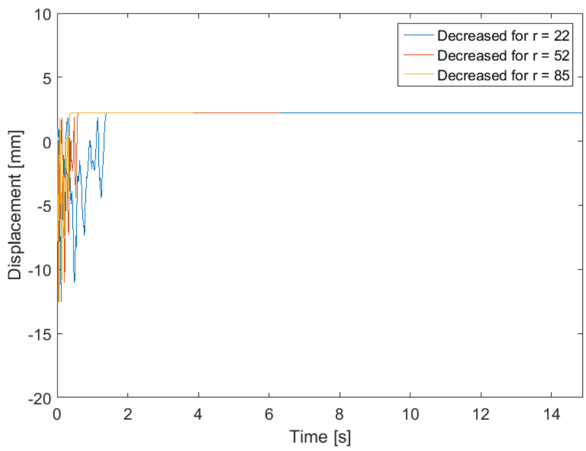


***Figure 8.3.*** Squeezed and Decreased Displacements in Time Domain.

The aim of this analysis is to obtain three new earthquake excitations that would lead to different responses of the structure.
Since an elastic analysis is carried out the obtained new stresses are obviously proportional to the ones shown in Fig. 8.2, and they are displayed in Fig. 8.4.

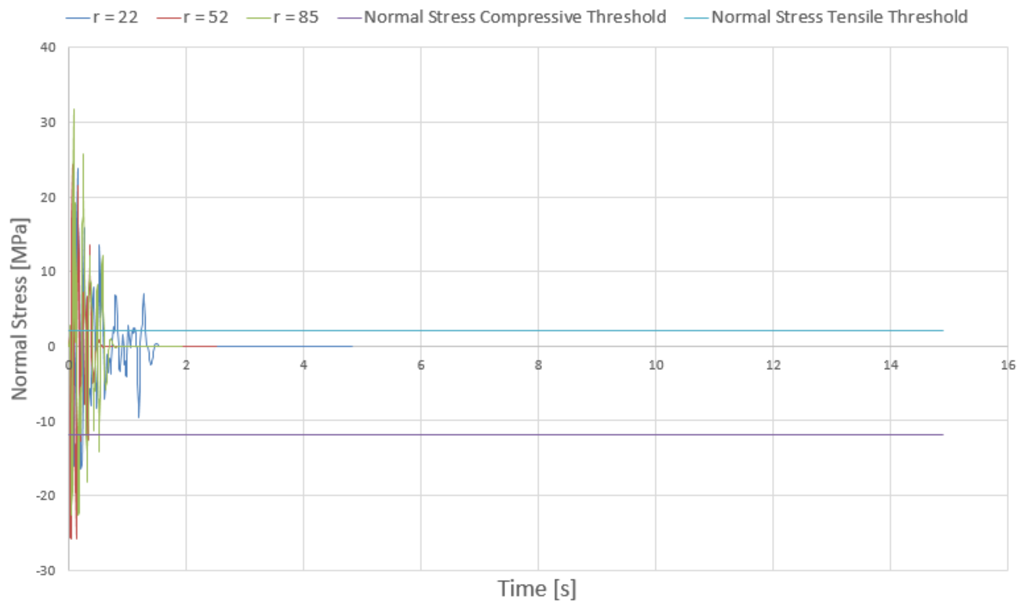


***Figure 8.4.*** Shell Model Elastic Dynamic Response to the earthquake excitation given in Fig. 8.3

## 8.2 Plastic Analyses of Shell Model

In this section the results of the plastic analyses carried out for the shell model are presented.
Three analyses are implemented for the data illustrated in time domain in Fig. 7.16, and in frequency domain in Fig. 7.17.
The obtained results in terms of normal stresses are tracked in the point depicted in Fig. 8.1, and they are illustrated in Fig. 8.5.

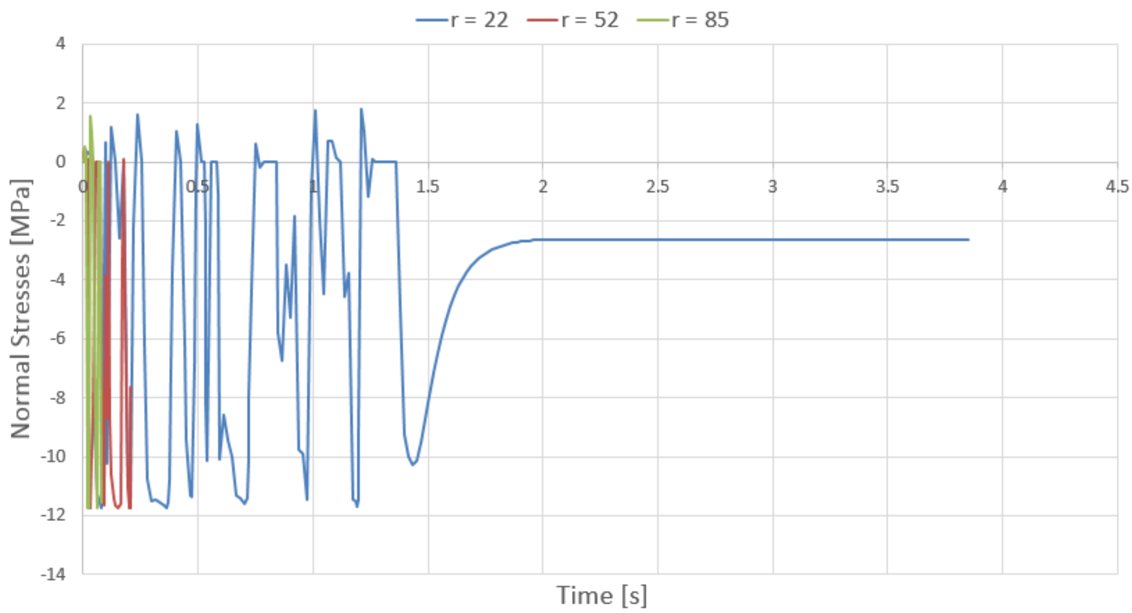


***Figure 8.5.*** Shell Model Plastic Dynamic Response to the earthquake excitation given in Fig. 7.16 and 7.17.

The models with $r = 85$ and $r = 52$ reach failure (non-convergence) in a very short amount of elapsed time, while the one with $r = 22$ does not. The time step at which failure occurs is dependent on the reduction factor $r$. Such results was also expected since, as shown in Fig. 7.18, for higher reduction factors higher displacements amplitude are obtained at all eigenfrequencies.
It can also be noticed that the maximum values of stresses concrete can carry result to be slightly higher than the ones that are assigned to the material model (corresponding to the design values depicted in Tables 2.2 and 2.3). This is due to the fact that the concrete damage plasticity model, as previously mentioned, contains isotropic hardening leading to a gradual expansion of the failure surface within increments in plastic strains. Moreover such maximum values of normal stresses appear to be more or less equal each other between the depicted series, and that is logical too since the material strengths used are the same.
The same analysis is then carried out for the earthquake excitation reduced by the reduction factor $d$, thus with reference to the displacements given in Fig. 8.3. The obtained results in terms of normal stresses are tracked in the same point, given in Fig. 8.1, and they are illustrated in Fig. 8.6.

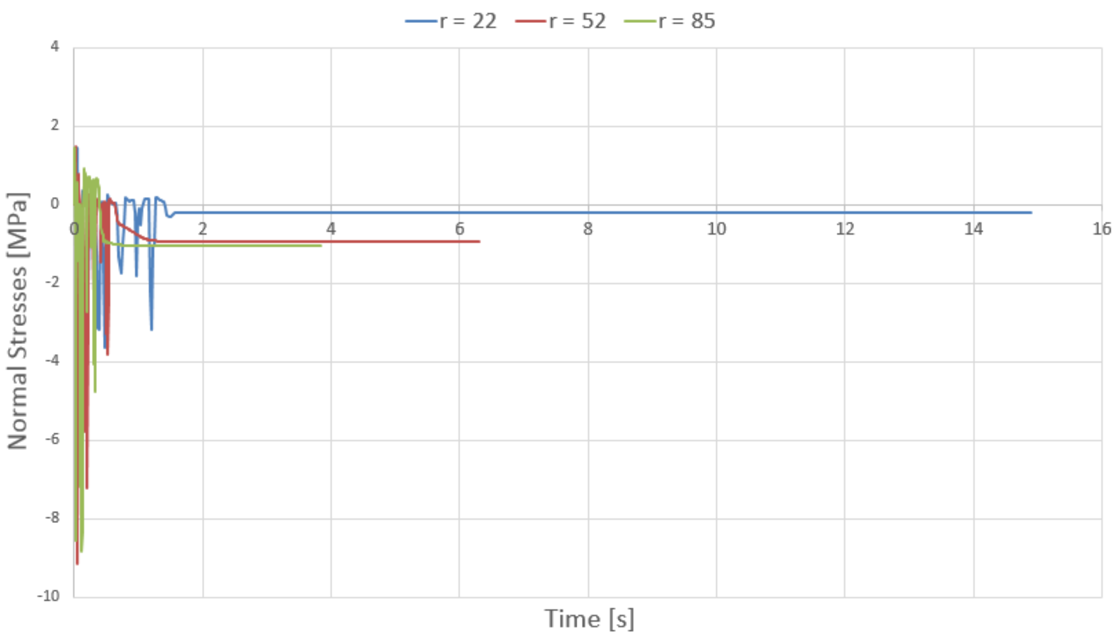


***Figure 8.6.*** Shell Model Plastic Dynamic Response to the earthquake excitation given in Fig. 8.3.

From the above graph some interesting considerations can be extracted.
At the last time step of the three data series the final stress never perfectly coincides. Such results were also expected since the three forced displacement series excite the structure with different frequencies, thus they lead it to vibrate in different manners. Generally higher reduction factors leads to higher values of normal stresses. That is also logical since higher displacements amplitudes are given for higher reduction factors (see Fig. 7.18).

Moreover the maximum strength of concrete is never reached, but the model is, in all cases, into plasticity. The damage also plays an important role in such analysis since the damage parameters increase with the inelastic strains leading to a reduction of the initial Young's modulus, and thus a reduction in terms of normal stresses.

## 8.3 Plastic Analyses of Solid Model

Plastic analyses are carried out for the solid model for the earthquake excitation shown in Fig. 8.3. The obtained results are tracked in Fig. 8.7, and they are displayed in Fig. 8.8. The obtained results are almost alike the ones derived for the shell model. The same considerations given for the shell case results apply to the solid model ones as well.

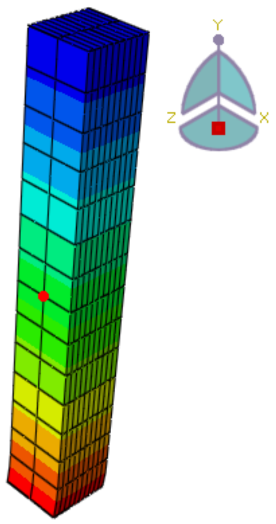


***Figure 8.7.*** Point in which the normal stresses are tracked in the solid model.

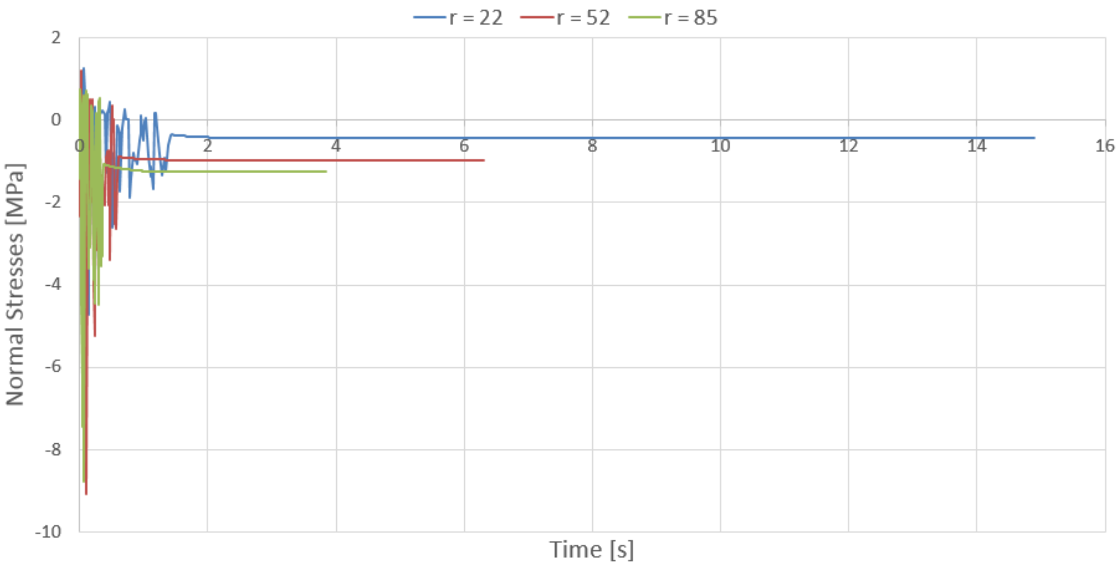


***Figure 8.8.*** Solid Model Plastic Dynamic Response to the earthquake excitation given in Fig. 8.3.

## 8.4 Analysis and Comparison of the Results

In this section the obtained results are discussed and compared.
By introducing a time-dependent displacement the problem turned from static to dynamic. Within a cyclic behavior the effect of damage and stiffness recovery are included into the CDP model.
Damping is also inserted in the model when the problem turns to dynamic.
From the above obtained results it can be observed that damping of RC structures is so high that once the earthquake excitation stops the structure almost does not vibrate at all.
However damage is considered to be the main problem of concrete in cyclic behavior. Once the structure compressive and/or tensile damage increases the maximum bearing load decreases since concrete strength gets lower and lower.

Fig. 8.9 overlaps the shell and solid model dynamic responses for the time-dependent displacements shown in Fig. 8.3 with a reduction factor, $r$, of 52. The two models seem to respond quite similarly, and once the earthquake excitation ends the normal stresses appear to be almost identical. The slight differences between these two responses may be given by the fact that, when running the FE analyses, data were extracted at different amounts of time increments. Such choice was made in order to optimize and fasten the computations, especially for the solid model.

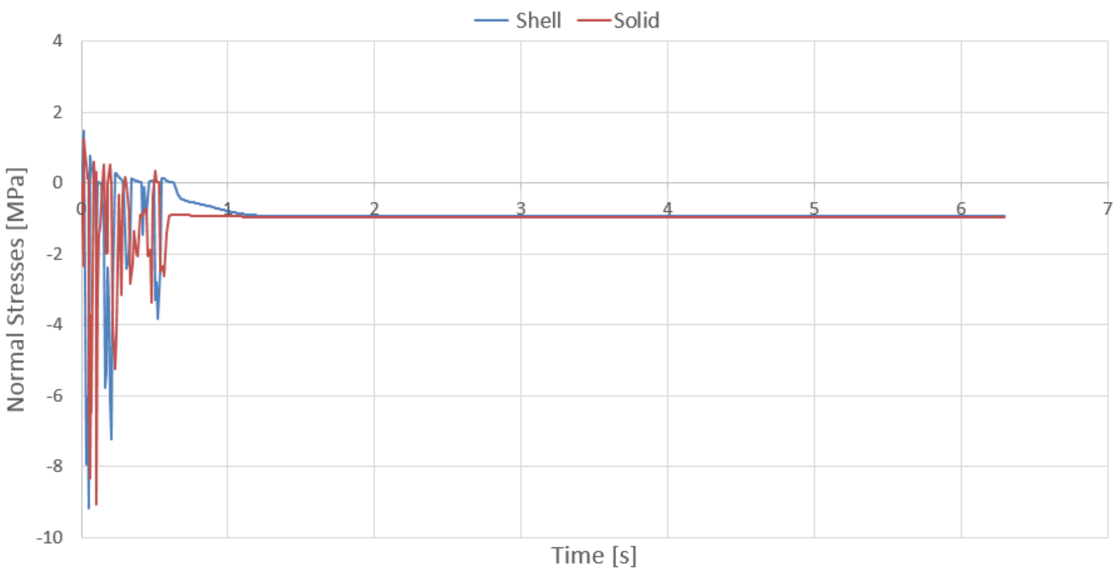


***Figure 8.9.*** Comparison of shell and solid models' dynamic responses for the forced displacement reduced by r = 52 given in Fig. 8.3.

# Conclusions 9

In this chapter conclusions on the overall project are carried out.

Tab. 9.1 illustrates the results obtained in the static analyses with reference to the design strength case for maximum vertical displacements ($u_{max}$), maximum compressive stress in concrete ($\sigma_{c,max}$), and maximum bearing load ($P_{max}$). In general a very good match can be appreciated between them, with percentages of main differences between analytical and numerical analysis not exceeding 14%.

The limit state approach has been applied for decades to the design of RC structures, while the FE one is a relatively new and more sophisticated method. The usage of such numerical analyses for the design a simple structure, like a RC beam, is however not suggested. Numerical methods are more likely useful to model complex geometries, where the implementation of an analytical procedure is not recommendable.

However, in this report, the efficiency of the CDP model was tested, giving, as shown in the below table, very good results.

Regarding the two implemented FE models, shell and solid, they also gave a good match. For this type of analysis, then, it would be recommended to use shell models for their lower computation cost. However it is not certain that the same results would have been achieved for a more complex geometry as well, for which a solid model remains the most realistic and recommendable approach to use despite its high computation time.

It is also important to remark that FE analyses are very flexible, in the sense that by manipulating the material models the designer is able to run simulations including different effects. In this case, for example, in the shell models, the tensile stress-strain relationship was adjusted in order to simulate the behavior of concrete for varying rate of weakening. Also, in the solid models, a variation of fracture energy was applied, thus including higher and lower tension stiffening, to test how it affects the RC beam behavior.

| - | $u_{max}$ [mm] | $\sigma_{c,max}$ [MPa] | $P_{max}$ [kN] |
|---|---|---|---|
| Limit State | 19.44 | 11.5 | 52.2 |
| Shell Model | 21.5 | 11.2 | 69.8 |
| Solid Model | 19.07 | 11.4 | 72.5 |
| Main Difference [%] | 10.0 | 2.2 | 14.0 |

***Table 9.1.*** Sum-up of static analyses results for the design strength case.

Regarding the dynamic analyses some of the obtained results, for the shell and solid model, are summarized in Tab. 9.2 with reference to maximum compressive and tensile stresses ($\sigma_{c,max}$, $\sigma_{t,max}$ ), and stress after the earthquake excitation ($\sigma_{c,fin}$). Such results are tracked respectively for the shell and solid model in the points depicted in Fig. 8.1 and 8.7. The data refer to the case with a reduction factor, $r$, of 52.
In this case as well the two models generally gave a pretty good match, since the results difference does not exceed 2.13 %.
The usefulness of FE applications in dynamic analyses is instead enormous. Modal and dynamic implicit analyses are performed giving as output the deformed shape of the FE mesh. It is unthinkable to reach the same results through an analytical approach.
As previously shown the earthquake data from El Centro were adjusted and manipulated to match the structure eigenfrequency corresponding to the $1^{st}$ eigenmode.
In reality the designer is required to use the inverse approach, thus manipulating the structure eigenfrequencies to get them as far as possible from the earthquake frequencies with highest amplitudes.
It is also important to remark that computation time for non-linear dynamic FE analyses is very high.
An essential aspect of such analyses is how the cyclic behavior affects the compressive and tensile concrete strength, that gets lower and lower within an increasing amount of cycles, thus giving maximum stresses in compression lower than the model specified maximum compressive and tensile strengths.

| - | $\sigma_{c,max}$ [MPa] | $\sigma_{t,max}$ [MPa] | $\sigma_{c,fin}$ [MPa] |
|---|---|---|---|
| Shell Model | -9.08 | 1.22 | -0.94 |
| Solid Model | -9.07 | 1.21 | -0.96 |
| Difference [%] | 0.11 | 0.82 | 2.13 |

***Table 9.2.*** Sum-up of dynamic analyses results for the design strength case and for the case of $r = 52$.

# Bibliography


[1] **NRMCA**: *"About Ready Mixed Concrete"*, `http://www.concreteanswers.org/about/readymix.html`

[2] **Carl W.**: *"Technology and Culture"*, he First Reinforced-Concrete Skyscraper: The Ingalls Building in Cincinnati and Its Place in Structural History, February 2014.

[3] **Thomas J., Jenning H.**: *"The science of concrete"*, Northwestern University, Evanston, IL, 2008.

[4] **Stover C.W., Coffman J.L.**: *"Seismicity of the United States"*, U.S. Geological Survey professional paper, 1989.

[5] **Jackson N., Dhir R.K.**: *"The Mathematics of Material Quality Control "*, The Royal Academy of Engineering.

[6] **Dehn F.**: *"Constitutive Concrete and Durability Models in the new fib Model Code 2010"*, Encontro Nacional - BE2012 FEUP, October 24-26, 2012.

[7] **Di Ludovico M.**: *"Retrofit and design of reinforced concrete structures"*, Department of Structural Engineering University of Naples Federico II.

[8] **McCorman, Jack C.**: *" Structural Steel Desig"*, Upper Saddle River, NJ: Pearson Prentice Hall. ISBN 978-0-13-221816-0..

[9] **Landau L.D., Lifshitz E.M.**: *"Theory of Elasticity"*,Vol. 7 (3rd ed.). Butterworth-Heinemann. p. 42. ISBN 978-0-7506-2633-0

[10] **Deaton J.**: *"A Finite Element Approach to Reinforced Concrete Slab Design"*, School of Civil and Environmental Engineering, Georgia Institute of Technology, August 2005. `https://smartech.gatech.edu/bitstream/handle/1853/7188/deaton_james_b_200508_mast.pdf`

[11] **Grassl P., Xenos D., Ulrika N., Rempling R., Gylltoft K.**: *"CPDM2: A damage-plasticity approach to modelling the failure of concrete"*, July 2013.

[12] **Abaqus/CAE User Guide**: *"Concrete Damage Plasticity"*.

[13] **Birtel V., Mark P.**: *"Parameterised Finite Element Modelling of RC Beam Shear Failure"*, Ruhr-University Bochum, Universitätsstr. 150, 44780 Bochum, Germany Institute for Reinforced and Prestressed Concrete Structures

[14] **Kmiecik P., Kaminski M.**: *"Modelling of reinforced concrete structures and composite structures with concrete strength degradation taken into consideration"*, Wrocław University of Technology, Wybrzeże Wyspiańskiego 25, 50-370 Wrocław, Poland.

[15] **Karihaloo B.L., Abdalla H.M., Imjau T.**: *A simple method for determining the true specific fracture energy of concrete"*, Cardiff University, Magazine of Concrete Research, 2003, 55, No. 5, October, 471–481.

[16] **Von Mises, R.**: *"Mechanik der festen Körper im plastisch deformablen Zustand"*, Göttin. Nachr. Math. Phys., vol. 1, pp. 582–592.

[17] **Abaqus/CAE User Guide**: *"General Metal Plasticity"*.

[18] **Cook R., Malkus D., Plesha M., Witt R.**: *"Concepts and Application of Finite Elements Analysis"*, Fourth ed., J. Wiley, 2002.

[19] **Abaqus/CAE User Guide**: *"Shell Elements"*.

[20] **Shen W., Lei G.**: *"Application of the Finite Element Method to Deflection in a Cantilever Beam"*, Rensselaer Politechnic Institut.

[21] **Dorph M.**: *"Concrete building subjected to earthquake excitation by using Finite Element Analysis"*, Aalborg University, January 2010.

[22] **Miao Z.W., Lu X.Z., Jiang J.J., Ye L.P.**: *"Nonlinear FE Model for RC Shear Walls Based on Multi-layer Shell Element and Microplane Constitutive Model"*, Department of Civil Engineering, Tsinghua University, Beijing.

[23] **Abaqus/CAE User Guide**: *"Solid Elements"*.

[24] **Yang J.G.**: *"Finite Element Analysis"*, VirginaTech University, 1997.

[25] **Autodesk User Guide**: *"Truss Elements"*.

[26] **Bhatt, P.**: *"Maximum Marks Maximum Knowledge in Physics"*, Allied Publishers. ISBN 9788184244441. Retrieved 2014-01-10.

[27] **Ogata, K.**: *"System Dynamics"*,(4th ed.). University of Minnesota, 2005.

[28] **Rodrigues, D.**: *"Resonant Frequency"*.

[29] **Wilson, E. L.**: *"Static and Dynamic Analysis of Structures"* (4th ed.). Berkeley, CA: Computers and Structures, Inc.

[30] **Van Loan, C.**: *"Computational Frameworks for the Fast Fourier Transform "* (SIAM, 1992).